Electrode-electrolyte interface layers in lithium ion batteries using reactive force field based molecular dynamics

by

Sahithya Reddivari

A dissertation submitted in partial fulfillment
of the requirements for the degree of
Doctor of Philosophy
(Environmental Engineering)
in the University of Michigan
2016

Doctoral Committee:

Associate Professor Christian M. Lastoskie, Chair
Research Associate Professor Herek L. Clack
Professor Wei Lu
Professor Adri C. T. van Duin, Pennsylvania State University

DEDICATION

To my family

Because you were my inspiration, my support and because you will never read it.

ACKNOWLEDGEMENT

I would like to thank my advisor, Dr. Christian Lastoskie, for his unwavering guidance throughout my graduate school experience and for being the role model that I aspire to be. I am grateful to Dr. Adri van Duin and his team at Penn State for hosting me in their lab and their continued assistance with the ReaxFF optimization. Thank you Dr. Wei Lu and Dr. Herek Clack for your counsel and constant encouragement during group meetings and conference presentations. My committee's valuable inputs and insights have not only elevated my dissertation work, but also advanced to my ability has a researcher.

A special thanks to all my mentors at the University of Michigan, Dr. Aline Cotel, Dr. Avery Demond, Dr. Andrew Gronewold and Dr. Steven Wright to name a few. Your unconditional mentorship has helped me achieve goals I never imagined I would.

My research group members, Dr. Trinh Tran, Dr. Qiang Dai, Dr Francisco Sotomayor, Margaret Reuter and Christina Reynolds, who have been my pillars of support for the past six years. I cannot thank you enough for your contributions to this dissertation be it brainstorming for ideas, feedback, cakes/cookies or just entertaining conversations.

My loving family, thank you for always encouraging me to reach beyond anything I ever dreamed for myself. I am so fortunate to have a family that is always proud of my achievements, however unusual they may be.

I am grateful to have had the opportunity to attend the University of Michigan and be part of a wonderful (barely adequate) community. My experiences here have helped me grow as a researcher, educator and a citizen of the world. It's now time for me to go make the Michigan difference in the world. I am sad to leave my home of six years, but happy to trade my mittens for some sunshine!

TABLE OF CONTENTS

LIST OF TABLES

LIST OF FIGURES

LIST OF APPENDICES

LIST OF ABBREVIATIONS

CLC	Chemical Looping Combustion
DFT	Density Functional Theory
DMC	Dimethyl Carbonate
DNP	Double Numerical Plus
EC	Ethylene Carbonate
EIS	Electrochemical Impedance Spectroscopy
EPMA	Electron Probe Micro analyzer
EV	Electric Vehicles
FEC	Fluoroethylene Carbonate
FTIR	Fourier Transform Infrared Spectroscopy
GCMS	Gas Chromatography Mass Spectrometry
GGA	Generalized Gradient Approximation
IR	Infrared
LAMMPS	Large Scale Atomic/Molecular Massively Parallel Simulator
Li-ion	Lithium ion battery
LMO	Lithium manganese oxide
MD	Molecular Dynamics
MM	Molecular Mechanics
NMR	Nuclear magnetic resonance
OSC	Oxygen storage compounds

PBE	Perdew-Burke-Ernzerhof
PEC	Polyethylene carbonate
PVDF	Polyvinylidene fluoride
QM	Quantum Mechanics
SEI	Solid Electrolyte Interface
SEM	Scanning Electron Microscopy
USABC	United States Automotive Battery Consortium
TEM	Tunneling Electron Microscopy
VC	Vinylene Carbonate
XAS	X-ray Absorption Spectroscopy
XPS	X-ray Photoelectron Spectroscopy

ABSTRACT

Lithium manganese oxide cathode and graphite anode based batteries are sought after for high power applications like electric vehicles and energy storage due to their high capacity, low cost and low toxicity. However, there are well-documented problems with capacity fade and cycle life for this battery chemistry, caused by the dissolution of divalent manganese from the cathode surface and deposition of dissolved manganese onto the anode. Dissolution of manganese from the $LiMn_2O_4$ surface into the electrolyte leads to a progressive decrease in the cathode material available for lithium intercalation.

A key to improving the retention of manganese is to understand the reactions that occur at the cathode surface. Tunneling electron microscopy imaging has shown the presence of a layer of electrolyte decomposition products at the cathode surface, but no experimental composition analysis has been possible due to the thinness and delicacy of this layer. Most commercial cells use electrolyte additives to develop a stable solid-electrolyte interface layer (SEI) on the surface of the anode to increase cycle life. The speciation and reaction mechanisms of these electrolyte additives are however not well understood. Moreover, the fate of the dissolved manganese atoms on the surface of the anode is still highly debated. To bridge this knowledge gap, in this dissertation reactive force field-based molecular dynamics was applied to investigate the reactions occurring at the $LiMn_2O_4$ battery electrode-electrolyte interfaces and the mechanisms of manganese

dissolution. Currently, there is no molecular dynamics (MD) force field parameterized for manganese that enables the study of this electrochemical system using computational methods. The ReaxFF model is a reactive force field that can be used to simulate the formation and dissociation of chemical bonds, and thereby help to reveal the dynamic surface reaction chemistry at the electrodes. The ReaxFF model is optimized to reproduce the density functional theory (DFT)-derived energetics of the elemental species comprising the $LiMn_2O_4$ battery cell.

The force field was validated against experimental data for high temperature methane oxidation over manganese oxide surfaces. The developed model predicts the complete oxidation of methane to CO_2 and H_2O by removal of lattice oxygen atoms, as observed in experiments. The developed force field was used to study the anode and cathode half cells of the $LiMn_2O_4$ based battery. The study reveals that fluoroethylene carbonate (FEC), a commonly used electrolyte additive, decomposes on the anode surface to yield Li_2CO_3, contrary to the widely-held belief that LiF is the decomposition product of FEC. The fate and effect of dissolved manganese ions on the anode SEI layer was also investigated. ReaxFF MD simulations reveal that manganese in the anode-electrolyte interface catalyzes the polymerization of ethylene carbonate, forming polymers that extend from the anode surface into the electrolyte.

MD simulations of the cathode half-cell reveal that the cathode-electrolyte interface layer is comprised of oxidation products of electrolyte solvent molecules such as aldehydes, esters, alcohols, polycarbonates, and organic radicals. The oxidation reaction pathways for the electrolyte solvent molecules reveal the formation of surface hydroxyl species that react with exposed manganese atoms. The presence of hydrogen

fluoride (HF) results in the formation of inorganic metal fluorides and surface hydroxyl species. Simulation results generated by ReaxFF MD are found to be in agreement with experimentally identified cathode-electrolyte interface compounds. An overall cathode-electrolyte interface reaction scheme is proposed based upon the findings from this study.

CHAPTER 1

INTRODUCTION

1.1 LITHIUM ION BATTERIES

The invention of portable power played an important role in the technological revolution, and in turn, new technological inventions with higher portable energy demands led to the invention of a wide variety of batteries. Improvements in energy storage technology came through multiple innovations in battery working mechanisms as well as battery materials, from electrolysis-based voltaic piles to intercalation-based lithium ion batteries. Fundamentally, all electrochemical cells involve conversion of chemical energy to electrical energy via redox reactions at the electrodes, with cations flowing through the electrolyte and electrons flowing through an external circuit. There are important distinctions between different types of battery cells that are based upon the electrodes and electrolyte that constitute the battery chemistry. Electrode and electrolyte materials are typically selected for their voltage, charge capacity, conductivity, weight, cost, reactivity, ease of handling, and ease of manufacture.

In lithium ion batteries (Figure 1.1), first commercialized in 1991, the discharge process involves the extraction of lithium ions from the negative electrode (de-intercalation) and insertion into the positive electrode (intercalation). In the recharge

1

process, lithium ions move in the opposite direction. Electrons are conducted through the external circuit in the direction corresponding to the movement of the lithium ions. Lithium ion batteries have high specific energy, imparting a low battery weight and high energy density, thus allowing for a low battery volume. Lithium ion batteries are therefore lighter and smaller than other rechargeable batteries. On account of this, lithium ion batteries are quickly replacing conventional alkaline and nickel based batteries in portable electronics.
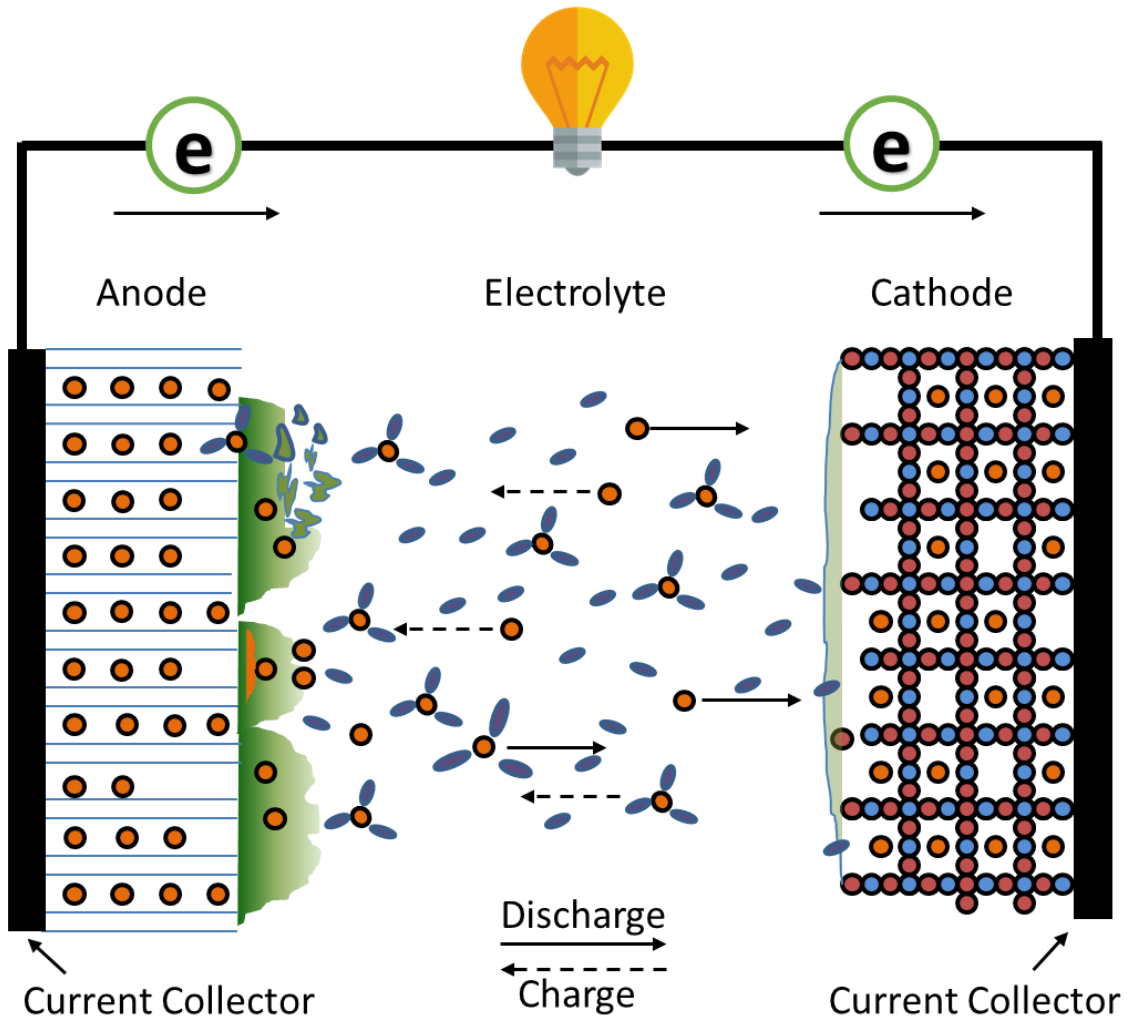
Figure 1.1 The working principle of a lithium ion electrochemical cell.

Owing to their high voltage and high charge density, lithium ion battery technology is now on the brink of revolutionizing the transportation energy sector. However, automotive applications of Li-ion batteries impose significant technological challenges. Table 1.1 lists the battery requirements for electric vehicles (EV) as proposed by the U.S. Automotive Battery Consortium (USABC). Although the theoretical capabilities of Li-ion batteries meet the requirements for EV applications, in practice, the achievable energy density, calendar life, and operating temperature of these batteries fall short of the required values. Li-ion battery chemistries are prone to a number of internal degradation mechanisms that cause capacity and power fade, thereby limiting practical capabilities. Specifically, Li-ion battery degradation occurs due to side reactions, occurring alongside the desired electrochemical redox reactions, that lead to electrolyte decomposition and electrode chemical or structural distortion[1]. A key to closing the gap between the theoretical capabilities of Li-ion batteries and their practical achievable properties is to understand and then counteract these degradation mechanisms.

Table 1.1 Goals for advanced batteries for EVs from Freedom Car/ USABC[2].

Battery attribute	Mid-Term Goals	Commercialization Goals	Long-term Goals
Power density (W/L)	250	460	600
Specific power (W/kg)	150	300	400
Energy density (Wh/L)	135	230	300
Specific energy (Wh/kg)	80	150	200
Life (years)	5	10	10
Cycle life – 80% DOD (cycles)	600	1000	1000
Sale price – 25000 units @ 40 kWh ($/kWh)	<150	<150	<100

Li-ion battery technology is comprised of a family of battery chemistries that operate on the principle of lithium ion intercalation and de-intercalation into and out of the electrodes. Various cathode and anode materials have been developed that achieve different levels of performance in terms of capacity, life, cost, and safety. For example, the most widely used anode material is graphite; whereas silicon and $Li_4Ti_5O_{12}$ both provide higher capacity as anodes, silicon undergoes excessive volume expansion upon lithium intercalation, leading to distortion of the electrode, while $Li_4Ti_5O_{12}$ has a lower voltage output in comparison to graphite[3].

Similarly, a number of cathode materials have been investigated for lithium ion batteries, including $LiNiO_2$, $LiMn_2O_4$, $LiFePO_4$ and $Li(Ni_{1/3}Co_{1/3}Mn_{1/3})O_2$. The layered structured material $LiCoO_2$ is the most commonly used cathode for electronic devices. However, $LiCoO_2$ is expensive and toxic, and hence unfit for large-scale applications like electric vehicles. The $LiMn_2O_4$ cathode material is more stable than $LiCoO_2$ on account of its three dimensional spinel structure, making it a better candidate for EV applications. The low cost and nontoxic nature of $LiMn_2O_4$ are additional merits. However, $LiMn_2O_4$ batteries have a lower capacity than $LiCoO_2$, and the higher solubility of $LiMn_2O_4$ in a liquid electrolyte can cause a more rapid capacity fade in $LiMn_2O_4$-based batteries. Aside from $LiMn_2O_4$, only lithium nickel manganese cobalt oxide $Li(Ni_{1/3}Co_{1/3}Mn_{1/3})O_2$ has also proven thus far to be a viable cathode material for EV applications[45].

1.2 KNOWLEDGE GAPS: ELECTRODE - ELECTROLYTE INTERFACE LAYERS IN $LiMn_2O_4$ BATTERY SYSTEMS

$LiMn_2O_4$ is the primary cathode material being utilized for EV applications. $LiMn_2O_4$ cathodes possess several advantages, such as low cost, nontoxicity, and a

simple preparation process[6] as compared to other cathode materials. There are, however, well-documented problems with capacity fade of lithium ion batteries containing $LiMn_2O_4$ due to active material loss, caused by the dissolution of divalent manganese from the cathode surface and deposition of dissolved manganese onto the anode. The $LiMn_2O_4$ spinel consists of manganese ions in two oxidation states (Mn^{3+} and Mn^{4+}) in equal proportion to yield a net manganese oxidation state of $+3.5$[7]. Conventional wisdom holds that trivalent manganese ions are unstable to acid attack and are lost from the cathode surface into the electrolyte following charge disproportionation through the Hunter reaction[1]:

$$2Mn^{3+} \rightarrow Mn^{4+}_{solid} + Mn^{2+}_{solution}$$
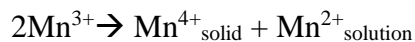
Experiments have confirmed the presence of Mn^{2+} ions in the electrolyte, but its speciation and related reaction mechanisms at the cathode-electrolyte interface are not yet fully understood. Electrochemical impedance spectroscopy (EIS) techniques have revealed the formation of a film on the cathode[8]. This film has been attributed to electrolyte oxidation driven by the reduction of unstable metal (manganese) ions in the cathode active material. The salts of these unstable metal ions are speculated to compose this cathode surface layer[9]. X-ray photoelectron spectroscopy (XPS) analyses of this layer suggest a layered structure similar to the anode solid-electrolyte interface (SEI) layer, but no further composition analysis of the cathode layer has been possible due to its thinness and delicate structure[9]. Experiments have shown that the amount of Mn^{2+} present in the electrolyte increases with charge-discharge cycling, suggesting that the cathode-electrolyte interface layer that is formed is not dense enough to form a passivizing layer and prevent further oxidation of electrolyte, as occurs at the anode SEI layer[10]. Hence, the

cathode-electrolyte interface layer can limit battery performance by consuming the electrolyte continuously as cycling proceeds.

The dissolution of divalent manganese into the electrolyte not only leads to a decrease in the effective amount of active cathode material, but also increases the anode resistance and decreases the anode capacity. Solvated Mn^{2+} ions are deposited on the anode surface. The subsequent reduction of these manganese ions results in the oxidation of lithium intercalated within the anode, thereby decreasing the Li content of the anode and reducing the overall cell capacity[11]. On account of the collective undesirable consequences of manganese dissolution and deposition in battery cells comprised of manganese-rich cathodes there is a great need to understand the reactions occurring in the cathode-electrolyte interface layer of such cells, and to develop molecular methods that can realistically simulated reactions and transport in interfacial regions not readily accessible by experiments.

1.3 ATOMISTIC METHODS

The macroscopic phenomena observed in a system are inherently the effect of atomic and molecular interactions occurring in the system. Hence, understanding and controlling the properties of matter at the level of individual atoms and molecules is a useful tool for scientific and technological advancement. The analysis of atomic and molecular interactions by experiments is not yet a reality, so we turn to computational methods to explain and predict the behavior of atomic and molecular systems. Computational methods refer to a range of techniques that simulate real systems using mathematical models. The type of computational method used to study a system depends on the size scale of the system being simulated. Figure 1.2 shows the length and time

6

scales for which different computational methods and experimental methods are applicable.
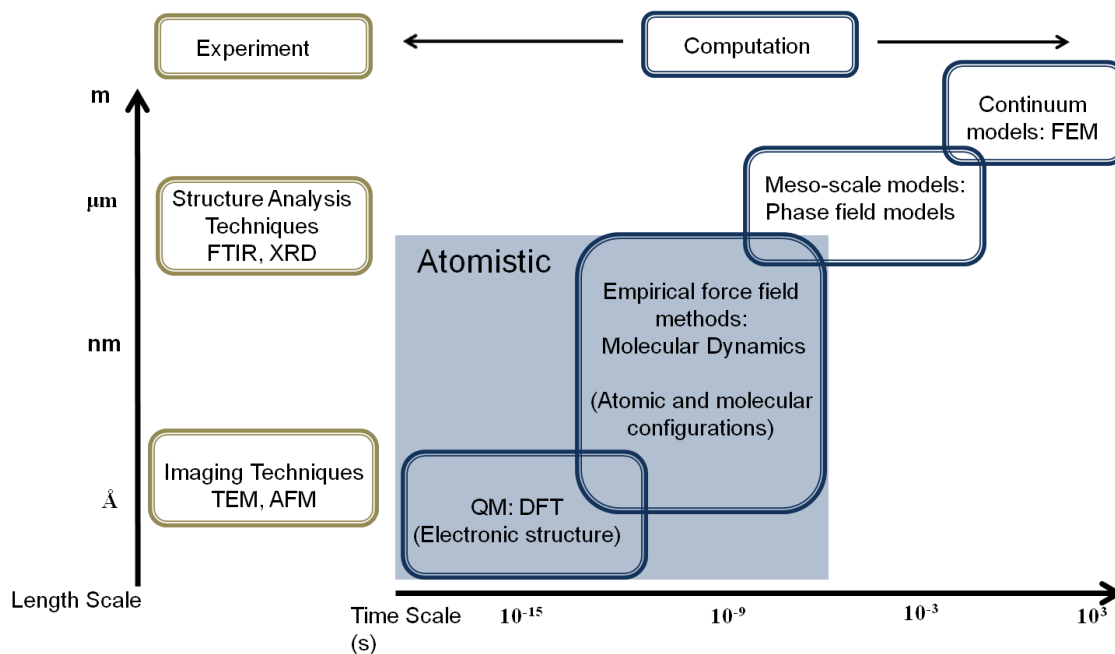
Figure 1.2 Spatio-temporal applicability scales of computational and experimental methods.

The computational methods applicable to atomic and molecular systems are called atomistic methods. Atomistic methods pose the atomic and molecular systems as an N-body problem and find solutions based on the principles of either quantum mechanics (*ab initio* methods) or classical mechanics (empirical force field methods). *Ab initio* methods and empirical force field methods differ in the time and length scales of systems they address. Within these two classes of atomistic methods, there are many sub-classes based on the approach used to achieve the desired results. Each sub-class is suited to study a particular system property or a particular application. For example, some methods can be used to study diffusion properties but not reactions, while some methods are better suited to study organic systems rather than inorganic systems. Therefore, the type of atomistic

7

method used should be carefully picked based on the size of the system under study (which determines the computational cost), the chemical nature of the system, and also the type of properties to be analyzed.

1.3.1   AB INITIO METHODS

As the name suggests, *ab initio* methods start from first principles quantum mechanics and make few approximations while deriving the explicit solution of the Schrödinger equation. Because of their modeling fidelity, *ab initio* methods usually produce more accurate and reliable results than other atomistic methods, but at a high computational cost. The computational complexity of *ab initio* calculations increase exponentially with the number of electrons simulated in the system; a consequence of the non-local approach of *ab initio* methods. Many approaches have been developed to overcome the limitations of *ab initio* methods out of which density functional theory (DFT) based approaches have delivered the best accuracy and performance in most cases[12]. DFT uses electron density functions to calculate the ground state electronic structure of many body systems based on the Hohenberg and Kohn theorems[13]. DFT can predict a great variety of molecular properties such as molecular structures, vibrational frequencies, atomization energies, ionization energies, electric and magnetic properties, and reaction pathways[14]. DFT is the most popular *ab initio* method, but its accuracy is limited to roughly 1000 atoms and time scales of a few picoseconds, limiting the scope of its application to sub-nanoscale systems[15]. Systems of this length and time scale are rarely sufficient to observe the phenomena of interest in real-life problems.

1.3.2 CLASSICAL METHODS

The second class of atomistic methods is the empirical force field methods (also called molecular dynamics methods) based on the principles of classical mechanics. These methods model the behavior of physical systems using a set of discrete entities (for example, atoms) and a set of interactions among them (empirical force fields). Simulation techniques solve the equation for many bodies by discretizing time and integrating particle behavior over discrete time steps. The behavior of these particles is governed by Newton's Second Law. At each time-step, the force, acceleration, velocity, and position of the discrete entities are calculated by minimizing the total energy of the system, thus generating spatio-temporal evolution of the system. Empirical force field methods extend the applicability of atomistic methods to the nanoscale, making it possible to study phenomena like diffusion and reaction dynamics from the atomic point of view[16]. Empirical force field methods, unlike *ab initio* methods, do not treat electrons explicitly. Instead, the atomic nucleus and the orbital electrons are modeled as a single entity, thus making the problem "local". The interactions between these atomic particles are approximated by means of functional forms and parameters. Often, the force fields are dependent on a large number of tunable parameters. Evaluation of these parameters is a critical step in the modeling process. Typically, all parameters are tuned iteratively to match well-studied experimental properties of the target real-system or properties derived from *ab initio* methods[17].

Force fields describe the energy and forces between interacting particles in terms of particle positions. There are three types of particle interactions that contribute to the energy described by a force field: bonded interactions, short-range interactions, and long-

range interactions. Bonded interactions are covalent bonds, valence angle interactions, and dihedral (torsion) interactions. These types of interactions typically take place within the range of a few angstroms and constitute a very small portion (1-5%) of the computational complexity of an MD model. The short-range interactions refer to van der Waals interactions, whereas the long-range interactions refer to electrostatic interactions. The short-range and long-range interactions are collectively known as the non-bonded interactions, and their computation may account for up to 99% of the total computation cost[12]. The simplest force fields that use functional forms resembling Hooke's Law (i.e., the spring model) to represent the bonded terms are known as classical force fields. DRIEDING[18], UFF[19], AMBER[20], and CHARMM[21] are among the most well-known classical MD force fields. These force fields have been used to study the properties of metals, inorganic and organic molecules, as well as to successfully predict protein folding and function.

While classical MD force fields are successful in reproducing various properties of molecular systems, they have limitations. Some of these limitations are as follows:

(i) Classical MD force fields do not allow for changes in bonds during simulations. Therefore, they cannot be used to model reactive systems.

(ii) Classical force fields describe electrostatic interactions in terms of fixed and atom-centered charges that are not representative of the real system, where atoms and molecules are prone to polarization depending on the environment. Such polarization strongly affects the geometry and energetic of molecular systems and is not accounted by classical force fields.

(iii)   Due to system-specific parameterization, classical force fields are not generic and hence they are not transferable[17].

Various modifications of MD force field models have been proposed to target the aforementioned limitations, including polarizable force fields, mixed quantum mechanics coupled molecular mechanics, and reactive force fields[22]. There have also been efforts to develop newer force fields that overcome some, if not all, of the limitations listed above. These are discussed in the next section.

POLARIZABLE FORCE FIELD METHODS

Polarizable force fields account for variations in the charge distribution during a molecular simulation. Force fields account for polarization by employing either inducible point dipole methods or fluctuating charge models[23]. Polarizable force fields provide a far superior physical description of organic and bio-molecular systems than non-polarizable force fields, and have demonstrated to be useful in determining the directionality and energetics of hydrogen bond formation and cation-aromatic interactions[24]. The inclusion of a polarization model into the functional form of the force field does however result in increased complexity during force field development, due to the increased number of parameters that require tuning[25].

MIXED QM/MM METHODS

Another important limitation of classical force fields is their inability to simulate reactions. This limitation is the result of classical force fields using static bonds; i.e., they do not allow for the formation of new bonds or for bond dissociation during a MD simulation. Mixed quantum mechanics/molecular mechanics methods provide an option

for the study of small-scale reactive systems. Here, QM methods are used to simulate the reactive region of the system, while molecular dynamics methods are applied to the rest of the system.

The computational cost of the mixed QM/MM simulation technique depends on the size of the reactive region where quantum mechanics methods are used. The larger the reactive region, the higher the computational cost. The most challenging part of a mixed QM/MM simulation is the bridging of the reactive and non-reactive regions using different modeling regimes. Long-range interactions can be used to efficiently integrate the QM and MM regions for systems that do not have covalent bonds that span the two regions. The complexity of coupling the regions increases greatly however if there are covalent bonds that bridge the reactive and non-reactive regions. Although QM/MM mixed techniques have been used to study systems with localized reactive regions, their application to larger reactive systems has been limited due to several factors, including *a priori* uncertainty regarding the location of the reactive region; size limitations on the reactive regions; loss of information that occurs when coupling the QM and MM regions; and the general intricacy required to set up and execute a mixed QM/MM simulation[17].

REACTIVE FORCE FIELDS

An alternative approach to overcome the limitations of classical force fields are force fields that are based on bond order. These techniques mimic the quantum overlap of electronic wave functions through a bond order term that describes the bonds in the system dynamically, based on the local neighborhood of each atom. The concept of bond order-based force fields was first developed by Tersoff[26]. The second generation of bond order based potentials were REBO[27] and AIREBO[28] which, despite being widely used at

the time of their introduction, incur fundamental problems in the shape of the dissociation and reactive potential curves. The ReaxFF method[29] of van Duin *et al.* is the first reactive force field that contains both dynamic bonds and polarization effects in its formulation. The ReaxFF method calculates bond orders from interatomic distances that are continuously updated at every MD or energy minimization (MM) iteration step, thus allowing for changes in atom connectivity. All of the energy bonding terms of the potential are made dependent upon the bond order, thereby ensuring that the energies and forces associated with bonding go to zero upon dissociation (Figure 1.3). ReaxFF also describes non-bonded interactions between all atoms, irrespective of their connectivity. Excessive short-range repulsive or attractive non-bonded interactions are circumvented by the inclusion of a shielding term in the van der Waals and Coulomb interactions. The ReaxFF method also calculates the charge distribution in the system at every iteration timestep. A charge equilibration (QEq) procedure approximates the partial charges on atoms by minimizing the electrostatic energy of the system.

$$BO_{ij} = \sum_{t=\sigma,\pi,\pi-\pi} exp\left[p_{bo,1} \left(\frac{r_{ij}}{r_o^t} \right)^{p_{bo,2}} \right]$$
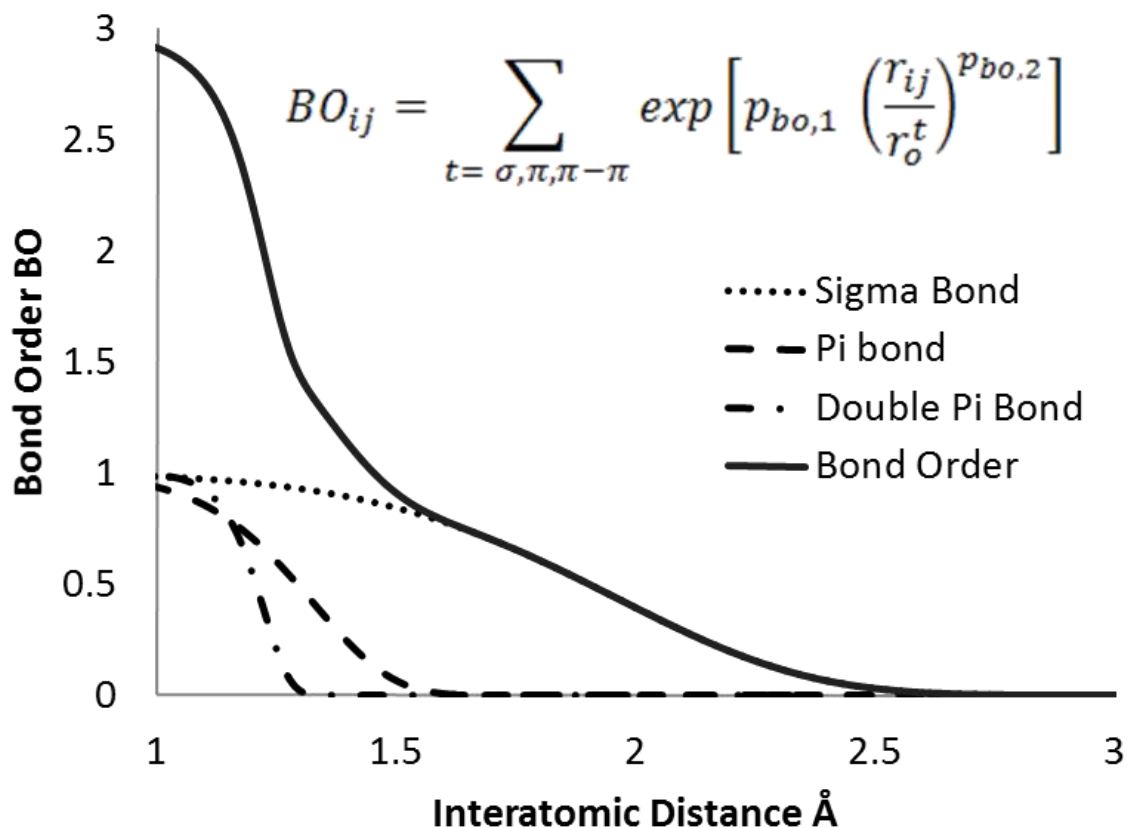
Figure 1.3 Bond-order/bond-length relationship for C-C interactions. The ReaxFF method allows for a smooth transition from non-bonded to single, double, and triple bonded interactions between the two carbon atoms. All connectivity-dependent interactions are made bond-order dependent, ensuring that their energy contributions disappear upon bond dissociation.

The most important feature of the ReaxFF is its transferability to a wide range of chemical environments, irrespective of the application for which it was developed. The parameters for ReaxFF method are based on the element under consideration; e.g., the ReaxFF metal oxide oxygen is described by the same parameters as the ReaxFF oxygen in organic molecules. Similarly, ReaxFF does not have separate sp^2 and sp^3 atoms for carbon, as the method determines the atom's hybridization (i.e., bond order) from its chemical environment[30].

The ReaxFF method has been applied to a wide variety of systems, including hydrocarbon reactions[29], transition-metal-catalyzed nanotube formation[31], high-energy materials[32], and interfacial reactions[33]. The reactive force field method is computationally more expensive than MD simulations that employ classical force fields, due to the additional calculations required to determine bond orders and charge distributions. In spite of this added computational expense, the development and use of ReaxFF is growing rapidly, owing to its ability to predict reactions accurately[34].

1.4 KNOWLEDGE GAPS: REACTIVE FORCE FIELDS FOR THE LiMn$_2$O$_4$ BATTERY SYSTEM

Atomistic simulation methods have proven useful for probing molecular-scale systems beyond the reach of experimental techniques. As previously noted, current experimental capabilities are inadequate to perform accurate chemical analyses of the electrode-electrolyte interface layers of LiMn$_2$O$_4$ battery cells. The reactions at the cathode-electrolyte interface layer occur within the spatial range of a few nanometers from the cathode surface, and can thus be investigated by molecular dynamics using reactive force field methods. One difficulty, however, is that there are no fully developed force fields to simulate the reactions involving manganese that are of primary interest in this study, specifically the formation of the dynamic cathode-electrolyte interface layer. This gives rise to the need for the development of a reactive force field to study the LiMn$_2$O$_4$ battery system. A ReaxFF model has already been developed to simulate interactions between three (C, H, O) of the seven elements (C, H, O, Mn, Li, F, P) in the LiMn$_2$O$_4$ battery cell. Thus, in order to investigate the nanoscale phenomena occurring at the LiMn$_2$O$_4$ and graphite electrode-electrolyte interfaces, the ReaxFF model needs to be

expanded to include the full set of optimized pairwise ReaxFF parameters for lithium, manganese, fluorine, and phosphorus.

1.5 DISSERTATION OUTLINE

This dissertation sets out to develop a ReaxFF model for the complete set of element interactions found in a battery system consisting of a $LiMn_2O_4$ cathode, a graphite anode, an ethylene carbonate/dimethyl carbonate electrolyte, and a lithium hexafluorophosphate electrolyte salt. The optimized ReaxFF model is then used to investigate the following research questions:

i.   The fate of dissolved manganese atoms in the anode-electrolyte interface layer. Specifically, identifying the manganese compounds present in the layer and investigating the effects of manganese atoms on the stability of the anode-electrolyte interface layer.

ii.   The overall reaction mechanisms that result in the formation of the cathode-electrolyte interface layer. This work will probe the species that comprise this layer, the reaction pathways for cathode dissolution, and the role of impurities in the dissolution reaction.

Chapter 2 discusses the optimization process of the ReaxFF model for the elemental interactions that will completely describe the $LiMn_2O_4$ battery system, as shown in Figure 1.4. This chapter further discusses the validation of the developed ReaxFF model by studying the reduction of manganese oxides in the presence of methane using ReaxFF based molecular dynamics. The developed ReaxFF model not only

accurately predicts experimentally observed products of manganese oxide reduction with methane, but also reveals reaction intermediates.

Elements in the LiMn₂O₄ system		Interactions optimized by this work		Published ReaxFF parameters		Interactions to be included in future	
	Mn	**F**	**Li**	**O**	**H**	**C**	**P**
Mn							
F							
Li							
O							
H							
C							
P							

Figure 1.4 Element interactions that comprise the LiMn₂O₄ battery system. The figure highlights the interactions for which the ReaxFF model parameters are being optimized by this work.

The investigation of the anode-electrolyte layer is discussed in Chapter 3. This layer has been widely studied using experimental methods as well as computational methods. Hence, starting the ReaxFF analysis from the anode layer will be useful in further validating the developed model. The analysis of the anode-electrolyte interface layer starts with probing the decomposition of fluoroethylene carbonate (FEC), an electrolyte additive used to develop a thermally stable anode-electrolyte interface layer. While is it known that FEC is decomposes faster than the other electrolyte solvents, its speciation on the anode surface is not yet well understood.

On analyzing the fate of FEC, the ReaxFF model successfully predicted the ability of FEC to decompose before the other electrolyte solvent molecules and also revealed the decomposition products of FEC. Chapter 3 also addresses the fate of dissolved manganese ions in the anode-electrolyte interface layer. Manganese compounds formed in the layer are discussed, and the simulations reveal insights into the detrimental effects of Mn ions on the stability of a developed anode-electrolyte interface layer.

Chapter 4 explores the cathode-electrolyte interface layer using the ReaxFF model introduced in Chapter 2. Specifically, the reaction pathways leading to the formation of the compounds comprising the layer are investigated. The manganese dissolution reaction mechanism is reported, and the effect of HF impurities on the dissolution reaction are described. Chapter 4 also addresses the overall reaction mechanism that occurs on the cathode surface, and provides evidence for its non-passivated nature, resulting in the ongoing degradation of the cathode and electrolyte compounds.

This dissertation investigates and reports on the nanoscale phenomena that lead to macroscopic performance losses in batteries, and yields insights that can help in developing high capacity, long life, low cost energy storage devices. The reactive force fields and DFT property compilations developed in this research will serve as valuable additions to the body of knowledge on interatomic potentials that are used by researchers in many disciplines of science and engineering.

CHAPTER 2

OPTIMIZATION AND VALIDATION OF THE REAXFF MODEL FOR LITHIUM MANGANESE OXIDE BATTERY SYSTEMS

The reactive MD model, ReaxFF[35], developed by van Duin *et al*. is an empirical force field that is based on bond order/bond length relationships enabling the prediction of bond formation and dissociation during molecular dynamics simulations. In order to simulate bond formation and dissociation, all the energy terms in the ReaxFF model are based on bond order/bond length relationships. This allows for a smooth transition of the energy and forces in the system, even during reactions. The energy and bond order terms that describe the ReaxFF model are explicated by previous work[36]. The ReaxFF model is one of the more successful reactive force fields and has been used to study over 150 different systems including hydrocarbon oxidation[37], pure metallic systems[38] and catalytic activity of other transition metal oxides[36]. The ReaxFF model has also been used to simulate the SEI layer reactions on lithium anodes[39] in good agreement with experimentally observed results which further validates the application of the ReaxFF model for the $LiMn_2O_4$ battery system under consideration in this study. The success of the ReaxFF model over other reactive force fields is due to its transferability to a wide range of chemical environment irrespective of the application for which it was developed.

The parameters for the ReaxFF method are based on the element under consideration, i.e., the ReaxFF metal oxide oxygen is described by the same parameters as the ReaxFF oxygen in organic molecules[30]. This feature enables researchers to build on previous ReaxFF development for similar systems.

The lithium manganese oxide ($LiMn_2O_4$) battery system under study by this work uses the $LiMn_2O_4$ spinel as cathode, graphite as anode, ethylene carbonate (EC) and dimethyl carbonate (DMC) as the electrolyte solvents, lithium hexafluorophosphate ($LiPF_6$) as the electrolyte salt, and fluoroethylene carbonate (FEC) as the electrolyte additive. This study uses parameters developed by Chenoweth *et al*. to describe the interactions between carbon, hydrogen and oxygen[37], the parameters developed by Han et. al to describe the lithium interactions[40] and optimizes the ReaxFF model parameters for manganese and fluorine interactions.

The system under study also contains the element phosphorus in the form of $LiPF_6$ salt. Decomposition of this salt into highly reactive phosphorus compounds and hydrogen fluoride plays an important role in the composition of the SEI layer on the electrode surfaces[41]. The simulation of these complex decomposition reactions requires additional ReaxFF model training that are able to capture the reaction chemistry as well as reaction kinetics of $LiPF_6$ decomposition. As this is the first study to investigate the reactions occurring at the electrode-electrolyte interfaces using reactive molecular dynamics, we limit the scope of the study to reaction chemistry of the electrode material and the electrolyte solvent compounds. The absence of $LiPF_6$ salt decomposition under the conditions in this study has not been proved or speculated but this assumption simplifies the system without compromising the purpose of the study. In doing so, the

ReaxFF model parameters for phosphorus are constrained to interactions with fluorine that can simulate the dissociation of LiPF$_6$ into Li$^+$ and PF$_6^-$ but keeps the PF$_6^-$ anion intact throughout the simulation.

2.1 TRAINING SET FOR LITHIUM MANGANESE OXIDE SYSTEM

The application of the ReaxFF model to a system involves firstly, the optimization of the ReaxFF parameters to reproduce the quantum mechanics derived energetics for all the atomic interactions in the system and secondly, molecular dynamics simulations of the system using the optimized ReaxFF. Figure 2.1 is a schematic of the ReaxFF model optimization process. The optimization process of the ReaxFF model starts with assembling a database of quantum mechanics (called the training set) generated geometries, energetics, and charge distributions of a broad spectrum of compounds that contain the elements for which the ReaxFF model interactions parameters are to be optimized; manganese and fluorine are the elements of interest in this study.
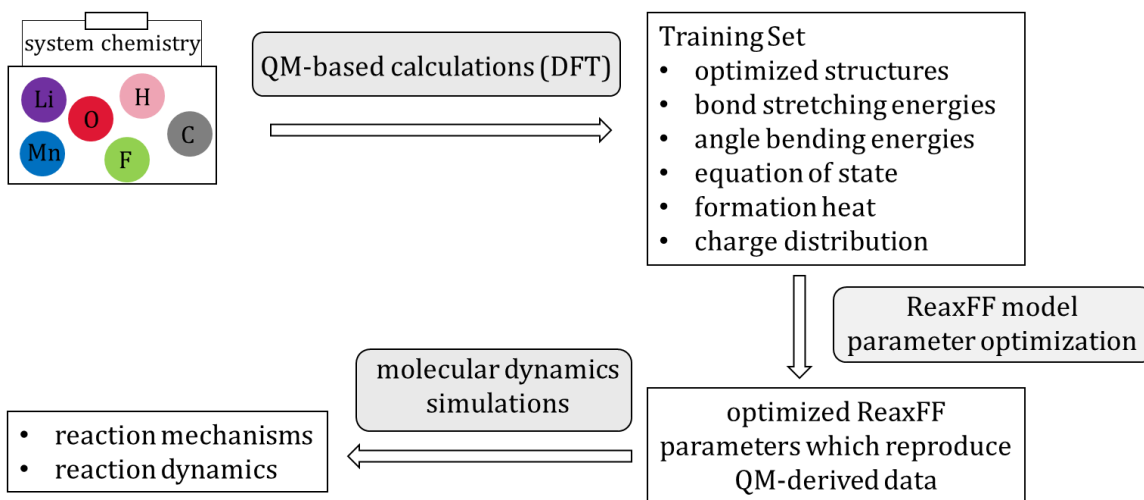

Figure 2.1 Schematic of the ReaxFF model optimization process.

The compounds included in the training set for the LiMn₂O₄ battery system are shown in Figure 2.2. The compounds in the training set were selected to represent the complete chemistry of manganese and fluorine in a lithium ion battery electrochemical cell. To ensure transferability of the developed force field to systems beyond of interest in this study, the ReaxFF model has been optimized to reproduce QM derived properties of nearly 1500 structures of the condensed phases and molecules of compounds in the training set. Some of the structures included in the training set are thermodynamically unfavorable; the energetics of these structures train the ReaxFF model to identify high energy configurations that are unlikely to occur during the MD simulations.

	Mn	F	Li	O	H	C	P
Mn	α-Mn β-Mn bcc-Mn fcc-Mn sc-Mn	MnF_2 MnF_3 MnF_4	$LiMnF_4$	MnO MnO_2 (α, β, λ) α-Mn_2O_3 α-Mn_3O_4	$Mn(OH)_2$	Mn_3C	
F		F_2		OF_2 O_2F_2	CH_3F, CF_4		$LiPF_6$
Li	$LiMnO_2$ $Li_xMn_2O_4$, x= 0-1	LiF	Li_2O	Li_2O_2	LiH	CH_3Li	
O	111, 100, 110 $LiMn_2O_4$ surface	OF_2		O_2	H_2O	C_2Li_2	
H	HMnOH	HF					
C	$Mn(CH_3COO)_2$ $MnCO_3$	CF_4	CH_3COOH		C_2H_2	C_2H_6	
P	$Mn(PF_6)_2$						

Elements in the LiMn₂O₄ system	Compounds added to the training set	Published ReaxFF parameters

Figure 2.2 Compounds included in the training set for LiMn₂O₄ ReaxFF model optimization.

2.2 METHODS

2.2.1 DENSITY FUNCTIONAL THEORY CALCULATIONS

The quantum mechanics based training set was developed by conducting periodic and non-periodic density functional theory calculations.

PERIODIC CALCULATIONS

The periodic calculations were conducted to obtain the equations of state and heats of formation of condensed phases. The equation of state was obtained by conducting individual calculations on condensed phase structures with volumes varying between 0.7 and 1.3 times the equilibrium structure. The heat of formation for each condensed phase was calculated based on the most stable pure phase, α-Mn for manganese, bcc structure of metallic lithium, graphite for carbon, molecular H_2, O_2, and F_2 for hydrogen, oxygen and fluorine respectively. Periodic calculations were performed using CASTEP[42] in the Material Studio software environment. The Vanderbilt ultrasoft psuedopotential was used to model the core electrons and Perdew-Burke-Ernzerhof (PBE) generalized gradient approximation was used to describe the electron exchange correlation functional. Plane wave cutoff energy was set to 500eV. The Brillouin zone was sampled using the Monkhorst-Pack scheme with grid of size 8x8x8 kpoints.

NON-PERIODIC CALCULATIONS

Non-periodic calculations on clusters and molecules of training set compounds were conducted to obtain changes in energy due to bond stretching and angle bending, and charge distribution in the compounds. The bond stretching energy curves were obtained by changing the bond length between two atoms in the compound while keeping

23

all other structural parameters constant. The bond lengths are varied between 1 Å – 5 Å. Similar calculations were conducted to obtain the angle bending energy curves. Valence and torsion angles were varied between 60º and 180º keeping all other structural parameters constant. The ReaxFF charge parameters were optimized to Mulliken charges calculated using DFT programs. Non-periodic calculations were carried out using the GGA BLYP functional as implemented in the DMol3[43] program of the Material Studio software package. Double numerical plus polarization (DNP 4.4)[44] atomic orbital basis set was used to describe all electrons (relativistic) explicitly. The DFT functionals used in this work were chosen to describe all compounds in the training set to an agreeable degree of accuracy, in the process compromising the accuracy for individual compounds which may have been obtained by a different choice of functionals.

2.2.2 REAXFF PARAMETER OPTIMIZATION

The ReaxFF model parameters are optimized successively (single parameter search optimization) to minimize the sum squared error between QM values and values predicted by the model[45] using the standalone ReaxFF code developed by van Duin *et al*[35].

2.3 RESULTS

2.3.1 REAXFF MODEL FOR LITHIUM MANGANESE OXIDE SYSTEM

The ReaxFF model was optimized to include the interaction parameters of manganese and fluorine with carbon, oxygen, hydrogen and lithium as well as interaction parameters between manganese and fluorine. The results of the optimization process for each pair of interactions is detailed below.

MANGANESE - MANGANESE INTERACTIONS

The manganese-manganese interaction parameters are optimized against metallic manganese cohesive energies, equations of state and relative stability of 5 metallic phases. The five phases of manganese included in the training set are α-Mn (stable temp range: 0 K – 1000 K), β-Mn (stable temp range: 1000 K – 1370 K), fcc-Mn (stable temp range: 1370 K – 1410 K), bcc-Mn (stable temp range: 1410 K – 1500 K), and sc-Mn which is a high pressure structure. Figure 2.3 shows the equations of state of manganese metal phases calculated by ReaxFF and DFT. ReaxFF predicts the relative stabilities of the phases as α-Mn > β-Mn > fcc-Mn > bcc-Mn > sc-Mn which is in agreement with the experimentally determined[46] order and DFT calculations. ReaxFF also predicts the lattice expansion and compression energy changes in good agreement with DFT except for the high density structures of the fcc phase. These high density structures of the high temperature phase are not realistic; hence, it is not of utmost importance to be captured accurately by the model. However, ReaxFF predicts the fcc equilibrium structure to be 2.45 kcal/mol higher in energy than α-Mn, which is in good agreement with the DFT value of 2.28 kcal/mol, showing that ReaxFF is able to predict the energetics of the fcc phase.
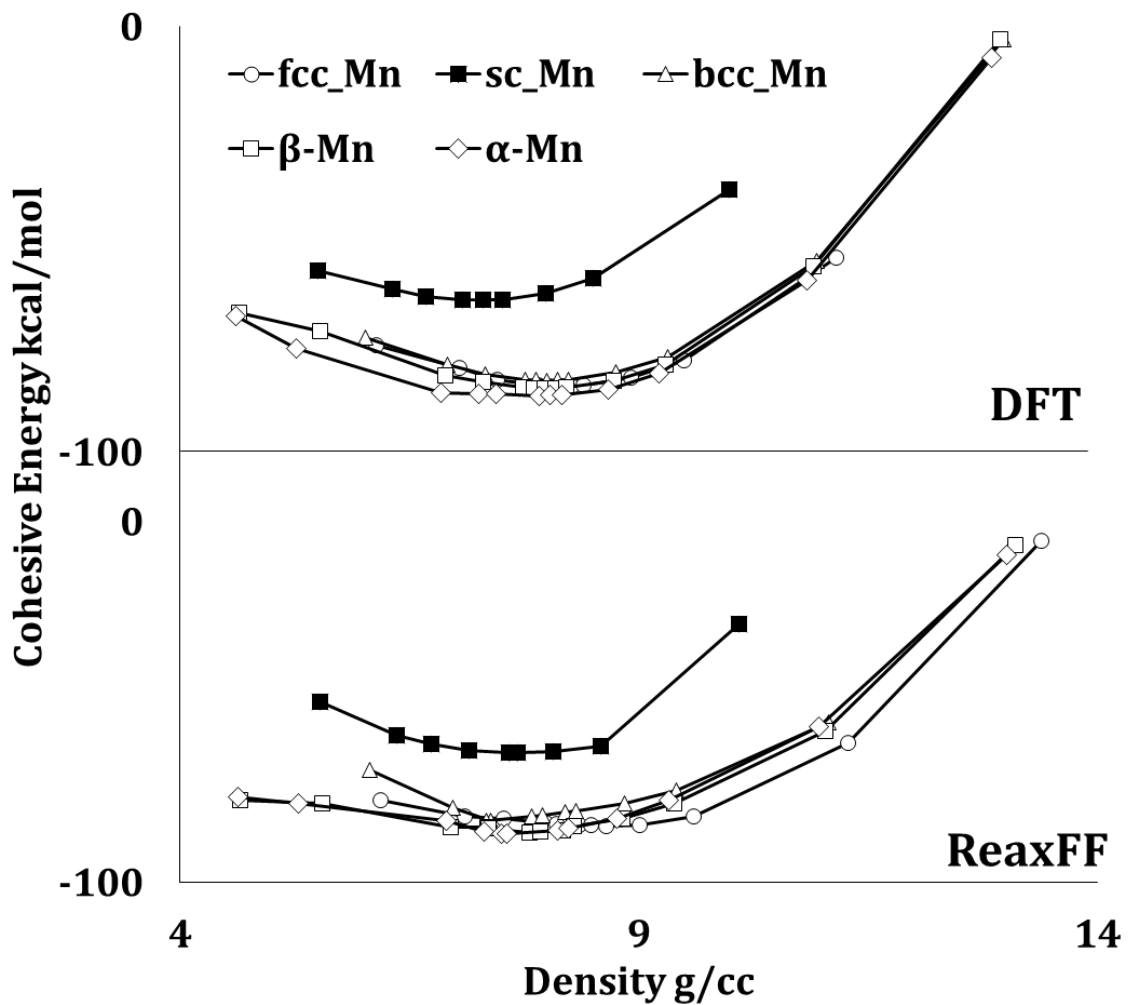
Figure 2.3 Equations of state of five metallic manganese phases as predicted by ReaxFF and DFT.

Table 2.1 compares other ReaxFF predicted properties of manganese metal with DFT value calculated by this work, DFT value reported by others and experimentally observed values. ReaxFF predicts the density of α-Mn as 7.75 g/cc, which is within 3% error of the experimentally predicted value of 7.47 g/cc[47]. The cohesive energy of the most stable phase α-Mn as determined by ReaxFF is 86.52 kcal/mol, which is in very close agreement with the DFT predicted value of 86.75 kcal/mol. The theoretical

predictions of manganese cohesive energy differ largely from the experimentally calculated value. While it is known that manganese has unusual properties as compared to other transition metals (e.g., low boiling point) which can be attributed to low cohesive energies, the experimental value cited here has been extrapolated from high temperature data making it less reliable. However, it is important to note that theoretical methods overestimate metallic manganese cohesive energies.

Table 2.1 Properties of the stable metallic manganese phase predicted by the ReaxFF model compared to DFT values predicted by this work, and DFT and experimental values reported in literature.

Property	ReaxFF	DFT		Exp.
Lattice constant Å	8.85	8.71	8.64[48]	7.47[47]
Cohesive Energy kcal/mol	86.54	86.75	88.32[49]	67.5(298 K)[46]
Stable phase	alpha	alpha	alpha[48]	alpha[47]

MANGANESE INTERACTIONS WITH OXYGEN

Manganese oxides occur in multiple manganese oxidation states and in order to capture the ability of manganese cations to change oxidation states readily, a combination of manganese oxide condensed phases and small molecules were included in the training set (Figure 2.2). Specifically, the three common oxide oxidation states (Mn^{2+}, Mn^{3+}, Mn^{4+}) were represented by MnO, Mn_2O_3 and MnO_2 condensed phases and molecules. Further, structural properties were represented by including three different phases of MnO_2 crystal (α-MnO_2, β-MnO_2 and λ-MnO_2). To capture the features of manganese-oxygen interactions, the ReaxFF parameters were trained against condensed phase properties like equations of state, heats of formation, lattice constants and small molecule

properties like equilibrium bond distance, bond dissociation energies, valence angle energies and molecular charge distribution.

Figure 2.3 compares the heat of formation of the manganese oxides. The heats of formation have been calculated relative to ground state α-Mn phase and dioxygen gas molecule. ReaxFF accurately predicts β-MnO$_2$ as the stable manganese oxide phase with heat of formation of 122.90 kcal/mol which is within 2% error of the experimental value[50] 124.63 kcal/mol. Table 2.2 compares the lattice constants of manganese oxides predicted by ReaxFF with DFT predicted and experimentally determined values. ReaxFF reproduces the DFT lattice constant within 3% error.

Table 2.2: Lattice constants of manganese oxides as predicted by ReaxFF compared to DFT and experimental values.

Phase	Lattice parameter	ReaxFF Å	DFT Å	Exp[51] Å
α-MnO$_2$	a=b	10.04	10.09	9.96
	c	2.78	2.79	2.85
β-MnO$_2$	a=b	4.52	4.50	4.39
	c	2.96	2.86	2.87
λ-MnO$_2$	a=b=c	8.23	8.31	8.04
MnO	a=b=c	4.36	4.51	4.44
α-Mn$_2$O$_3$	a=b=c	9.34	9.21	9.41
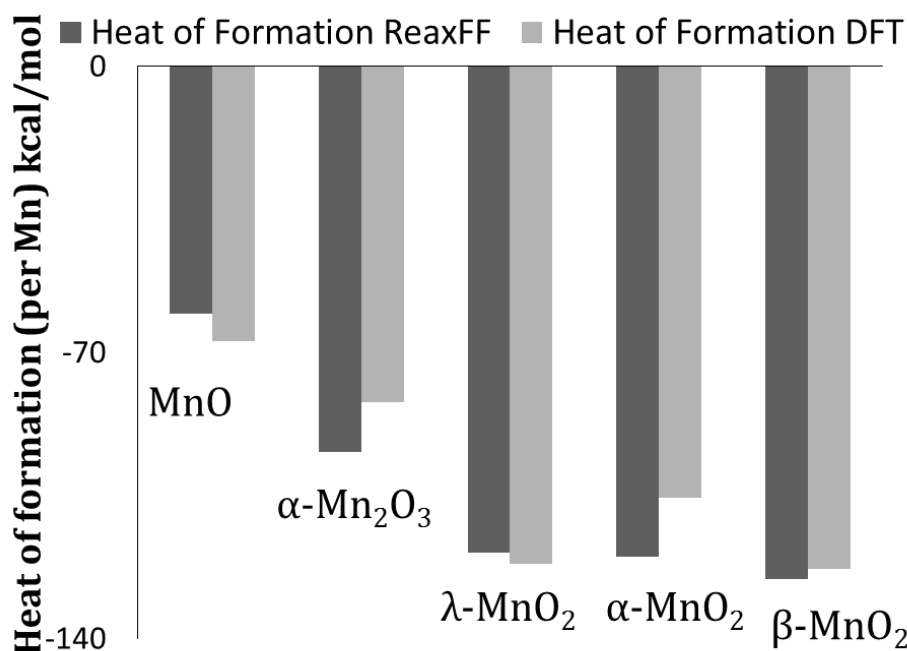
Figure 2.3 Heats of formation of manganese oxide condensed phases. The experimentally calculated heat of formation for β-MnO_2 is -126.3 kcal/mol[50], ReaxFF model predicts the value within 2% error.

The optimization results for manganese-oxygen bond energy curves, angle bending energy curves and charge distribution are given in Figure 2.4, Figure 2.5 and Figure 2.9. The optimum bond length between Mn and O in a MnO and MnO_2 molecule by ReaxFF is 1.56 Å, which compares well with the DFT predicted value of 1.61 Å. The Mn_2O_3 molecule has two types of bonds between Mn and O, which are both captured by ReaxFF as 1.56 Å (DFT: 1.61 Å) and 1.83 Å (DFT: 1.80 Å). ReaxFF predicts the bond dissociation energy of the Mn-O bond as 92.5 kcal/mol, which is in good agreement with the experimental value of 96 kcal/mol[52]. Further, reaction energies for oxidation and reduction reactions of manganese oxides were used to validate the ReaxFF model shown in Table 2.3.
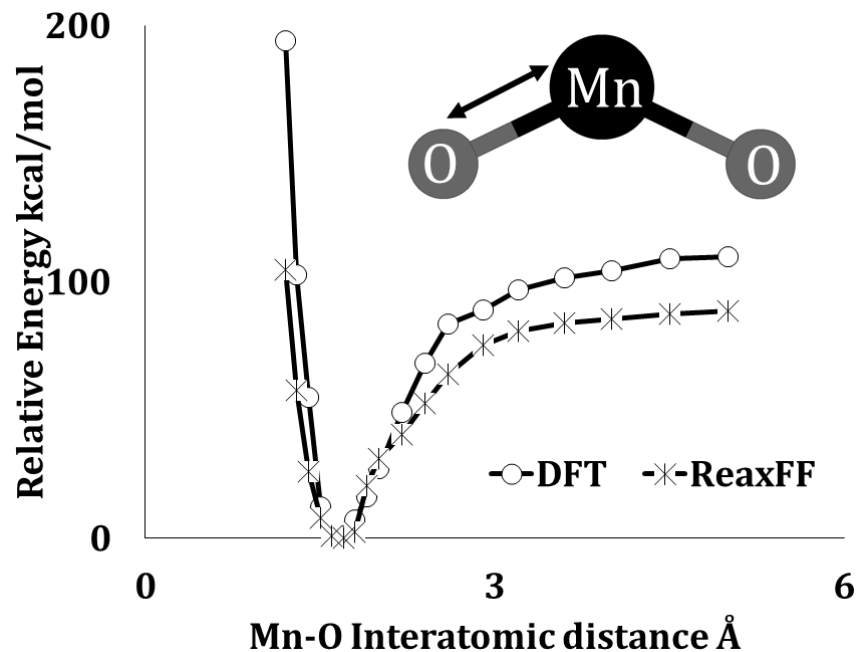
Figure 2.4 Mn-O bond stretching energy curve in MnO_2 molecule. Energy of each structure is calculated relative to the optimum geometry of MnO_2.
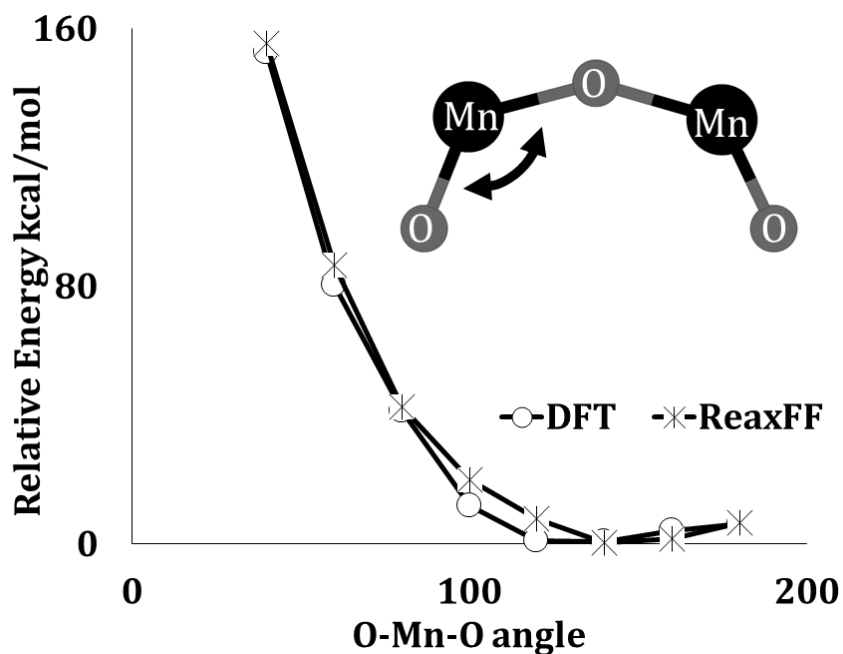
Figure 2.5 O-Mn-O angle in the Mn_2O_3 molecule. Energy of each structure is calculated relative to the optimum geometry of Mn_2O_3.

Table 2.3 Reaction enthalpies as predicted by ReaxFF and DFT. All energies are given in kcal/mol.

Reaction	ReaxFF	DFT
$Mn + \frac{1}{2} O_2 \rightarrow MnO$	-10.00	-12.58
$MnO_2 + H_2 \rightarrow MnO + H_2O$	-20.75	-18.98
$MnO_2 + 2C \rightarrow Mn + 2CO$	-67.11	-64.74
$MnCO_3 \rightarrow MnO + CO_2$	19.26	22.05

MANGANESE INTERACTIONS WITH HYDROGEN

Manganese-hydrogen interactions were represented through the bond dissociation energies and valence angle bending energies for $Mn(OH)_2$ and the HMnOH molecules. HMnOH molecule is a short lived intermediate during reaction of Mn with water that has been identified using matrix-isolation FTIR at 15 K[53]. Even though HMnOH molecule is not stable, for the purpose of ReaxFF development, the energetics of this molecule give valuable information about the interactions between manganese and hydrogen.

The Mn-H interaction parameters of ReaxFF were fit to H-Mn bond energy curve (Figure 2.6) and H-Mn-O angle distortion in HMnOH molecule and the Mn-O-H angle distortion in $Mn(OH)_2$ (Figure 2.7). The formation energy of HMnOH was predicted by ReaxFF as 40.72 kcal/mol, which is close to the DFT value of 48.18 kcal/mol.
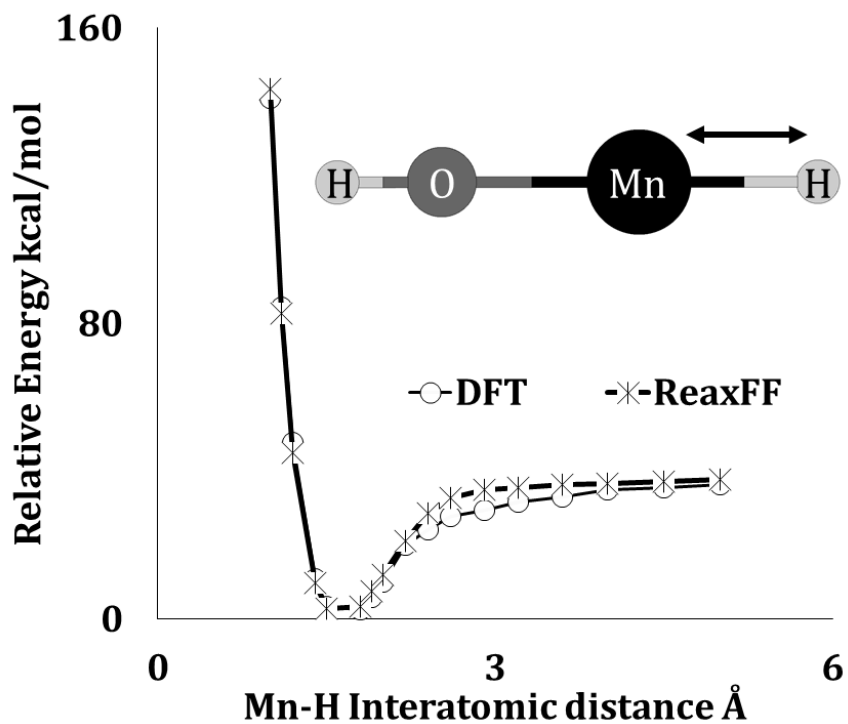
Figure 2.6 Mn-H bond stretching energy in HMnOH molecule. Relative energy is calculated with respect to the optimum geometry of HMnOH.
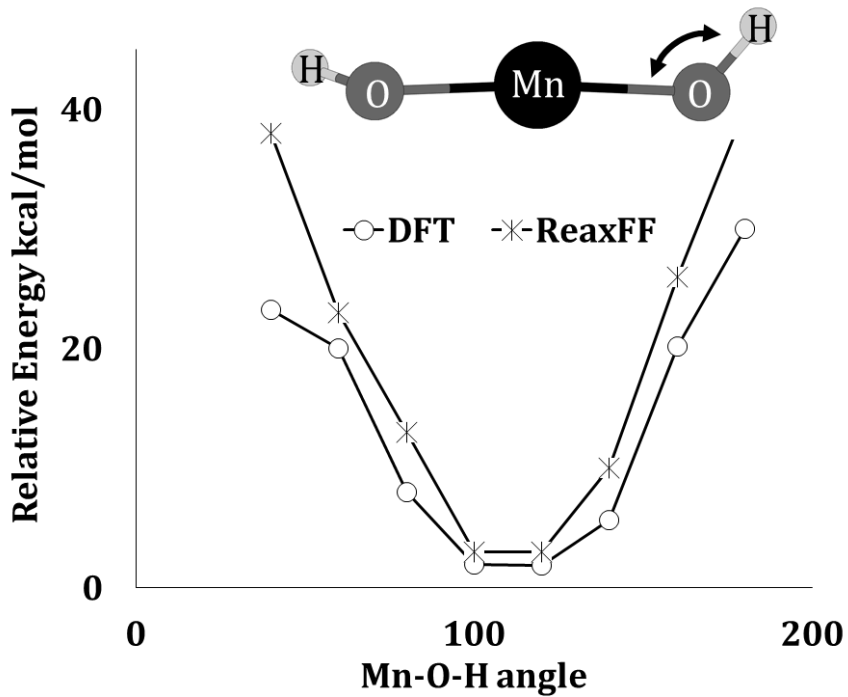
Figure 2.7 Mn-O-H angle bending energy in Mn(OH)$_2$ molecule. Relative energy is calculated with respect to the optimum geometry of Mn(OH)$_2$.

MANGANESE INTERACTIONS WITH CABRON

Bond dissociation energy curves, optimum geometries and charge distributions in MnC and $MnCO_3$ are included to describe the interactions between manganese and carbon.

The manganese carbon interaction energy was fit to the bond stretching energy in a MnC molecule (Figure 2.8). ReaxFF predicts the equilibrium bond distance between manganese and carbon to be 1.78 Å, within 3% error of the DFT predicted value of 1.73 Å. The heat of formation of MnC is predicted as 78.45 kcal/mol as compared to the DFT value of 70 kcal/mol[54]. The ReaxFF has also been trained to predict the charge distributions in the manganese molecules included in the training set. Figure 2.9 shows that ReaxFF predicts the Mulliken charges calculated using DFT with good accuracy.
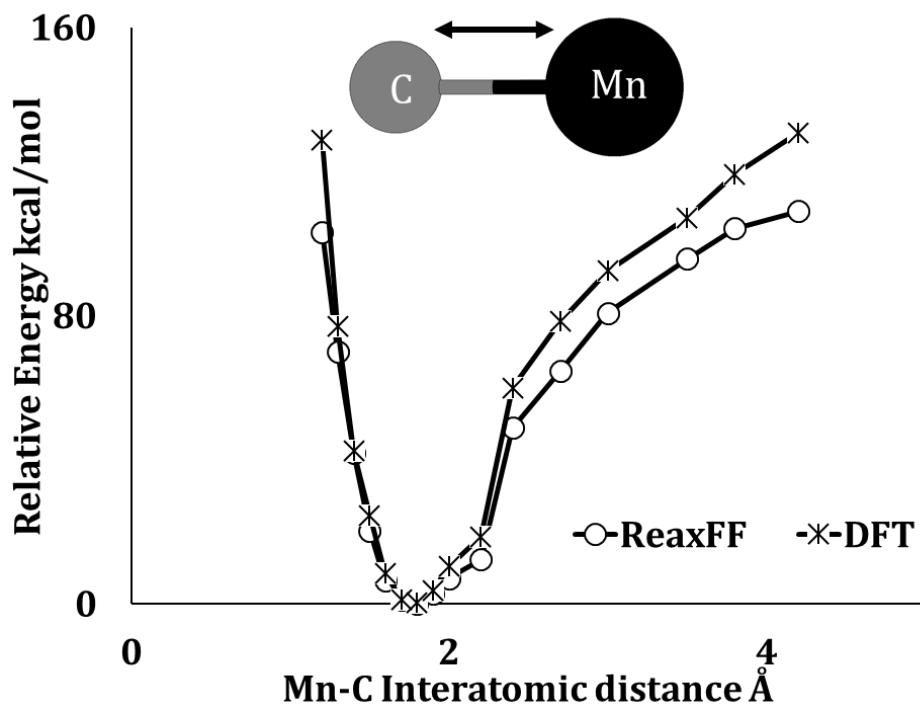
Figure 2.8 Mn-C bond stretching in MnC molecule. Relative energy is calculated with respect to the optimum geometry of MnC.

ReaxFF: 1.032
DFT: 1.116

ReaxFF: -0.516
DFT: -0.558

ReaxFF: -0.516
DFT: -0.558

Manganese (IV) oxide, MnO_2

ReaxFF: 0.916
DFT: 0.936

ReaxFF: 0.916
DFT: 0.936

ReaxFF: -0.746
DFT: -0.788

ReaxFF: -0.543
DFT: -0.542

ReaxFF: -0.543
DFT: -0.542

Manganese (III) oxide, Mn_2O_3

ReaxFF: 0.237
DFT: 0.255

ReaxFF: 0.885
DFT: 0.871

ReaxFF: 0.237
DFT: 0.255

ReaxFF: -0.679
DFT: -0.691

ReaxFF: -0.679
DFT: -0.691

Manganese hydroxide, $Mn(OH)_2$

ReaxFF: -0.584
DFT: -0.645

ReaxFF: 0.584
DFT: -0.558

Manganese (II) oxide, MnO

ReaxFF: -0.223
DFT: -0.240

ReaxFF: 0.223
DFT: 0.240

Manganese carbide, MnC

ReaxFF: -0.465
DFT: -0.573

ReaxFF: 0.767
DFT: 0.857

ReaxFF: 0.438
DFT: 0.674

ReaxFF: -0.465
DFT: -0.573

ReaxFF: -0.275
DFT: -0.385

Manganese carbonate, $MnCO_3$

ReaxFF: -0.524
DFT: -0.552

ReaxFF: 1.024
DFT: 0.842

ReaxFF: 0.153
DFT: 0.120

ReaxFF: -0.401
DFT: -0.304

ReaxFF: 0.478
DFT: 0.599

ReaxFF: -0.524
DFT: -0.552

ReaxFF: 0.153
DFT: 0.120

Manganese acetate, $Mn(COOCH_3)_2$

Figure 2.9 Charge distribution in manganese molecules as predicted by ReaxFF and DFT.

FLUORINE INTERACTIONS WITH MANGANESE AND LITHIUM

The condensed phase properties of manganese and fluorine containing compounds were obtained using lithium fluoride, manganese di-fluoride and manganese tri-fluoride. The deposition of lithium fluoride has been observed and the deposition of manganese fluorides has been widely speculated in the SEI layer. In order to predict the formation of these fluorides, the developed ReaxFF model accurately captures the energetics of formation and decomposition of these compounds. The ReaxFF model parameters are optimized against DFT obtained equations of state and heats of formation of the three condensed phases. Figure 2.10 shows the equation of state of MnF_2; ReaxFF is able to capture the energetics of density changes in the MnF_2 crystal well beyond the equilibrium structure. ReaxFF predicts the equilibrium density of MnF_2 to be 3.90 g/cc, which is within 2% error of the experimentally observed value of 3.98 g/cc[55]. Table 2.4 shows the heats of formation of the three condensed phases. The heats of formation as predicted by the ReaxFF model are in good agreement with DFT calculated as well as experimentally observed values.

Manganese and fluorine parameters were also fit to bond stretching and angle bending curves of manganese and lithium fluoride molecules. Table 2.5 compares the equilibrium bond length of molecules as predicted by the ReaxFF model, DFT and as observed experimentally.

Table 2.4 Heats of formation of fluorine containing condensed phases as predicted by ReaxFF and DFT compared with experimentally observed values. The heats of formation are calculated relative to the stable pure form of each species.

Heats of formation kcal/mol			
	ReaxFF	DFT	EXP.
LiF	148.2	147.9	146.3[56]
MnF_2	222.7	221.4	203.0[57]
MnF_3	262.2	258.8	256.0[57]
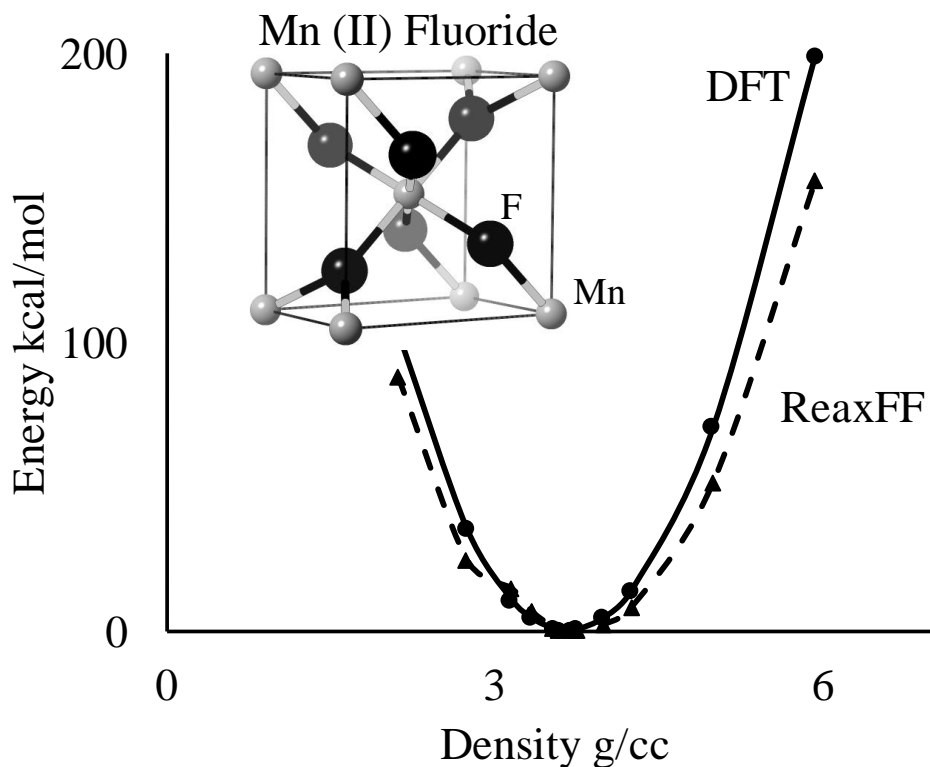
Figure 2.10 Equation of state of MnF_2 crystal as predicted by ReaxFF and DFT. ReaxFF is able to capture the energetics of density changes in the MnF_2 crystal well beyond the equilibrium structure.

Table 2.5 Equilibrium bond lengths of fluorine molecules in the training set as predicted by ReaxFF compared with DFT calculated and experimentally observed values.

Molecule	Bond type	Bond length $\mathring{A}$		
		ReaxFF	DFT	Exp.
MnF_2	Mn-F	1.81	1.81	1.74[58]
MnF_3	Mn-F	1.77	1.78	1.73[58]
LiF	Li-F	1.57	1.58	1.54[58]
F_2	F-F	1.45	1.44	1.42[59]
HF	H-F	0.97	0.95	0.92[60]
OF_2	O-F	1.45	1.45	1.41[61]
CH_3F	C-F	1.38	1.42	1.35[59]
CF_4	C-F	1.36	1.35	1.35[59]

FLUORINE INTERACTIONS WITH CARBON, HYDROGEN, AND OXYGEN

The ReaxFF model predictions of bond energy curves of C-F bond stretching in a CH_3F molecule and H-F bond stretching in a HF molecule are shown in Figure 2.11. ReaxFF is able to predict the energy changes associated with fluorine bond formation and dissociation in good agreement with DFT predicted trends. ReaxFF predicts a H-F bond (HF molecule) dissociation energy of 125 kcal/mol in close agreement with the experimental value of 135 kcal/mol[52] and C-F bond dissociation energy (in CH_3F) of 103 kcal/mol as compared the experimental value of 108 kcal/mol[52]. Table 2.5 compares the ReaxFF predicted equilibrium bond distances with DFT calculated values as well as experimentally observed values; ReaxFF predicts bond distances within 2% error. Further, as shown in Figure 2.12, ReaxFF is also successful in reproducing DFT calculated charge distribution in fluoroethylene carbonate molecule.
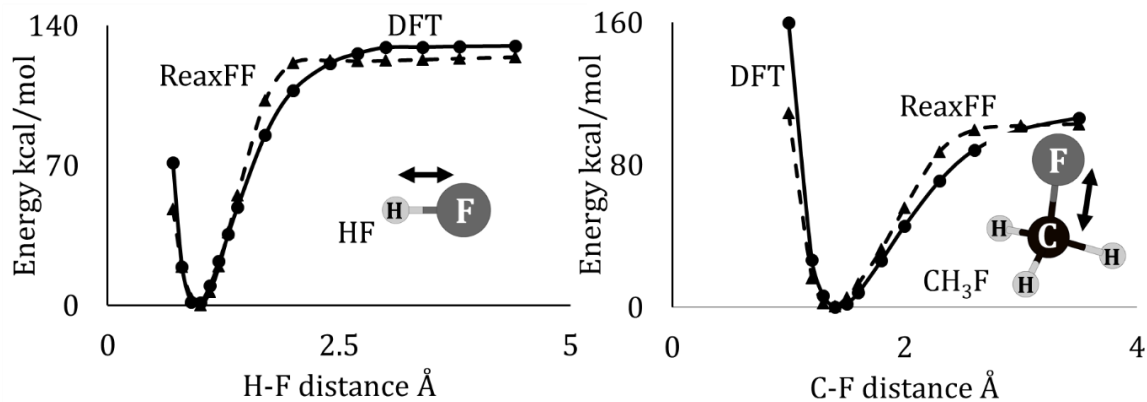
Figure 2.11 Bond energy curves for H-F bond stretching in a HF molecule and C-F bond stretching in a CH₃F molecule. ReaxFF predicts the dissociation energies of both bonds within 3% error of the DFT predicted values.
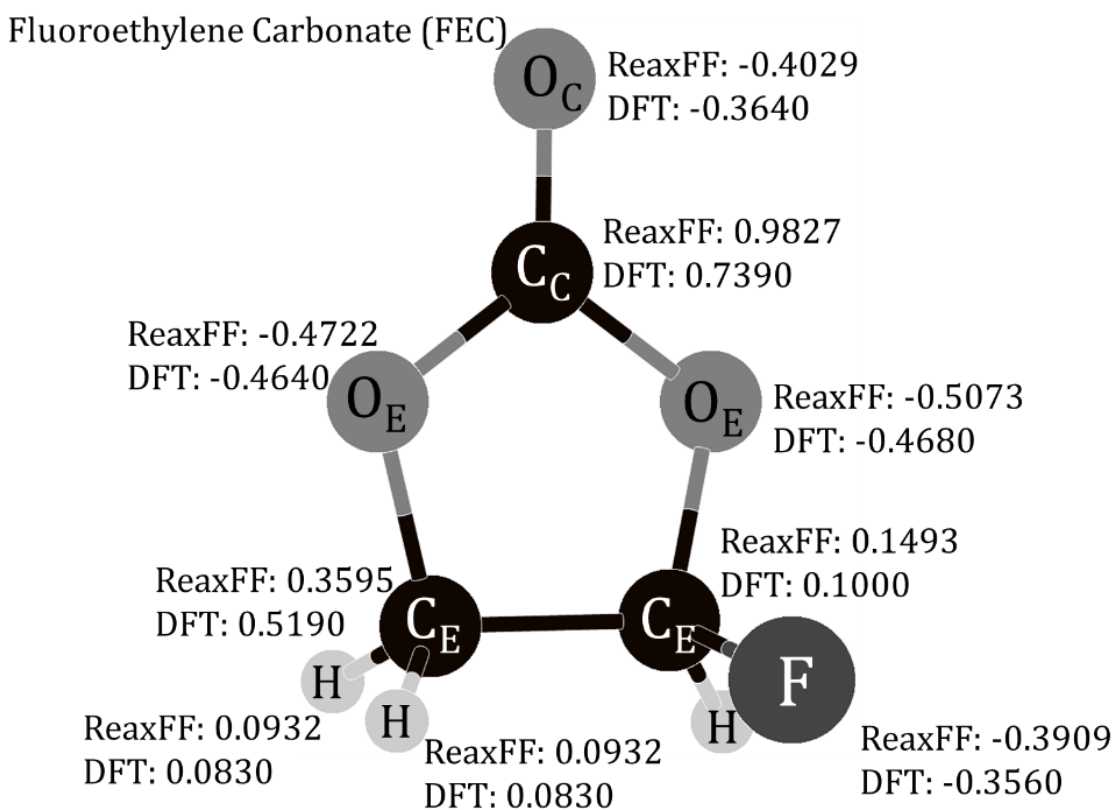
Figure 2.12 Charge distribution in a fluoroethylene carbonate molecule as predicted by ReaxFF and DFT.

MANGANESE INTERACTIONS WITH LITHIUM

The ReaxFF model parameters for manganese lithium interactions with optimized to reproduce the energetics of the $LiMn_2O_4$ spinel structure. The equation of state predictions of the spinel structure (shown in Figure 2.13) reveal that ReaxFF is able to capture the lattice energetics of the fully lithiated spinel. ReaxFF reproduces the optimum lattice constant of the spinel within 2% of the DFT predicted value and is able to predicted the heat of formation with respect to the most stable phases of which element with good accuracy.
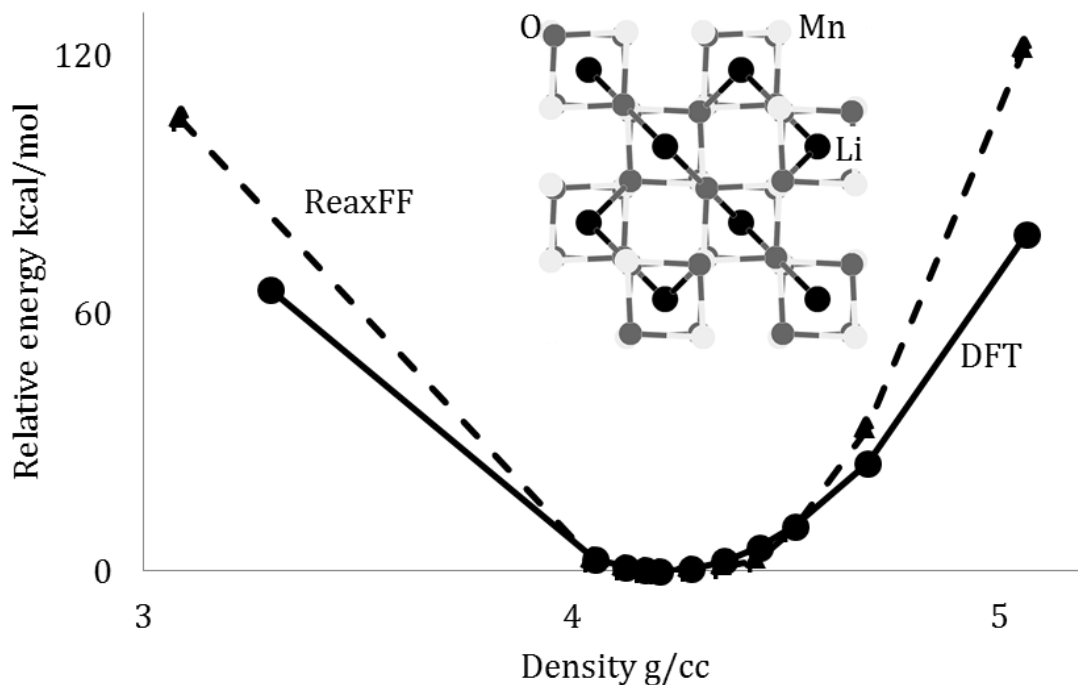
Figure 2.13 Equation of state for $LiMn_2O_4$ spinel structure. The energy is reported relative to the optimum structure.

The ReaxFF model was also validated against the heat of formation of the spinel structure with different lithium loadings. As shown in Figure 2.14, ReaxFF is able to reproduce the

heats of formation of spinel structures with high lithium loading but is unable to capture the energetics of lower charge spinel structures. The scope of this study is limited to lithium loadings of x=1, but the use of this force field to simulate $LiMn_2O_4$ cathode charge and discharge requires further improvement in the ReaxFF model. Figure 2.15 shows the ReaxFF predictions of the surface energies of the spinel structure. The energies of three surfaces (001, 110, 111) with different terminating atom layers (lithium (L), manganese (M), oxygen (O)) are compared to the energy of bulk spinel. Surface energies are calculated for structures with lithium loading of x=1. ReaxFF is able to capture surface energy of 001 with a high degree of accuracy but needs to be improved for other the two surfaces.
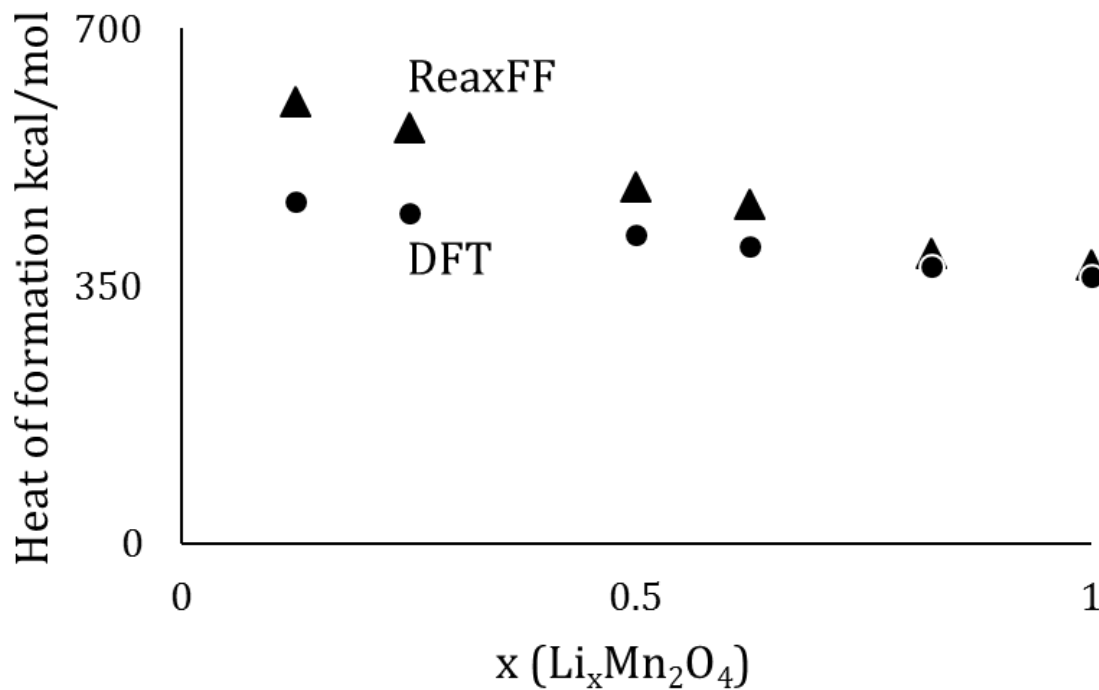
Figure 2.14 Heat of formation as predicted by ReaxFF and DFT for various lithium loadings.
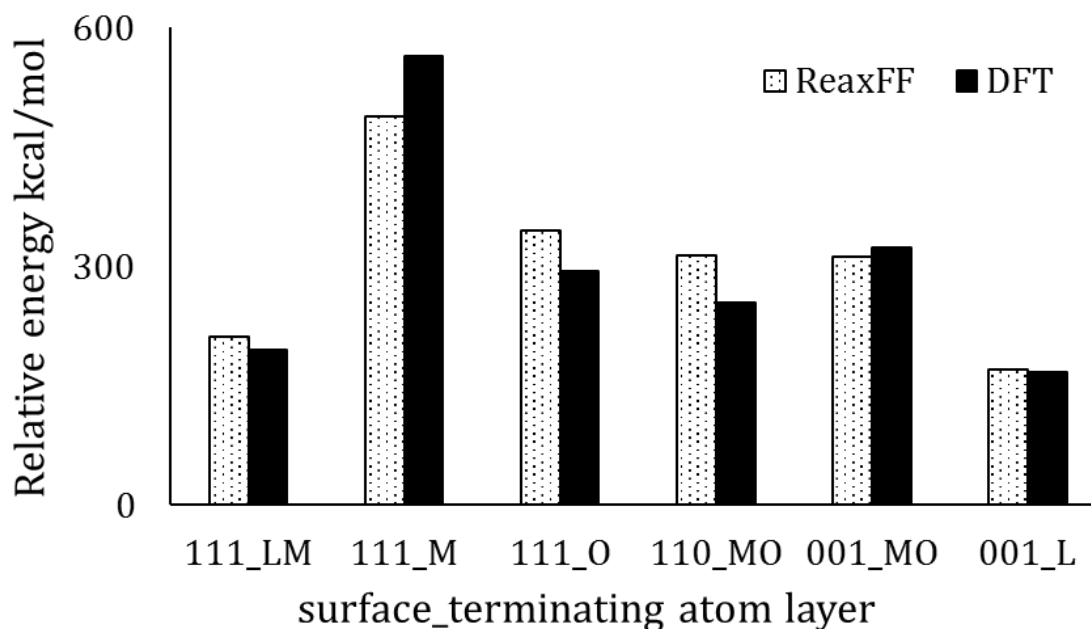
Figure 2.15 ReaxFF and DFT predicted energies of spinel surfaces and terminations. The horizontal axis is labelled starting with the surface followed by the terminating atom layer denoted as L (lithium), M (manganese), O (oxygen). The energy is reported relative to bulk spinel.

2.4 REAXFF BASED MOLECULAR DYNAMICS ANALYSIS OF MANGANESE DIOXIDE REDUCTION BY METHANE GAS

The newly developed ReaxFF model for manganese containing systems has been validated against DFT derived energetics with a high degree of accuracy. Before the model is used to study complex electrochemical systems, it is useful to test the ability of the force field to reproduce experimental observations in a molecular dynamics simulation. The ReaxFF model is used to study the reduction of manganese oxides by methane at high temperatures.

2.4.1 EMERGING CATALYSTS

Manganese oxides are well-known for their activity in oxidation reactions and have been used since ancient times to clarify glass by oxidizing iron impurities[62]. Since

41

then manganese oxides have found a wide variety of applications like in oxidation of organic pollutants[63–65], as catalysts for oxidative hydrocarbon coupling[66,67], and as battery cathodic materials[68]. Manganese oxides are further being studied as potential candidates for three-way catalyst catalytic convertors[69], catalysts for photocatalytic oxidation of water[70], and also as oxygen storage compounds for chemical looping combustion[71,72]. The catalytic properties of manganese oxides are attributed to the ease by which manganese cations undergo changes in oxidation states[73]. Manganese exists naturally in three different oxidation states (Mn^{4+}, Mn^{3+}, Mn^{2+}) allowing for a wide range of manganese oxide stoichiometry. Additionally, manganese is able to form multivalent oxides, increasing the diversity of atomic structures and hence increased oxidation activity.

Manganese oxides are attracting considerable attention from both academia and industry due to its low cost and low environmental toxicity in contrast to the currently used commercial oxidation catalysts that contain expensive noble metals like Pt, Rh, and Pd[74,75]. Also more recently, manganese oxides are being considered as potential oxygen storage compounds for chemical looping combustion because of their ability to be reduced by giving up lattice oxygen and be easily oxidized by air. Chemical-looping combustion (CLC) is an advanced combustion technology that uses a metal oxide as an oxygen carrier to transfer oxygen from the combustion air to the fuel, allowing for the reduction in the operation cost of the combustion reaction by using air instead of pure oxygen and also enabling the production of carbon dioxide that is free of nitrogen and sulfur impurities aiding in efficient CO_2 capture[76].

A high activity for complete oxidation of methane was discovered in manganese oxides as early as 1964[77]. But the instability of pure manganese oxides at high temperatures[78] and reduced reactivity due to low porosity[79] greatly limited its adoption as an oxygen carrier for CLC. The interest in manganese oxides as has been rekindled after a number of studies that show enhanced methane oxidation on doping commercial oxygen storage compounds (OSC) with manganese[80,81,82]. Further, there has also been progress on developing support materials that overcome the decomposition and porosity limitations of manganese oxides. A comparison of activities of different oxygen carries and support materials (over 240 combinations) showed that Zr[83] based supports are the best for preparing manganese oxide carriers while Al_2O_3 based supports show poor reactivity due to the formation of $MnAl_2O_4$ on successive cycles of reduction and oxidation[84]. Another study used $LaAlO_2$ support for manganese oxides and reported a higher oxygen storage capacity, and faster oxygen absorption and oxide reduction rates than the present commercial ceria-stabilized alumina support materials; this increased activity has been attributed to the higher Mn oxidation state in $LaAlO_2$ supports[69].

There has been a lot of work done to study the commercial viability of manganese oxides as OSCs but nearly not enough work to study the reaction mechanisms behind valuable redox properties of manganese oxides. With potential growing use of manganese oxides as catalysts, artificial photosynthesis[68], cathode materials for microbial fuel cells[85], it is important to understand the reaction mechanisms that contribute to the catalytic activity of manganese oxides. Insights into these reaction mechanisms will be useful in guiding the invention of feasible manganese oxide based catalysts and oxidation storage compounds.

In order to study the oxidizing properties of manganese oxides at the molecular level, we need computational methods that are able to capture properties of manganese oxides at various Mn oxidation states and the ability of manganese to be easily reduced and oxidized within the crystal structures. As mentioned earlier, there has been little to no previous work done to reveal reaction mechanisms responsible for manganese oxide activity. Density Functional Theory (DFT) has been used to study the Mn-O bond character[86] in manganese oxides, determine active sites on manganese oxides[87] and to identify reaction transition states[88] but there no effort to study the activity of manganese oxides at a time and length scale that can reveal chemical reactions that occur on the catalytic surfaces of manganese oxides. In fact, there are no validated force fields that can successfully predict the redox properties of manganese oxides.

Therefore, this study aims to validate a reactive force field that is able to simulate changes in manganese oxidation states and predict the experimentally observed oxidation activity of manganese oxides. This work will further validate the developed ReaxFF model by simulating manganese oxide reduction by methane gas (CLC fuel reactor system).

2.4.2 MOLECULAR DYNAMICS METHODS

The optimized and validated ReaxFF model is applied to investigate high temperature manganese oxide reduction by methane. Three manganese oxides (MnO_2, Mn_2O_3, and Mn_3O_4) are considered to evaluate the ability of the ReaxFF model to predict the effects of manganese cation oxidation state on redox activity of the oxides. A crystal slab measuring 35 Å x 35 Å x 35 Å of each oxide is exposed on both surfaces to a total of 48 molecules of methane gas in a volume of 43000 $Å^3$. Periodic boundary conditions are

maintained in all three directions. The simulation cells are subjected to temperatures ranging from 500 K to 1500 K. Each MD simulation was initiated from an energy-minimized structure and was equilibrated to the simulation temperature for 100 ps prior to the production run for 1 ns with 0.25 fs time step.

The simulations were temperature programmed under the NVT ensemble using the Nosé Hoover thermostat with a temperature damping constant of 10 fs. NVT simulations at 1500 K were performed on a system consisting of only manganese oxide crystals to ensure that the crystals do not give up lattice oxygen spontaneously under the simulation conditions. Three unique simulations with each of the three manganese oxides under study (β-MnO_2, α-Mn_2O_3 and α-Mn_3O_4) were performed with the same crystal size and surfaces as in the simulation setup with the gas phase. No expulsion of lattice oxygen was observed without reaction with methane for all the oxides under study. A similar setup with only methane molecules ensured no decomposition of methane. The most stable phase for each oxide were chosen for the simulations.

The ReaxFF based MD simulations were implemented using the LAMMPS parallel molecular dynamics code[89]. Molecular analysis of the simulations, to identify reaction intermediates, was performed using a bond order cutoff of 0.2 as successfully used in previous work[36].

While the ReaxFF parameters for manganese interactions were developed in this work, previously developed parameters for oxygen, hydrogen and carbon were used[37] to describe the interactions between oxygen, hydrogen and carbon in the MD simulations.

2.4.3 RESULTS

METHANE OXIDATION REACTION PATHWAY

ReaxFF accurately predicts experimentally observed products of methane oxidation. Figure 2.16 shows the initial configuration and simulation snapshot after 300 ps with β-MnO_2. Further, ReaxFF reveals the methane oxidation intermediates. The time evolution of reactants and products over 1 ns is shown in Figure 2.17. ReaxFF predicts HCHO as a stable intermediate in the conversion of CH_4 to CO_2.

The complete oxidation of methane occurs by taking up lattice oxygen from manganese oxides as predicted by ReaxFF has been confirmed experimentally [90–95]. Figure 2.18 shows the reaction mechanism for high temperature CH_4 oxidation by manganese oxides as predicted by ReaxFF. The reaction proceeds through the abstraction of one hydrogen from methane by a surface lattice oxygen leading to the formation of a surface hydroxyl group and a methyl species. The methyl species reacts with a surface oxygen to form an adsorbed meth-oxy species or it reacts with a surface hydroxyl group to form gas phase CH_3OH. CH_3OH remains in the gas phase (80 ps) until it is re-adsorbed as a meth-oxy species by losing the hydroxyl hydrogen to a surface oxygen. The second hydrogen is abstracted to form HCHO. HCHO remains in the gas phase for more than 100 ps until it is able to remove the second oxygen from the lattice to form HCOOH. HCOOH loses the hydroxyl hydrogen quickly to a surface oxygen forming HCOO species. Experiments have observed HCOO species as an intermediate in formaldehyde oxidation by manganese oxides[96]. The HCOO species loses its H to form CO_2. When two surface hydroxyl atoms come into close proximity, a water molecule

desorbs from the surface. A similar mechanism has been proposed for methane oxidation with noble metals and Al_2O_3 supports[97].
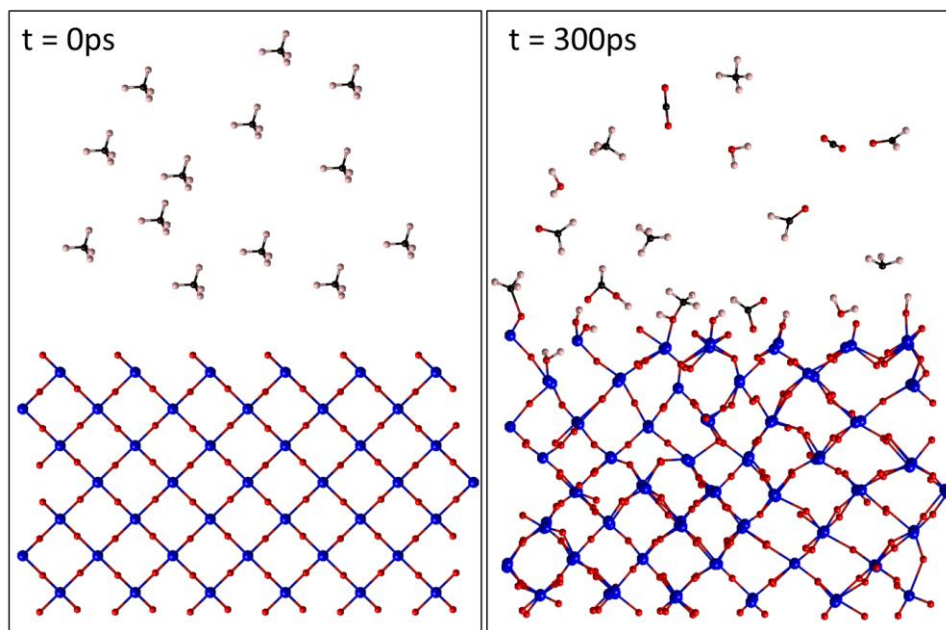
Figure 2.16 Simulation cell with β-MnO$_2$ and methane molecules at 0 ps and after 300 ps at 1000 K.
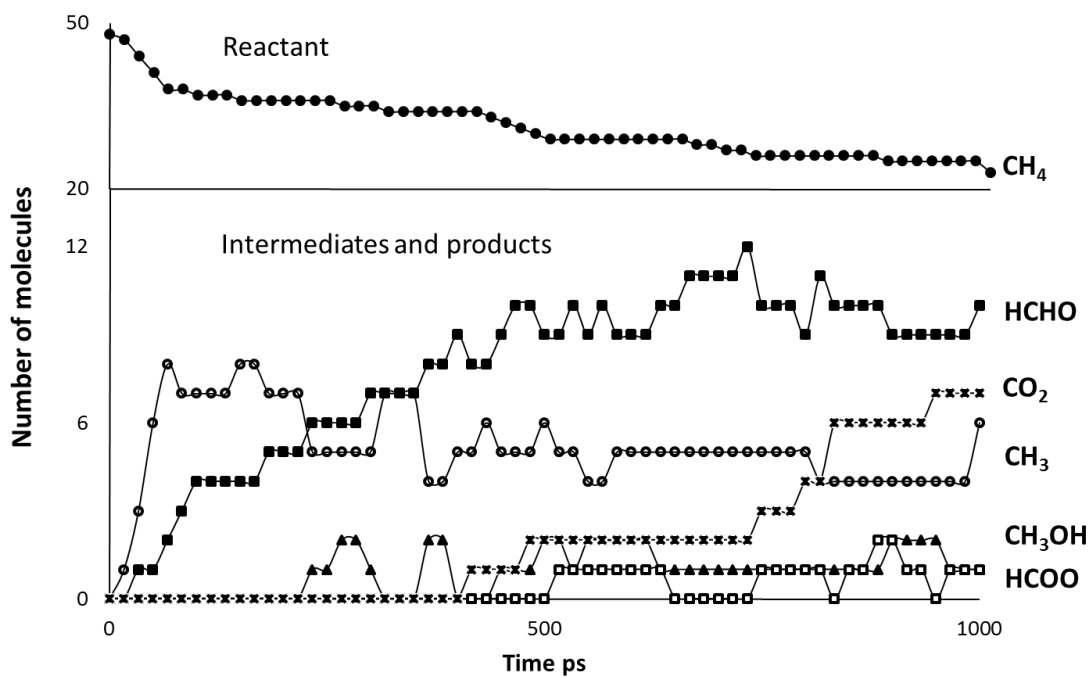
Figure 2.17 Time evolution of reactants and products over 1 ns when β-MnO$_2$ surface is exposed to methane at 1000 K.
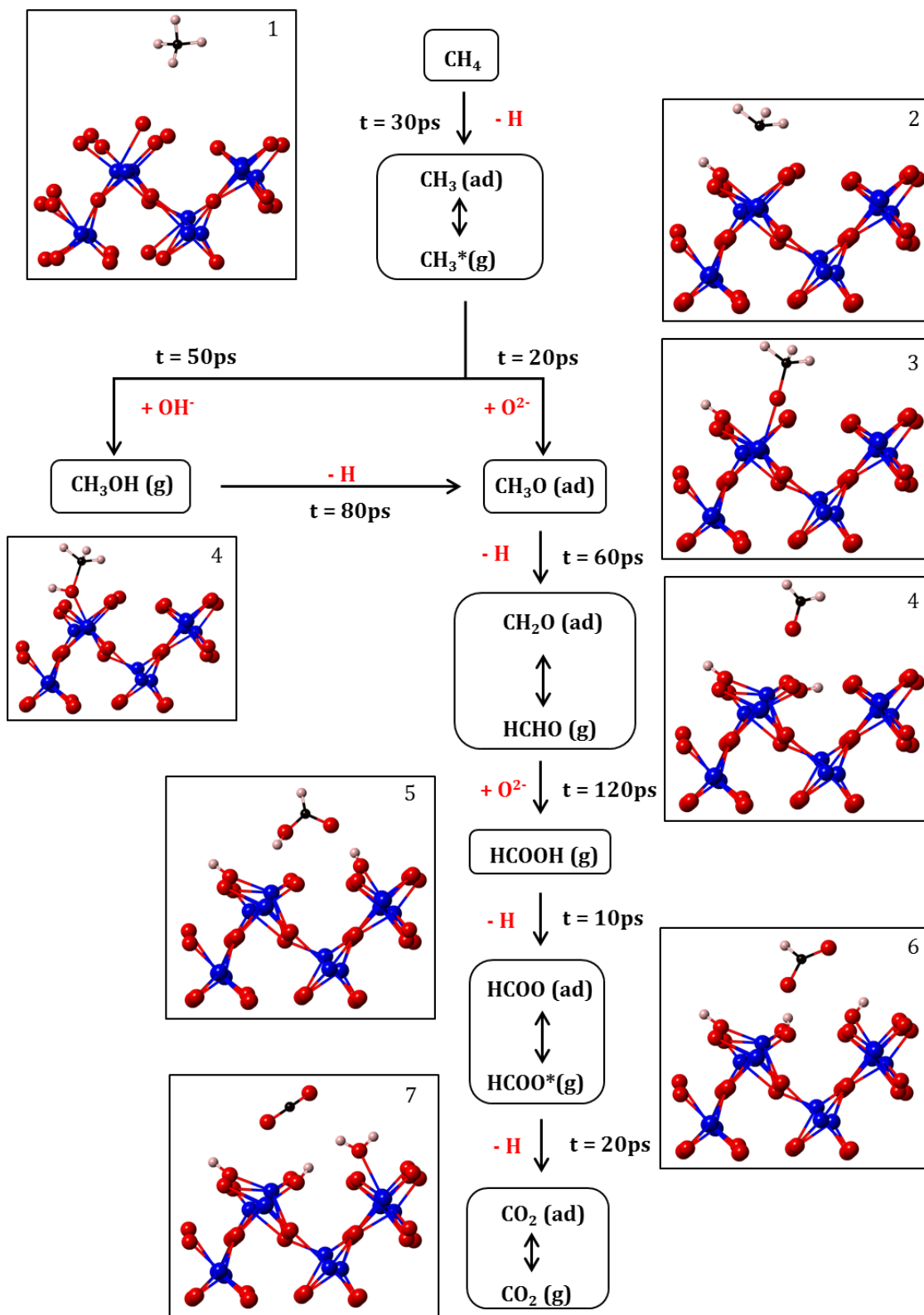
Figure 2.18 Reaction mechanism for the oxidation of methane on β-MnO₂ surface.

MANGANESE OXIDATION STATE ACTIVITY TOWARDS METHANE OXIDATION

Further, the ability of the developed ReaxFF model to predict the differences in oxidation activity of different manganese oxides was evaluated. Activity was determined as the ease of manganese oxidation reduction by methane. ReaxFF was used to simulated methane oxidation on three manganese oxides, β-MnO_2, α-Mn_2O_3, and α-Mn_3O_4 with manganese oxidation states of Mn^{4+}, Mn^{3+} and mixed Mn^{3+}, Mn^{2+}, respectively. Figure 2.19 shows the temperature dependence of methane conversion of the three oxides, CH_4 conversion by manganese oxides decreases in order of β-MnO_2 > α-Mn_2O_3 > α-Mn_3O_4. Experiments have revealed that Mn^{4+} has higher catalytic activity[98] as compared to Mn^{3+} and Mn^{2+}.
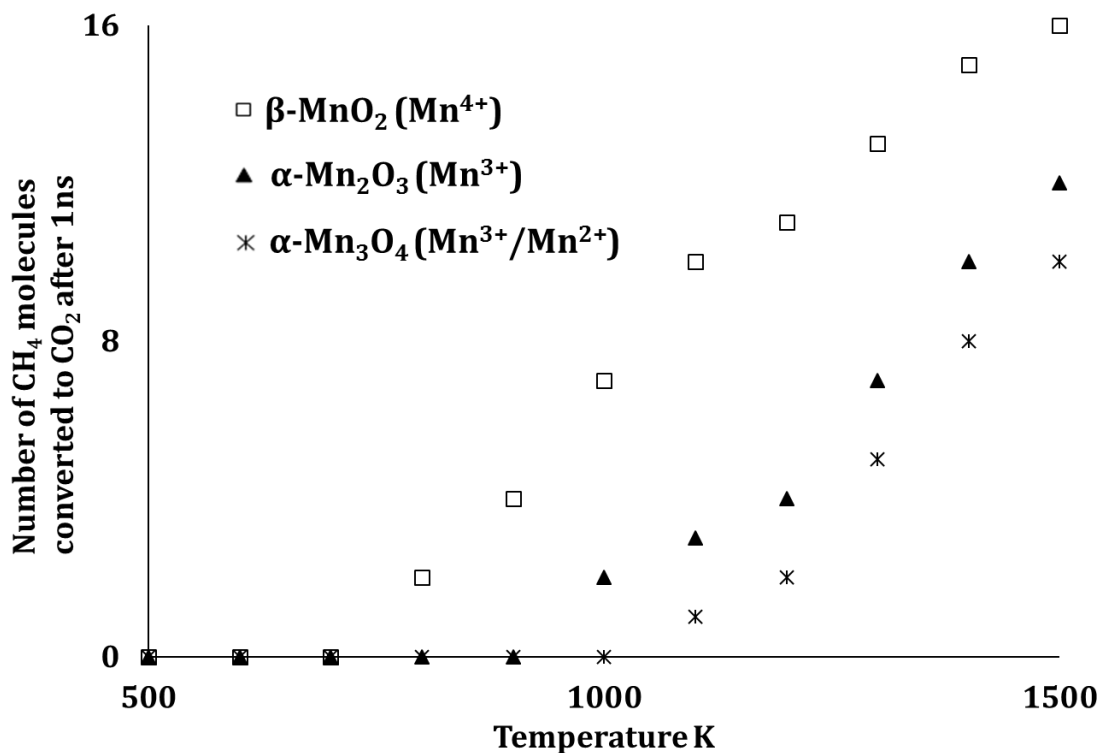
Figure 2.19 Temperature dependency of methane reduction of the three manganese oxides.

2.5 CONCLUSIONS

The ReaxFF model was optimized to describe systems comprising the elements Mn, O, C, H, Li, and F. The ReaxFF model reproduced the DFT derived energetics of compounds representative of the interactions occurring in a $LiMn_2O_4$ based electrochemical cell. The ReaxFF model was trained against equations of state, heats of formation, bond stretching energies, angle bending energies, reaction enthalpies and charge distributions. The lattice parameter for the stable metallic manganese phase was predicted within 3% error of the experimental value by the ReaxFF model. The model accurately captures the reaction enthalpies of manganese oxides with 3% error of DFT predicted values, demonstrating the ability of the ReaxFF model to capture the energetics of manganese oxidation states changes. The ReaxFF model is also able to capture the energetics of lattice expansion and contraction of the $LiMn_2O_4$ crystal as well as the energy associated with a 100 surface of the crystal. The optimized force field has predicted the properties of the training set compounds in good agreement with DFT predicted and experimentally observed values.

The force field was further validated by simulating high temperature methane oxidation over manganese oxide surfaces. The force field predicts complete oxidation of methane to CO_2 and H_2O by taking up lattice oxygen atoms into the gas phase, as observed by experiments. ReaxFF also predicts Mn^{4+} oxide (MnO_2) to be more reactive towards methane oxidation than Mn^{3+} or Mn^{2+} oxides, in agreement with experiments. ReaxFF reveals that formaldehyde is the major intermediate in the methane oxidation reaction. The developed model was successfully used to run molecular dynamics simulations to establish reaction mechanisms and reaction intermediates in systems

containing manganese, carbon, hydrogen and oxygen. The validated model will now be used to study the LiMn$_2$O$_4$ cathode based Li-ion electrochemical cell.

CHAPTER 3

EFFECTS OF FLUOROETHYLENE CARBONATE AND DISSOLVED MANGANESE IONS ON THE ANODE SEI LAYER USING REAXFF BASED MOLECULAR DYNAMICS

3.1 INTRODUCTION

Lithium ion batteries have great potential to revolutionize the transportation sector as energy storage media for electric mobility. Among the various lithium ion battery chemistries that have been proposed, manganese based cathode active materials are presently exploited for automotive applications, on account of low cost, low toxicity, and simple preparation process as compared to other cathode chemistries[99,100,51]. Lithium ion batteries undergo a number of degradation mechanisms through side reactions that consume cyclable lithium ions leading to capacity and power loss[1]. During the initial charge cycle, the electrolyte solvents are reduced on the surface of the anode, resulting in the formation of various surface species which constitute the solid-electrolyte interface (SEI) layer. Lithium ions are consumed in the process, leading to the formation of inorganic and organic lithium salts[101]. The SEI layer is able to conduct Li-ions but not electrons, preventing further decomposition of the electrolyte and hence improving the cycle life of Li-ion batteries. Thus formation of a passivating and stable SEI layer is integral to the electrochemical process in lithium ion batteries[102].

One successful strategy to obtain a stable SEI layer is using organic electrolyte additives like fluoroethylene carbonate (FEC)[101]. FEC has a slightly higher reduction potential than the other electrolyte solvents and is able to decompose before other electrolyte solvents, resulting in a uniform and stable SEI layer[103]. Scanning Electron Microscopy (SEM) and Electrochemical Impedance Spectroscopy (EIS) measurements reveal that the SEI layer formed in the presence of FEC are thinner[104], have lower ionic resistance[105] and are more stable at high temperatures[106] as compared to an SEI formed in the absence of FEC. However, the speciation of FEC on the surface of anodes has not yet been well understood. Fourier Transform Infrared Spectroscopy (FTIR) analysis of silicon anodes revealed a high concentration of LiF in the SEI layer, which is proposed to have originated from the dehydrofluorination of FEC to form LiF and vinylene carbonate (VC)[104]. Ab initio molecular dynamics simulations on silicon anodes proposed that one- and two-electron reactions led to the release of F^- anion to form LiF[107]. One other study on lithium anodes speculated that the apparent absence of C-F bonds in the SEI indicates that volatile fluorine-containing hydrocarbon components like C_2H_3F may be removed as gaseous products before they can form SEI films[108]. Yet another study proposed the formation of polymeric fluoro- and vinylene- carbonates as constituents of the stable SEI layer[109]. In spite of extensive evidence of the ability of FEC to form a robust SEI layer on graphite anodes, there has been little to no effort to elucidate the reaction mechanisms of FEC on the surface of graphite anodes. Insights into the mechanisms of the formation of a stable SEI layer by FEC will help determine dosage electrolyte additives as well as guide the development of novel electrolyte additives.

Apart from developing a stable SEI layer during the initial formation cycles, maintaining the integrity of the layer through multiple charge and discharge cycles is critical to the life of the battery. The predominant battery ageing mechanism especially for manganese based lithium ion cells is the dissolution of cathode material[110]. The dissolution of divalent manganese into the electrolyte has a twofold effect on the overall cell capacity: (i) it decreases the effective amount of active cathode material available for lithium intercalation, and (ii) it decreases the lithium content of the anode by oxidizing lithium ions from the anode as dissolved manganese ions deposit in the SEI layer[11]. The deterioration of the SEI layer in the presence of manganese ions was revealed through SEM and electron probe micro analyzer (EPMA) analyses[111]. However, the manganese induced SEI degradation mechanisms and speciation of manganese in the SEI layer are highly debated because experimental techniques are not yet able to accurately detect the extremely low concentration of manganese in the SEI layer. Some studies have reported that manganese ions are reduced to metallic manganese on the surface of the anode[112,113] while other studies have disputed this theory to report that manganese is deposited on the anode in the 2^+ oxidation state[114]. Further, there is no conclusive evidence on the type of manganese compounds found in the SEI layer; $MnCO_3$[115], MnF_2[116], MnO[111] are some of the commonly reported species. It is essential to understand the effects of manganese ions on the SEI layer in order to develop strategies to increase battery life.

This work aims to reveal (i) the speciation of FEC that results in the formation of a stable SEI layer and (ii) the compositional changes that lead to SEI degradation in the presence of Mn ions. The extremely fast reaction dynamics and low *in situ* concentrations of both these phenomena make them inaccessible to study using experimental techniques.

Computational methods like molecular dynamics (MD) are more suitable to reveal these nanoscale molecular reactions.

3.2 MOLECULAR DYNAMICS METHODS FOR THE ANODE HALF-CELL

The anode half-cell of a $LiMn_2O_4$ based battery is simulated using ReaxFF based molecular dynamics. A lithiated graphite anode is exposed to and electrolyte consisting of 3:7 mole ratio[117] of ethylene carbonate (EC) and dimethyl carbonate (DMC) as the electrolyte solvents, 1 M lithium hexafluorophosphate as the electrolyte salt, and 5% fluoroethylene carbonate as the electrolyte additive. The electrolyte molecules react with Li atoms from the anode, resulting in the formation of compounds that comprise the SEI layer on the surface of the anode.

Figure 3.1 shows the simulation cell that measures about 15 nm x 3.5 nm x 3.5 nm. The graphite slab with dimension 7 nm x 3.5 nm x 3.5 nm is located in the middle of the simulation cell and the rest of the simulation cell is filled with 208 EC molecules, 480 DMC molecules, 40 FEC molecules and 60 $LiPF_6$ molecules, which results in an equilibrium electrolyte density of 1.26 g/cc. This configuration helps with maintaining periodic boundary conditions in all three directions without any discontinuities. Bulk electrolyte character is maintained at distances greater than 3 nm from the anode surfaces even after 2 ns, the maximum time period in this study.
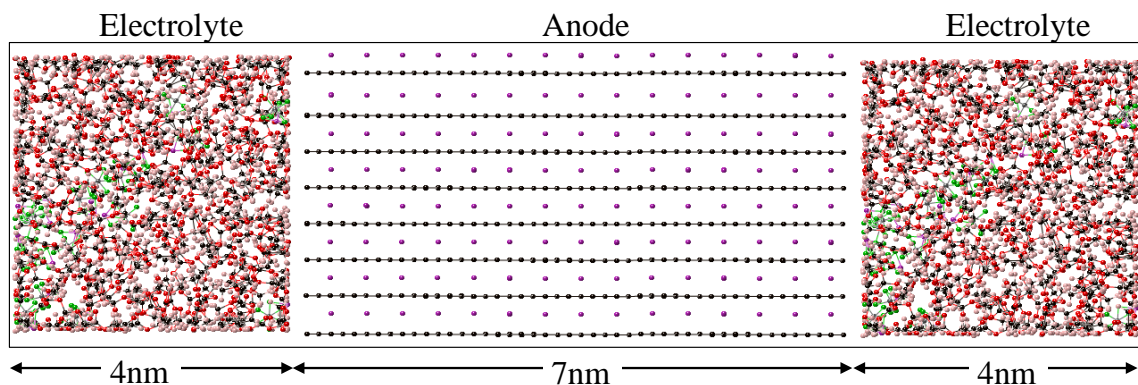
Figure 3.1 The starting configuration of the simulation cell with the anode in the center exposed to the electrolyte on both surfaces. The simulation box plane into the paper measures 3.5 nm x 3.5 nm. Lithiated graphite is used as the anode, 3:7 mol/mol mixture of EC and DMC as the electrolyte, 1M $LiPF_6$ as the salt and 5% FEC as the electrolyte additive.

The simulation cells were maintained at 303 K under the NVT ensemble using the Nosé Hoover thermostat with a temperature rescaling constant of 10 fs. The starting configuration of the electrolyte molecules was generated using the PACKMOL[118] code to make sure short range repulsive forces do not disrupt the simulation. Each MD simulation was initiated from an energy-minimized structure and was equilibrated to the simulation temperature for 100 ps prior to the production run for 1 ns with a 0.2 fs time step.

In order to study the effect of manganese on the SEI compounds, an SEI layer was developed on the surface of the anode by running a second set of simulations with the above described configuration for 700 ps. Manganese atoms were then introduced at random locations within a distance of 10 Å from the surface of the anode. This method has been successfully used by previous work to overcome the inability of empirical force field MD methods to explicitly mimic electron transfer from the anode to the electrolyte[119]. The introduction of manganese atoms assumes that the electron transfer has already taken place and enables the study of manganese speciation after taking up

electrons from the anode. Manganese atoms are introduced into the SEI layer at a rate of 0.5 atoms/ps with a total of 12 atoms introduced into the simulation cell. After the introduction of manganese atoms, the simulations were run for an additional 300 ps. This study also developed the force field to include manganese hexafluorophosphate salt in the simulation in order to study the solvation of manganese in the electrolyte, but the low dissociation constant of the salt resulted in irreproducible results in the given timescales.

The ReaxFF based MD simulations were implemented using the LAMMPS parallel molecular dynamics code[89]. Molecular analysis of the simulations, to identify SEI layer compounds, were performed using a bond order cutoff of 0.2[36] as implemented in a home built MATLAB code.

3.3 RESULTS

3.3.1   FATE OF FEC IN THE SEI LAYER

The developed and validated ReaxFF model is applied to study the fate of FEC in the SEI layer on a graphite anode. An anode half-cell simulation is conducted as described in section 3.2, and the simulation results are analyzed to identify the SEI layer composition in the presence of FEC and the decomposition reaction of FEC on the surface of the anode.

The SEI layer compounds after 1 ns of simulation are summarized in Table 3.1. The SEI layer compounds formed in the simulation are in good agreement with previous studies[120]. Figure 3.2 shows the precursor electrolyte solvent compounds of the most commonly found lithium salts in the SEI layer. The cyclic electrolyte solvent molecules (EC and FEC) decompose into the inorganic lithium salt Li_2CO_3 and into gaseous species

C_2H_4 in the case of EC and CH_2CHF in the case of FEC. ReaxFF predicts the presence of Li_2CO_3 as the only inorganic lithium salt formed on the surface of graphite. DMC decomposes to yield organic lithium salts and gaseous carbon monoxide.

Table 3.1 SEI layer compounds on a graphite anode with EC/DMC based electrolyte, $LiPF_6$ salt and FEC additive as predicted by ReaxFF based MD simulations.

Inorganic compounds	Organic compounds	Gases
Li_2CO_3	$LiOCO_2CH_3$	CO
	$LiCH_3$	C_2H_4
	$LiOCH_3$	C_2H_3F
	$LiOCO_2C_2H_4$	
	$(CH_2OCO_2Li)_2$	
	$(OCO_2C_2H_4)_n$ n=2-5	
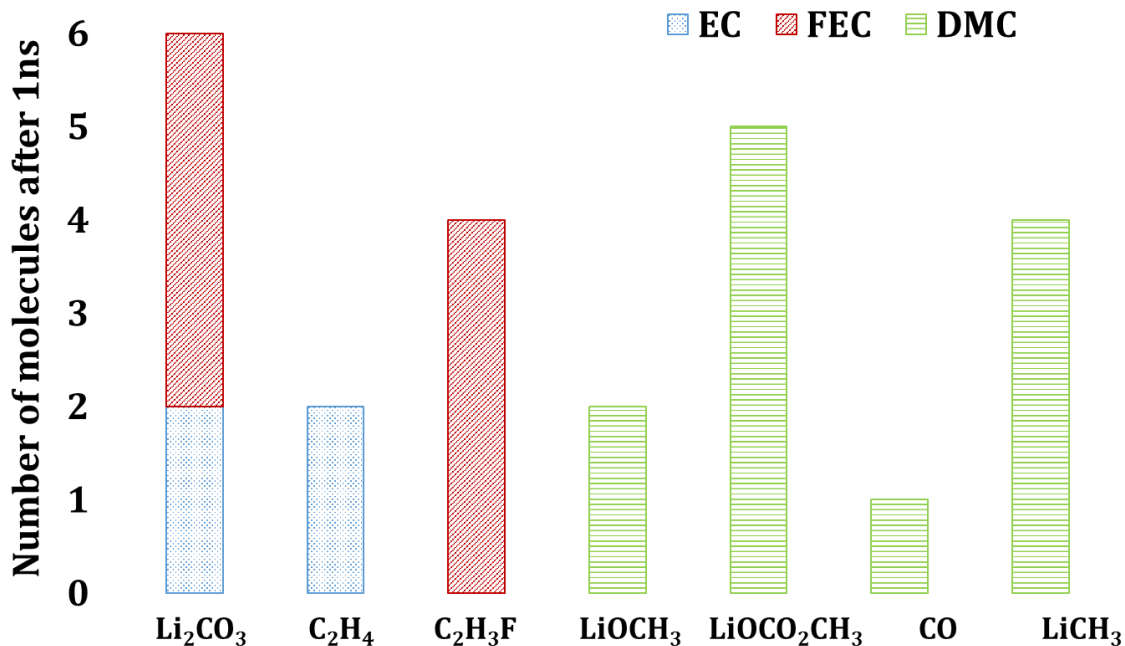
Figure 3.2 The most common lithium salts in the SEI layer based on ReaxFF MD. The precursor electrolyte compounds of each salt are also depicted.

While the decomposition pathway of EC to Li_2CO_3 has been confirmed through DFT calculations[121] as well *ab initio* molecular dynamics[119,122], the decomposition of FEC to Li_2CO_3 has been speculated but also widely debated. Figure 3.3 shows simulation snapshots of the decomposition pathway of FEC to Li_2CO_3 and CH_2CHF. This is the only pathway of FEC decomposition observed in the simulation cell. Schroder et. al discuss the two possible pathways of FEC decomposition on Si anodes, one that results in Li_2CO_3 and C_2H_4 as products (as observed by this work) and the other pathway that results in the formation of lithium fluoride, lithium ethoxide and methylene dioxide ion[123]. Although an increased amount of LiF in the SEI layer on Si anodes in the presence of FEC has been confirmed by Nie *et al.*[124], the source of LiF has not been identified, leaving the decomposition products of FEC open to debate. The results of this study provide evidence of FEC decomposition via the first pathway suggested by Schroder *et al*.
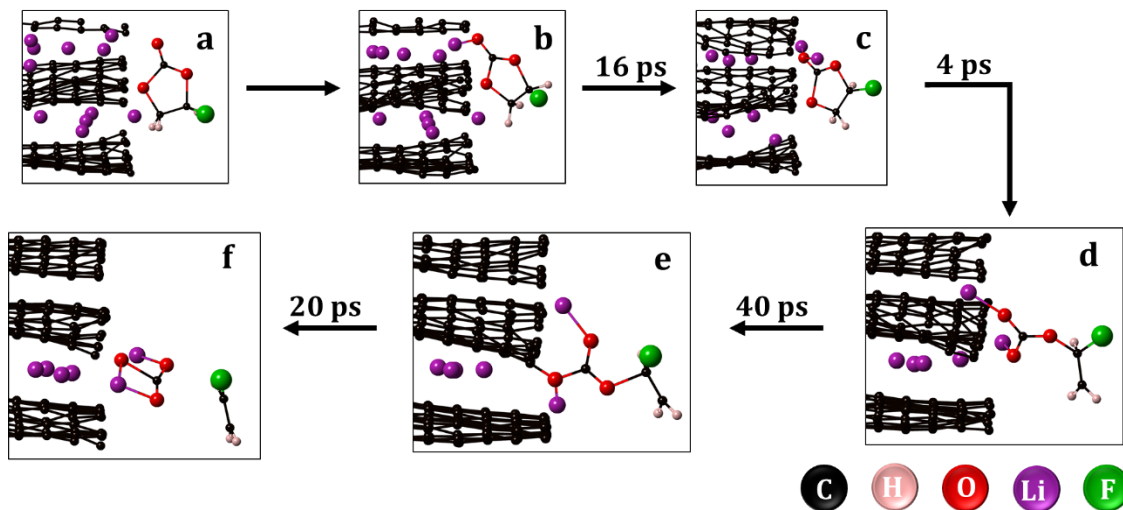
Figure 3.3 FEC decomposition reaction pathway on graphite anodes.

The one electron reduction product of FEC (panel d of Figure 3.3) with the C_E-O_E bond cleavage (see Figure 2.12 for atom labels) has been found to be a stable

intermediate of FEC decomposition by Mogi et al.[108]. Moreover, Mogi et al. concluded that $Li^+ {}^-OCO_2$ is the most likely product of FEC decomposition as they did not find any compounds directly derived from FEC, as predicted by simulations in this study. Further, DFT studies on FEC decomposition on Si clusters[125] found that C_E-O_E bond cleavage on the anode surface is thermodynamically feasible and the two electron transfer reaction with both C_E-O_E bonds dissociating has the lowest reaction energy but a very high energy barrier on Si clusters. ReaxFF predicts FEC decomposition via C_E-O_E bonds dissociating to form Li_2CO_3 and CH_2CHF likely due to a lower energy barrier on graphite anodes. Time-of-flight secondary ion mass spectrometry studies conducted by Nakai et al.[126] reveals the presence of polyene compounds in FEC based SEI layers. This study proposes the polymerization of CH_2CHF molecules released on FEC decomposition to Li_2CO_3. Moreover, this study also proposes a reaction pathway for the formation of LiF by the reaction of poly-C_2HCHF and HF, explaining the high LiF concentrations found in FEC based SEI layers. ReaxFF further predicts the decomposition of FEC to occur in 80 ps, 3 times faster than EC decomposition to Li_2CO_3 which takes 250 ps in accordance with experimentally observed results[127].

3.3.2 EFFECTS OF DISSOLVED MANGANESE IN THE ANODE

A second set of simulations were conducted to study the fate of dissolved manganese in the SEI layer and the effect of manganese on the SEI layer composition. The simulation was run without manganese atoms for 700 ps to develop the SEI layer on the anode surface. Manganese atoms were then introduced and the simulation was continued for another 300 ps. The SEI layer was analyzed to identify the fate of the manganese atoms in the SEI layer and changes in its composition.

Figure 3.4 shows a representative snapshot of the SEI layer after 1 ns of simulation time at 303 K. The fate of the 12 manganese atoms introduced into the simulation cell are identified in Table 3.2. ReaxFF predicts the formation of zero valent metallic Mn cluster on the graphite surface. A number of studies have reported the deposition of metallic manganese[113,128] in the anode SEI layer while a few other studies[114,129] have disputed this claim. Mn atoms deposited on the surface of the anode in this study were those Mn atoms that were introduced less than 3 Å from the graphite surface. The ReaxFF model has been identified to overestimate the cohesive energy of metallic manganese, which could result in an unrealistic prediction of metal deposition. The current ReaxFF model for metallic manganese does not provide conclusive evidence for the deposition of metallic manganese on the anode surface. Manganese atoms in the simulation also ended up as inorganic $MnCO_3$. Manganese atoms open the ring structure of EC molecules to form a carbonate and release a C_2H_4 gas molecule. In the absence of $LiPF_6$ decomposition reactions, no manganese fluorides were formed.
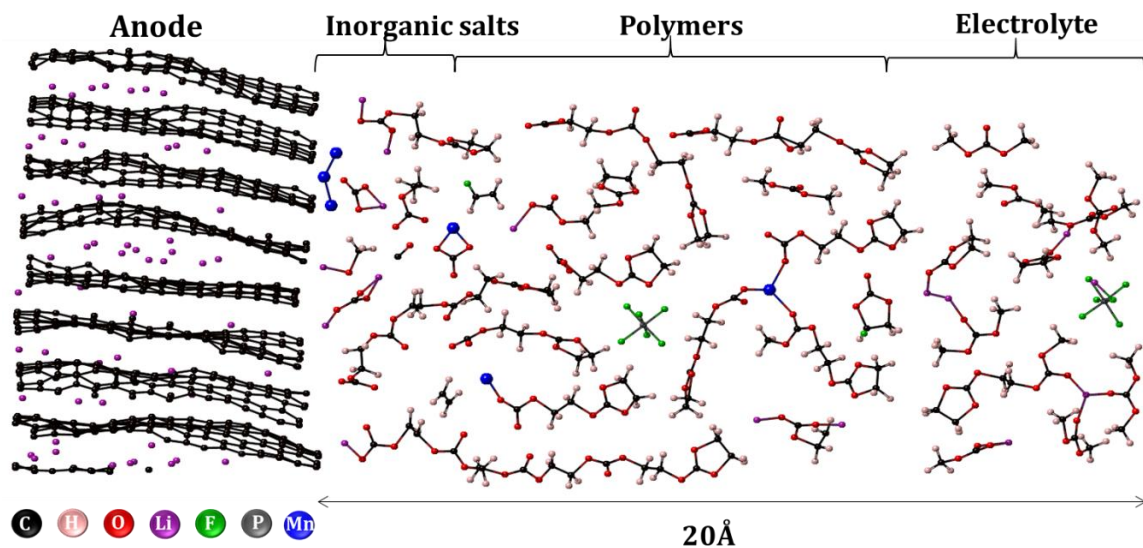
Figure 3.4 Simulation snapshot showing representative SEI layer compounds formed in the presence of Mn. The simulation ran for 700 ps, after which Mn atoms were introduced. The simulation was continued for another 300 ps at 303 K.

Table 3.2 Manganese compounds identified on the graphite anode after 300 ps at 303 K. A total of 12 manganese atoms were introduced into the simulation cell.

Mn compounds in the graphite SEI layer		
	Number of molecules (ReaxFF MD)	Exp. evidence
Metallic Mn	3	Gowda et al. [113] Ochida et al. [128]
MnCO$_3$	4	Delacourt et al. [115] Zhan et al. [114]
Solvated Mn	5	Gowda et al. [113] Shkrob et al. [129]

Over 40% of the introduced Mn atoms remain in the electrolyte without forming any salts. The Mn atoms are chelated by the carbonate oxygen atoms of the electrolyte solvent molecules. The Mn atoms in the electrolyte further catalyze the polymerization of EC and DMC. Figure 3.5 shows the unreacted EC and DMC as a fraction of the initial

composition with simulation time. There is a drastic decrease in the number of unreacted EC molecules in the 300 ps after the Mn atoms were introduced into the simulation. Analysis of the composition of the SEI layer after 1 ns of the simulation reveals an increased amount of polymers, especially EC polymers as reported in Figure 3.6. As can be seen in Figure 3.4, EC polymer chains consisting of 2-5 EC units extend from the surface of the anode into the electrolyte. The presence of these polymers change the composition and structure of the SEI layer presumably altering its viscosity, conductivity and stability. The possibility of structural and compositional changes in the SEI layer in the presence of Mn have been speculated previously[111,114]. Experimental studies have observed oxygen-rich SEI layer[130] in the presence of Mn, which can be explained by the presence of large organic carbonate polymers as observed in this study. The formation of a thick SEI layer[131] due to the catalytic activity[129] of Mn in the SEI further confirms the role of electrolyte solvent polymers in the capacity fade of batteries.
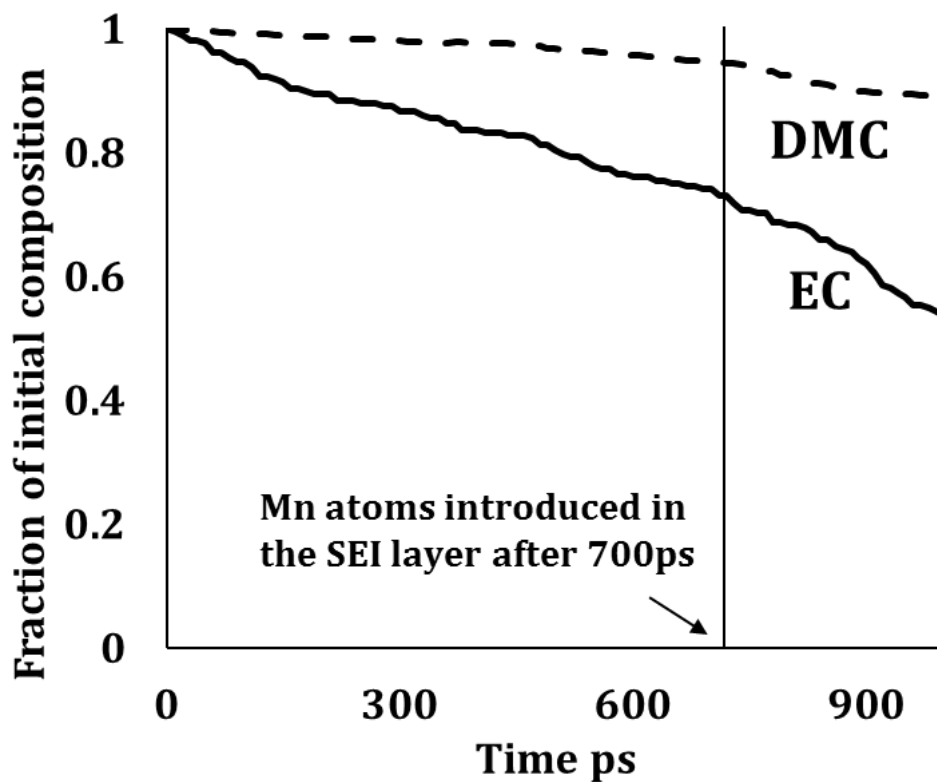
Figure 3.5 Time evolution of unreacted electrolyte solvent molecules represented as a fraction of initial composition.
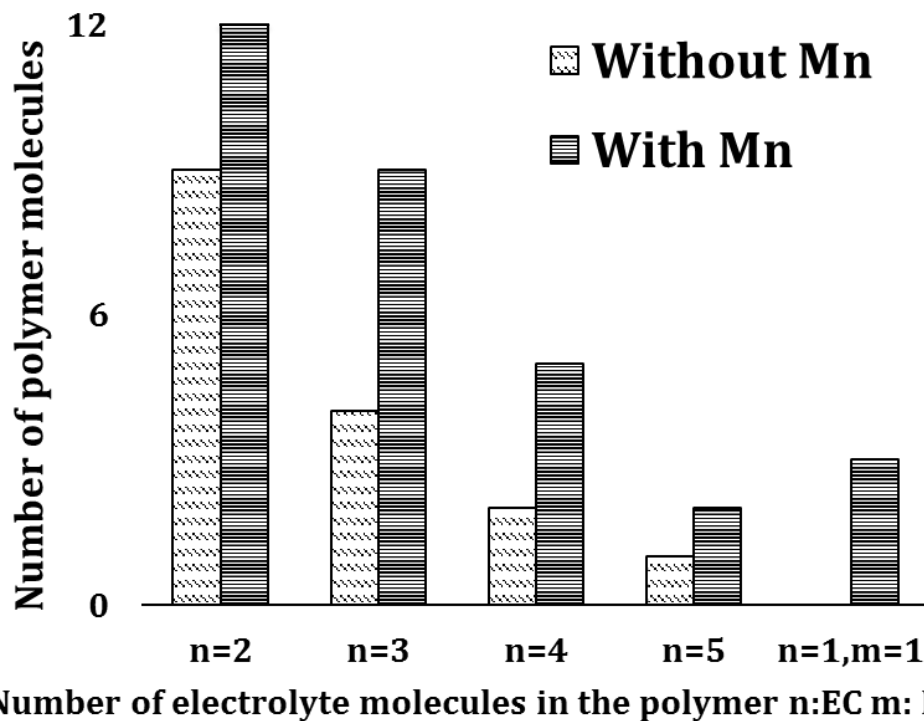
Figure 3.6 Polymer composition of the SEI layer after 1 ns with and without the introduction of Mn atoms after 700 ps.

3.4 CONCLUSION

The anode half-cell of $LiMn_2O_4$ based batteries is studied using ReaxFF based molecular dynamics to analyze the effect of FEC and dissolved manganese ions on the anode SEI layer. The simulations reveal that FEC decomposes at a faster rate than other electrolyte solvent molecules as proposed previously. The decomposition products of FEC were found to be Li_2CO_3 and CH_2CHF gas. The results of this study suggest that in the absence of $LiPF_6$ salt decomposition, FEC does not yield LiF; implying that FEC is not a direct source of the increased concentrations of LiF observed experimentally. In order to identify the source of LiF in FEC based anode SEI layers, the effect of FEC on salt decomposition needs to be further studied.

The ReaxFF model was also used to study the fate of manganese in the anode SEI layer and the effects of manganese atoms on the composition of the SEI layer. The simulations reveal that while some manganese atoms deposit as metallic manganese clusters and $MnCO_3$ molecules, most manganese atoms remain in solution chelated by carbonate oxygen atoms of the electrolyte solvent molecules. The chelated manganese atoms further catalyze the polymerization of ethylene carbonate molecules leading to the formation of large organic polymers extending from the surface of the anode into the electrolyte. This study reveals that apart from consuming electrons from the anode, dissolved manganese atoms change the composition of the SEI layer possibly increasing resistance to ion conduction through the SEI layer.

CHAPTER 4

CATHODE-ELECTROLYTE INTERFACE LAYER IN LITHIUM MANGANESE OXIDE BATTERIES: CHEMICAL COMPOSITION AND FORMATION REACTION MECHANISMS

4.1 CATHODE-ELECTROLYTE INTERFACE LAYER

Lithium manganese oxide ($LiMn_2O_4$) is the primary cathode material being exploited for high power and high energy density applications like electric vehicles (EV)[132] and renewable energy storage[133]. $LiMn_2O_4$ cathodes possess several advantages, such as low cost, non-toxicity and simple preparation process[134] as compared to other proposed cathode materials. However, there are well-documented problems with capacity fade of lithium ion batteries containing $LiMn_2O_4$ due to active material loss, caused by dissolution of divalent manganese from the cathode surface and deposition of dissolved manganese onto the anode[1]. The $LiMn_2O_4$ spinel consists of manganese ions in two oxidation states (Mn^{3+} and Mn^{4+}) in equal proportions to give a net manganese oxidation of $+3.5$[7]. Conventional wisdom holds that trivalent manganese ions are unstable to acid attack and are lost from the cathode surface into the electrolyte following charge disproportionation through the Hunter reaction[1],

$$2Mn^{3+} \rightarrow Mn^{4+}_{solid} + Mn^{2+}_{solution}$$

66
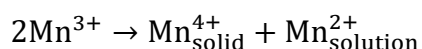
The dissolution of divalent manganese from the surface of the cathode into the electrolyte leads to a decrease in the effective amount of cathode material available for further lithium intercalation. Further, the deposition of the dissolved manganese ions on the anode decreases the Li content of the anode by consuming electrons from the anode.

The key to improving the capacity and service life of $LiMn_2O_4$ based cells is to understand the reactions that occur at the surface of the cathode leading to the dissolution of manganese ions. The cathode-electrolyte interface has only recently come to light as a potential impediment in the long term viability of Li-ion cells[135]. Advances in imaging techniques like Tunneling Electron Microscopy (TEM), have enabled the observation of the extremely thin (2 nm – 5 nm in thickness[136]) layer of compounds formed on the cathode surface. Electrochemical Impedance Spectroscopy (EIS) techniques have observed that the formation of a film on the cathode[8] is a source of increased cell impedance. EIS results imply that the compounds formed at the cathode-electrolyte interface are poor ion conductors, limiting the diffusivity of Li^+ ions through the interface[137]. The cathode-electrolyte interface is speculated to consist of a layer of electrolyte oxidation products and cathode active material salts formed due to the reduction of manganese ions[9]. Ex-situ analysis of the cathode surface by Infrared spectroscopy (IR) suggests the presence of polyethylene carbonate (PEC), which is proposed to have been derived from the oxidative polymerization of EC. But, this finding could not be confirmed via XPS due to overlap between the PEC and PVDF binder peaks[138] resulting in inconclusive spectroscopy analysis of the surface. The oxidation of other electrolyte solvents like DMC and FEC have been speculated but could not be confirmed through experiments. Chemical characterization of the interface is also

challenging as the concentrations of the interface compounds are below the detectable limits of NMR spectrometry and GCMS techniques[138]. Further, manganese ion deposits observed on the anode surface[114] provide strong evidence of manganese dissolution from the cathode, but its speciation and related reactions at the cathode-electrolyte interface have not yet been fully understood.

The cathode electrolyte interface layer was found to have a layered structure similar to the anode-electrolyte interface layer through Ar-ion sputtering experiments[139], but its composition and electrochemical characteristics differ vastly from the anode layer. Experiments have shown that the amount of Mn^{2+} present in the electrolyte increases with cycle number[10] suggesting that the cathode-electrolyte interface layer formed during the initial cycles does not prevent further decomposition of electrolyte, in contrast to the anode interface layer. The dynamic behavior of the cathode layer is attributed to organic radicals and ions that are formed via electrolyte oxidation, which further react with more solvent molecules resulting in a chain reaction[140]. Hence, the cathode-electrolyte interface layer can limit battery performance by consuming the electrolyte continuously as the cycling proceeds. Further, the $LiMn_2O_4$ surface is highly susceptible to the acidic species, HF, produced in the electrolyte via hydrolysis of $LiPF_6$ salt due to trace water present in the cell[141]. While HF is established as a putative trigger for Mn dissolution, the reaction mechanisms of HF induced Mn dissolution remains unknown. The dynamic nature, high organic content and susceptibility to acid attack make the reaction chemistry occurring on the cathode surface unique. Effective management of performance losses due to the cathode electrolyte layer can be achieved by understanding the dynamic reaction

mechanisms on the cathode surface and identifying strategies that can stabilize the cathode electrolyte interface layer.

A number of strategies have been adopted to improve cathode stability and decrease active material dissolution; these strategies have been reported to result in better cyclability of cathodes suggesting the formation of a stable and passivating cathode-electrolyte interface layer[142]. The most popular strategies are cathode modifications via active material doping and cathode surface coating. Mn sites in the $LiMn_2O_4$ spinel are doped with other transition metal cations (Ni^{143}, Fe^{143}, Co^{144}, Mg^{145},Zn^{145}, Al^{146}) to reduce the number of Mn^{3+} cations that are susceptible to acid attack. Spinel doping with Ni has proven to be especially successful at increasing the overall electrochemical performance of the cathode and reducing Mn dissolution rates, but this material was reported to show capacity loss after prolonged cycling due to surface film formation[147]. The other effective cathode modification is surface coatings that are designed to protect the cathode active material by either altering the chemistry at the cathode electrolyte interface or by acting as a physical barrier between the cathode active material and the electrolyte. Al_2O_3 is the most commonly used coating for transition metal based cathodes as it is known to scavenge HF, reducing the acidity of the cathode surface, and also reduces electrolyte decomposition at the cathode surface[148]. Surface coatings, however, have low lithium ion conductivity necessitating the optimization of coating thickness in order to act as an effective barrier to electrolyte oxidation while still conducting Li ions[149,6]. The use of electrolyte additives has been a successful strategy to suppress electrolyte decomposition on the anode surface. While a few compounds such as Vinylene Carbonate (VC) have been reported as potential additives to reduce electrolyte

degradation on the LiFePO$_4$ cathodes[150], these results could not be replicated on other cathode chemistries[151]. All of the above discussed strategies have been designed based on indirect evidence of increased cell performance without any knowledge of changes in actual surface chemistry induced by cathode modifications. In order to be able to devise more efficient cathode improvement strategies, insights into the composition and dynamics of the cathode electrolyte interface are essential.

Considering the challenges in characterizing the composition of the cathode electrolyte interface layer using experimental techniques, computational methods are a resource to probe nanoscale phenomena that are inaccessible by experiments. Computational methods have already been used to study the cathode electrolyte interface characteristics. Ogawa *et al.*[152] used quantum chemical molecular dynamics to study the transport properties of Li ions at the cathode electrolyte interface and determined that Li ions are solvated by EC molecules at the cathode surface. This study however did not consider the differences chemical composition between cathode-electrolyte interface and bulk electrolyte. In other work, DFT methods have been used to study the oxidation mechanisms of solvent molecules and salt anions[153,154] but most of the studies considered isolated solvents or anions that do not explicitly interact with the cathode. Leung *et al.*[155] conducted the first study on EC decomposition on LiMn$_2$O$_4$ surfaces revealing the generation of surface hydroxyl species (and possibly H$_2$O molecules) via H abstraction from EC as the primary reaction mechanism on the surface of the cathode. While this study provided invaluable insights into the chemical nature of the cathode surface, it is important to investigate the reactions occurring at the cathode surface in the presence of the complete electrolyte. We are yet to identify the products of the oxidative

70

decomposition of the solvent molecules, the fate of acidic species (HF) on the cathode surface and the complete reaction mechanism generating the cathode electrolyte interface layer.

This work applies reactive force field based molecular dynamics to investigate the reactions occurring at the $LiMn_2O_4$ cathode surface, and the mechanisms of manganese dissolution. The ability of ReaxFF to simulate the formation and dissociation of chemical bonds will help disclose the dynamic surface reaction chemistry of the cathode.

4.2 METHODS

The developed reactive force field is used to investigate the cathode-electrolyte interface layer in electrochemical cells with $LiMn_2O_4$ cathode, ethylene carbonate (EC)/ dimethyl carbonate (DMC) electrolyte, $LiPF_6$ salt and 5% fluoroethylene carbonate (FEC) additive. In order to probe manganese dissolution due to acid attack, HF is introduced into the simulation cell. Conventional wisdom holds that HF is generated within the battery when $LiPF_6$ molecules decompose and react with trace water molecules present in the electrolyte according to the following reactions[141],

$$LiPF_6 \leftrightarrow LiF + PF_5$$

$$PF_5 + H_2O \rightarrow POF_3 + HF$$
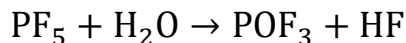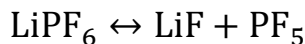
The focus of this work is to investigate the fate of the HF molecules on the cathode surface and not simulate the formation reactions of HF. Hence, in the interest of reducing the complexity of the study, the simulations assume the product of $LiPF_6$ decomposition (HF) to be present in the battery without simulating the actual decomposition

mechanisms. This assumption overlooks the effects of other $LiPF_6$ decomposition products on the cathode electrolyte interface. The inactive role of these decomposition products has not been proved or speculated but this assumption simplifies the system without compromising the purpose of this study.

4.2.1   MD SIMULATION

The formation of the cathode electrolyte interface layer was simulated using a cathode half-cell composed of a $LiMn_2O_4$ crystal with its 100 surfaces exposed to the electrolyte consisting of 208 EC molecules, 480 DMC molecules, 36 FEC molecules and 52 $LiPF_6$ molecules. The $LiMn_2O_4$ crystal measuring 3.5 nm x 3.5 nm x 3.5 nm is located at the center of the simulation box with dimensions of 10.5 nm x 3.5 nm x 3.5 nm, the rest of the simulation box is filled with the electrolyte as shown in Figure 4.1. This configuration helps with maintaining periodic boundary conditions in all three directions without any discontinuities. Bulk electrolyte character is maintained at distances greater than 2 nm from the electrode surfaces even after 2 ns, the maximum time period in this study. The equilibrium electrolyte density in the simulation cell is 1.26 g/cc with 3:7 mole ratio[117] of ethylene carbonate (EC) and dimethyl carbonate (DMC), 1M lithium hexafluorophosphate and 5% fluoroethylene carbonate.
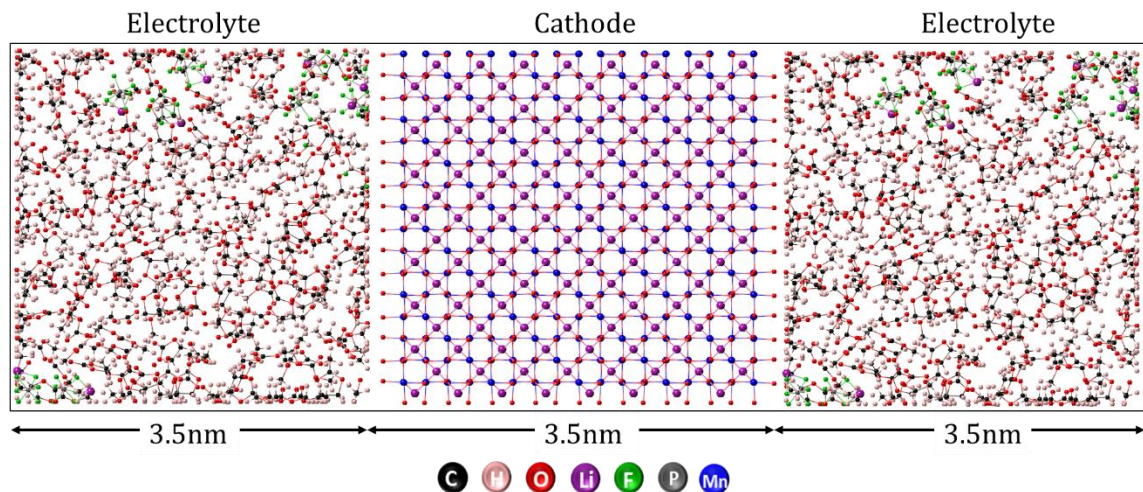
Figure 4.1 The starting configuration of the simulation cell with the cathode in the center. The 100 surface is exposed to the electrolyte on both sides.

The simulation cells were maintained at 330 K under the NVT ensemble using the Nosé Hoover thermostat with a temperature rescaling constant of 10 fs. The starting configuration of the electrolyte molecules was generated using the PACKMOL[118] code to make sure short range repulsive forces do not disrupt the simulation during the first time step. Each MD simulation was initiated from an energy-minimized structure and was equilibrated to the simulation temperature for 100 ps prior to the production run for 2 ns with a 0.2 fs time step.

The fate of HF on the cathode surface was studied by running a duplicate simulation as described above and introducing HF molecules into the simulation after 1.5 ns of cathode electrolyte interface layer formation. The HF molecules were introduced at random locations within a distance of 10 Å from the surface of the anode. HF molecules are introduced into the cathode electrolyte interface layer at a rate of 0.5 molecules/ps with a total of 10 molecules introduced into the simulation cell. After the introduction of HF molecules, the simulations were run for an additional 500 ps.

The ReaxFF based MD simulations were implemented using the LAMMPS parallel molecular dynamics code[89]. Molecular analysis of the simulations, to identify SEI layer compounds, were performed using a bond order cutoff of 0.2[36] as implemented in a home built MATLAB code.

4.3 RESULTS

This work sets out to investigate the reaction mechanisms that result in the formation of the cathode-electrolyte interface layer. The reaction pathways of electrolyte molecule oxidation will be elucidated, the role of HF in the dissolution reaction will be determined and finally, the overall reaction mechanism on the surface of the cathode will be discussed.

4.3.1 ELECTROLYTE SOLVENT DECOMPOSITION MECHANISMS

The ReaxFF based MD simulations of the cathode-half cell reveal a layer, 10 Å in thickness, consisting mainly of electrolyte solvent oxidation products formed on the cathode surface after 2 ns of simulation at 330 K. Figure 4.2 shows the primary compounds identified on the cathode surface. The ReaxFF model predicts a highly organic cathode-electrolyte interface consisting of compounds very similar to those speculated by other researchers[138,156,157,158]. At least three different oxidation products of EC were found in the simulation cell after 2 ns depending on the reaction pathway followed. The oxidation of EC also triggers polymerization, yielding large organic molecules as observed by other studies on EC oxidation[156]. While EC is most susceptible to oxidation on the cathodes surface, oxidation products of DMC and FEC are also present in the layer.
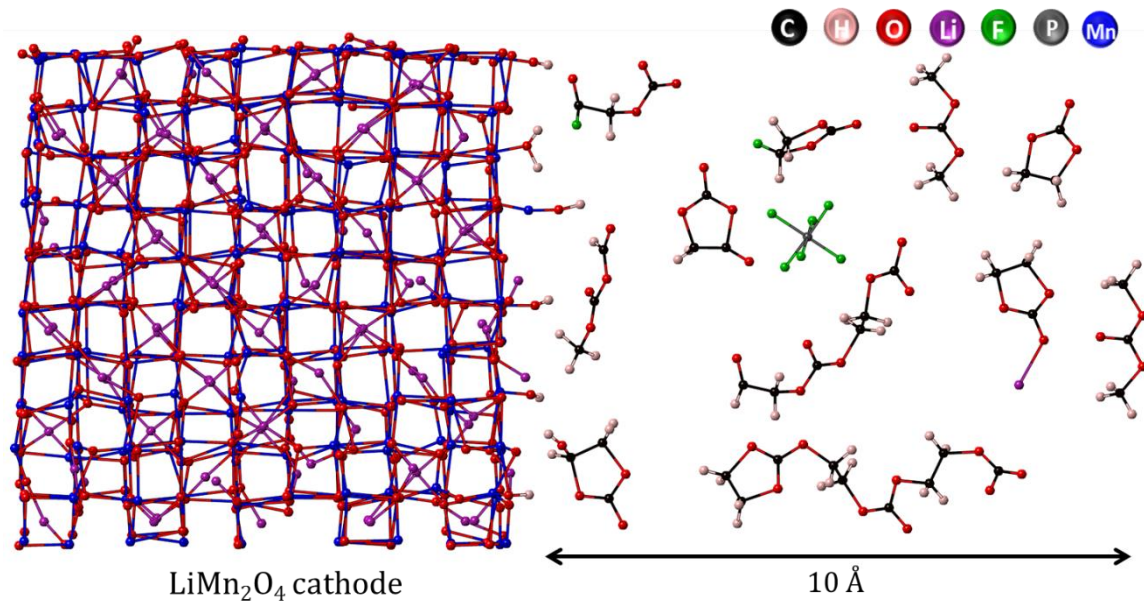
Figure 4.2 The simulation snapshot for ReaxFF force field based MD simulation of LiMn$_2$O$_4$ cathode, EC/DMC electrolyte, LiPF$_6$ salt and FEC electrolyte additive. This snapshot shows the primary compounds present in the cathode-electrolyte interface layer after for 2 ns at 330 K under NVT ensemble.

Figure 4.3 identifies the primary oxidation pathways of the three solvent molecules. The oxidation pathway of the solvents has been found to be very similar to the pathway reported by Leung *et al.*[155], proceeding via alkyl hydrogen abstraction and consequent lattice oxygen removal. The surface lattice oxygen atoms take up the hydrogen atoms from the alkyl groups of the solvent molecules resulting in a surface hydroxyl group and an organic radical adsorbed onto the cathode surface. After about 150 ps – 600 ps (depending on the reacting solvent molecule, see Figure 4.3), the organic radical pulls out a lattice oxygen atom which is made available due to the reduced oxidation state of the surface manganese atoms in the presence of a nearby hydroxyl species. The removal of lattice oxygen results in the formation of organic aldehyde groups, ester groups and polycarbonate species in the case of EC oxidation. DMC and FEC are found to be oxidized to only one type of product with no evidence of

polymerization. The organic radicals formed after H abstraction from EC often react with available surface hydroxyl groups resulting in the formation of alcohol groups. Unlike the anode electrolyte interface layer, no inorganic carbonates or organic lithium salts have been predicted by the ReaxFF model in the absence of salt decomposition; this is in good agreement with experimental evidence[159]. The oxidation reaction time for the solvent molecules range between 70 ps – 650 ps and increase in the order of FEC<EC<DMC.

The oxidation reaction pathways for all the electrolyte solvent molecules reveal the formation of surface hydroxyl species. The removal of oxygen from the cathode lattice exposes manganese atoms to the bulk electrolyte, which react with the surface hydroxyl species to form manganese hydroxide that is no longer a part of the lattice structure. The hydroxyl molecules are further, found to form water molecules that are likely to hydrolyze the $LiPF_6$ salt yielding HF. The formation of hydroxyl species and removal of lattice oxygen atoms, together result in manganese dissolution from the cathode into the electrolyte. The role of lattice oxygen vacancy formation on manganese dissolution has been speculated by previous experimental work using XAS analyses on cathode surfaces[160]. ReaxFF predictions of lattice oxygen removal during oxidation of electrolyte solvent molecules confirms the role played by oxygen vacancies on manganese dissolution and provides further insights into the reaction mechanisms that lead to lattice oxygen removal.

EC decomposition reaction
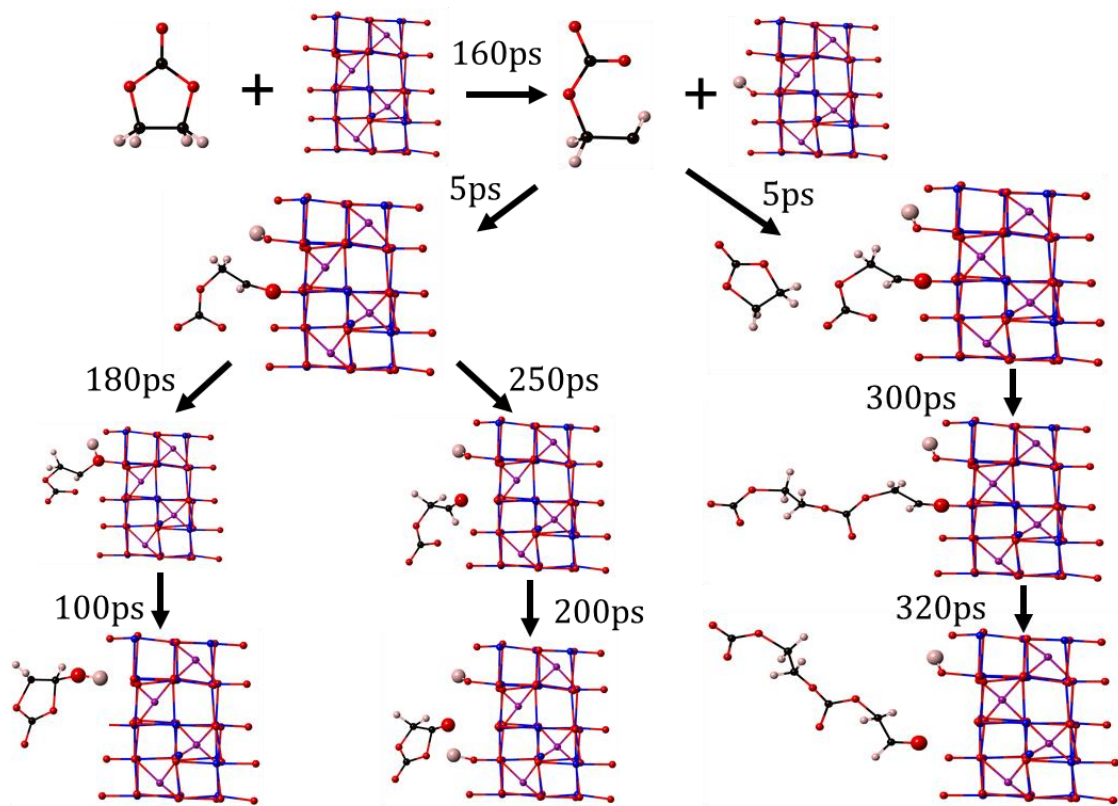
DMC decomposition reaction
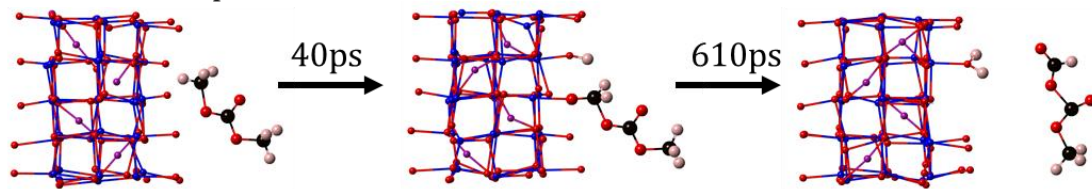
FEC decomposition reaction
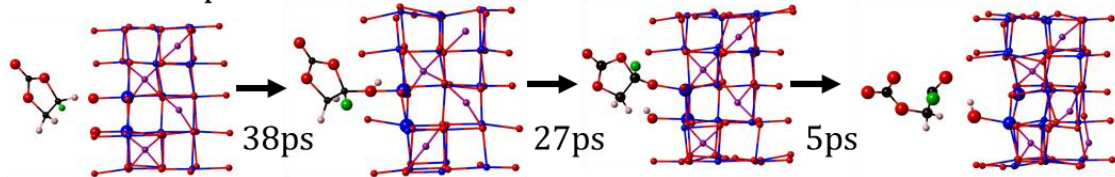
Figure 4.3 Oxidation pathways of electrolyte solvent molecules on the cathode surface.

4.3.2　FATE OF HF ON THE CATHODE SURFACE

HF in the lithium ion cells is believed to be a byproduct of $LiPF_6$ hydrolysis due to the presence of trace water molecules. But, the results from this study show that water molecules can be formed on the cathode surface during electrolyte oxidation. This finding implies that even in the absence of water as an impurity, HF can be formed by the hydrolysis of $LiPF_6$ salt via water molecules generated through electrolyte oxidation on the cathode surface. Therefore, HF is an inevitable part of the battery chemistry and considering that HF is a putative trigger for manganese dissolution, its fate on the cathode surface is an essential part of the cathode-electrolyte interface chemistry. In order to probe its fate on the cathode surface, HF is introduced into the simulation cell after 1.5 ns. A total of 10 HF molecules are introduced within 10 Å from the cathode surface and the cathode interface layer composition is analyzed after 500 ps.

The introduction of HF into the simulation cell results in a consequent rise in the number of surface hydroxyl species on the cathode. Figure 4.4 shows the primary compounds identified in the cathode electrolyte interface after 500 ps of simulation in the presence of HF molecules. The number of $Mn(OH)_2$ molecules also increases in the presence of HF. As can be seen in Figure 4.2, the manganese atoms that form $Mn(OH)_2$ are pulled out of the cathode lattice structure on bond formation with the surface hydroxyl species. The Mn-OH species observed in the simulation remain adsorbed on the cathode surface but, it is highly likely that manganese atoms are solvated by the electrolyte compounds leading to the dissolution of manganese at longer timescales. The fluoride anions from HF mostly end up as fluorinated salts of manganese (MnF_2) and lithium (LiF), which are the only inorganic salts present on the cathode surface, as

78

observed experimentally[161]. Organic radicals formed after alkyl hydrogen abstraction from electrolyte solvent molecules also react with HF to yield fluorinated organic solvents.

The presence of HF results in an increased amount of surface hydroxyl species and the formation of inorganic salts on the surface of the cathode. While the hydroxyl species react with manganese atoms displacing the metal atoms from the cathode lattice, the fluoride anions react with metal atoms to form inorganic salts which may help passivate the cathode surface in the long run. ReaxFF analysis yields insights into the acid attack mechanism occurring on the cathode surface and reveals that scavenging hydroxyl molecules formed on the surface of the cathode may lead to the formation of a stable cathode-electrolyte interface layer.
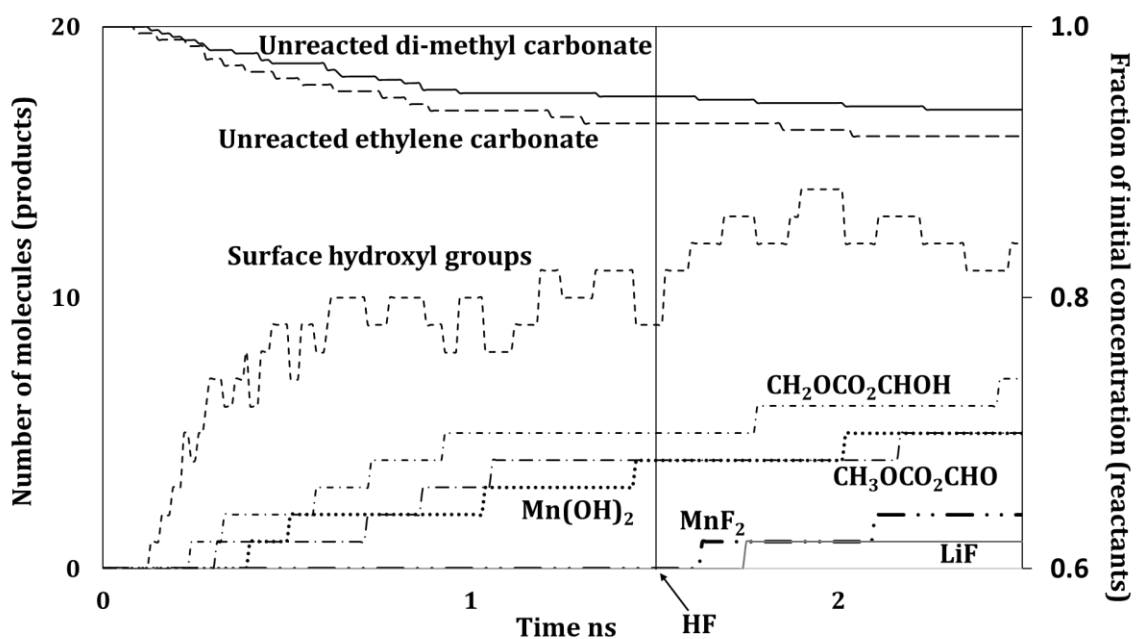
Figure 4.4 Time evolution of primary products and reactants in the cathode-electrolyte interface layer.

4.3.3   CATHODE-ELECTROLYTE INTERFACE LAYER FORMATION REACTION MECHANISM

Based on the ReaxFF MD analysis of the $LiMn_2O_4$ cathode electrolyte interface layer, the formation reaction scheme can be illustrated as shown in Figure 4.5. The electrolyte solvent molecules undergo alkyl hydrogen abstraction and oxidation via the removal of lattice oxygen atoms on the cathode surface. This oxidation process results in the formation of organic aldehydes, esters and alcohols that compose the cathode electrolyte interface layer. The oxidation reaction also results in the production of surface hydroxyl species that react with manganese atoms displacing them from the lattice. The hydroxyl species also form water molecules. The manganese hydroxide molecules and water molecules are likely to be released into the electrolyte. The formation of water molecules is likely to contribute to the continuous degradation of the cathode electrolyte interface layer due to salt hydrolysis that yields HF molecules[162], further explaining the non-passive nature of the cathode electrolyte interface layer. The presence of HF in the electrolyte adds to the formation of surface hydroxyl species and yields metal fluorides. Manganese fluoride, lithium fluoride and fluorinated solvent molecules can be found in the cathode electrolyte interface layer. The components of the cathode electrolyte interface layer identified by this work (excluding the compounds produced due to salt decomposition) are similar to those speculated by previous studies[163,164]. This work adds to previously established cathode-electrolyte interface reaction schemes[165,166] by providing detailed to reaction mechanism. The ReaxFF analysis also establishes that the formation of hydroxyl species is central to the formation and non-passivating nature of the cathode-electrolyte interface layer.
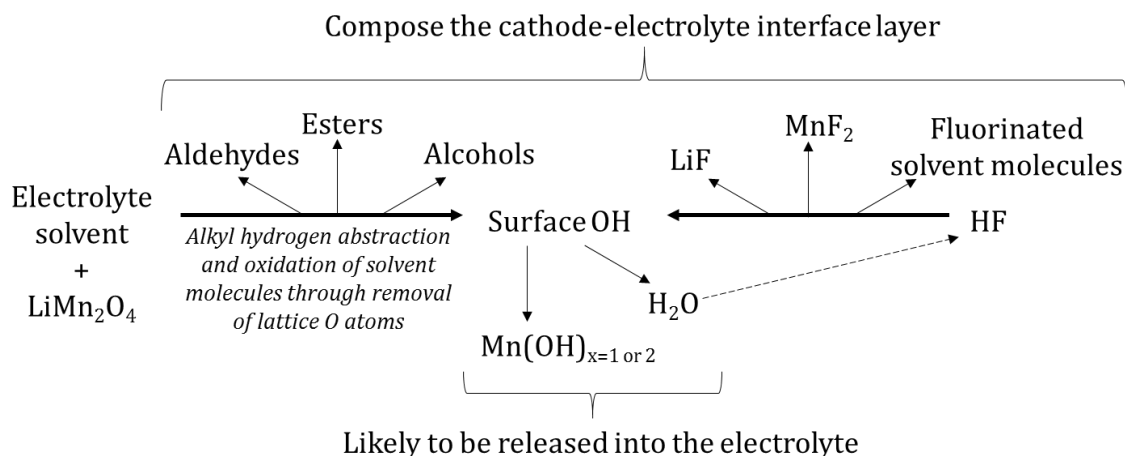
Figure 4.5 Reactions leading to the formation of the cathode-electrolyte interface. Solid lines indicate products as predicted by ReaxFF and dashed line indicates a proposed reaction pathway[141].

4.4 CONCLUSION

The formation of the cathode-electrolyte interface layer was investigated using ReaxFF based molecular dynamics. The MD simulations reveal that the cathode-electrolyte interface layer is mainly composed of oxidation products of electrolyte solvent molecules such as aldehydes, esters, alcohols, polycarbonates and organic radicals. The electrolyte solvent molecules undergo oxidation by removing lattice oxygen atoms and producing surface hydroxyl species. In the presence of HF, increased number of hydroxyl species, metal fluorides and fluorinated organic solvent molecules were formed. Manganese dissolution was aided by the removal of lattice oxygen atoms that expose manganese atoms to the bulk electrolyte, and the formation of surface hydroxyl species that react with the exposed manganese atoms and displace the atoms from the cathode lattice.

The cathode-electrolyte surface compounds predicted by the ReaxFF model are in good agreement with the experimentally observed products. The ReaxFF analysis yielded

insights into the acid attack mechanism occurring on the cathode surface, establishing that the generation of hydroxyl species is central to the formation and non-passivating nature of the cathode-electrolyte interface layer as well as the issue of manganese dissolution. The results of this work imply that developing strategies to scavenge hydroxyl molecules formed on the surface of the cathode will help in the formation of a stable cathode-electrolyte interface layer. Furthermore, this work also developed a detailed formation reaction pathway for the cathode-electrolyte interface layer with insights into the exact chemical compounds that can be found on the cathode surface. This information will be especially useful to future studies looking to bridge gaps between computational and experimental techniques.

CHAPTER 5

CONCLUSION

5.1 SUMMARY

A competitive electric vehicle and renewable energy market necessitates a twenty-fold increase in the current market share of energy storage technology. Meeting this demand requires the development of new energy storage technologies as well as the improvement of the existing Li-ion batteries. The current generation of Li-ion batteries are vulnerable to a number of degradation mechanisms, occurring alongside the main electrochemical reaction, that consume active material in the cell and limit the practically achievable performance of this technology. Understanding the origin of the degradation mechanisms and devising strategies to overcome the loss of active material through the degradation reactions will significantly increase the performance of these batteries by improving their energy density, cycle life, affordability and safety.

The abundance, low cost, and non-toxic nature of manganese makes its incorporation into Li-ion cathodes attractive. Manganese-rich cathode materials are thus a frontrunner as electrodes for the next generation high power applications. The most critical drawback of manganese based cathodes, however, is the dissolution of manganese that occurs from the bulk cathode into the electrolyte. The mechanisms associated with

manganese dissolution, and the fate of dissolved manganese, are not yet well understood in spite of the incriminating experimental evidence of capacity loss and reduced cycle life that occurs during the aging of manganese containing cathodes. The rapid reaction dynamics and low in situ concentrations of the dissolution and deposition phenomena make them inaccessible to study using experimental techniques. Computational methods such as molecular dynamics are thus useful to reveal the nanoscale molecular processes that lead to macroscopic battery degradation.

In this dissertation, reactive force field based molecular dynamics was applied to lithium manganese oxide battery cells to investigate the reactions occurring at both the cathode-electrolyte interface, the origin of manganese dissolution, and the anode-electrolyte interface, the experimentally observed deposition site of dissolved manganese. Specifically, the ReaxFF model was optimized for a battery system containing the elemental constituents, manganese, fluorine, lithium, carbon, hydrogen and oxygen, and molecular dynamics simulations were conducted on $LiMn_2O_4$ based cells to investigate the following:

i. The fate of dissolved manganese in the anode-electrolyte interface layer, with identification of the manganese compounds present in the layer and investigation of the effects of manganese atoms on the stability of the anode-electrolyte interface layer.

ii. The reaction pathways for cathode dissolution, and the role of impurities in the dissolution reaction, so as to elucidate the overall reaction mechanism that results in the formation of the cathode-electrolyte interface layer and the compounds that comprise the layer.

The developed ReaxFF model reproduced the DFT derived equations of state, heats of formation, bond stretching energies, angle bending energies, reaction enthalpies and charge distributions of compounds representative of the interactions occurring in a $LiMn_2O_4$ based electrochemical cell. The model was further validated against experimental data for the high temperature oxidation of methane over manganese oxide surfaces. The developed model not only accurately predicts the experimentally observed products of manganese oxide reduction with methane, but also reveals the reaction intermediates that are formed.

The validated ReaxFF model was used to probe the decomposition of fluoroethylene carbonate (FEC) and the fate of dissolved manganese on the surface of the anode. The simulations revealed that FEC decomposes at a faster rate than other electrolyte solvent molecules as proposed previously[127]. The decomposition products of FEC were found to be the inorganic compound-Li_2CO_3 and CH_2CHF gas. While some manganese atoms were found to deposit as metallic manganese clusters and $MnCO_3$ molecules on the anode surface, most manganese atoms remain in solution, chelated by carbonate oxygen atoms of the electrolyte solvent. The chelated manganese atoms catalyze polymerization of ethylene carbonate molecules leading to the formation of large organic polymers extending from the surface of the anode into the electrolyte. This study reveals that apart from consuming electrons from the anode, dissolved manganese atoms change the composition of the anode SEI layer possibly increasing resistance to ion conduction through the SEI layer.

The $LiMn_2O_4$ cathode half-cell was analyzed using the ReaxFF model. The simulations reveal that the cathode-electrolyte interface layer is mainly composed of the

oxidation products of electrolyte solvent molecules such as aldehydes, esters, alcohols, polycarbonates and organic radicals. Electrolyte solvent molecules undergo oxidation by removal of lattice oxygen atoms, producing surface hydroxyl species. In the presence of hydrogen fluoride (HF), an increased number of hydroxyl species, metal fluorides and fluorinated organic solvent molecules are formed. Manganese dissolution is aided by the removal of lattice oxygen atoms to expose manganese atoms to the bulk electrolyte, and by the formation of surface hydroxyl species that react with the exposed manganese atoms and displace them from the cathode lattice.

The cathode-electrolyte surface compounds predicted by the ReaxFF model are in good agreement with the experimentally speculated products[138,156,157]. The ReaxFF analysis yielded insights into the acid attack mechanism occurring on the cathode surface, establishing that the generation of hydroxyl species is central to the formation and the non-passivate nature of the cathode-electrolyte interface layer and the process of manganese dissolution. The results of this investigation suggest that strategies that scavenge hydroxyl radicals formed on the surface of the cathode will help to stabilize the cathode-electrolyte interface layer. Furthermore, this study identified a detailed formation reaction pathway for the cathode-electrolyte interface layer with insights into the specific chemical compounds that can be found on the cathode surface. The results of this study provide evidence for the non-passivated conditions at the cathode-electrolyte layer and continual degradation of the cathode and electrolyte throughout the battery lifetime.

This work revealed the nano-scale phenomena that lead to macroscopic performance loss in batteries and suggests a route to develop high capacity, long-lived, low cost energy storage devices. The reactive force fields and DFT property compilations

developed in this dissertation are valuable additions to the body of knowledge on interatomic potentials used by researchers in many disciplines of science and engineering.

5.2 LIMITATIONS

5.2.1 METALLIC MANGANESE COHESIVE ENERGIES

The ReaxFF model accurately captures the DFT predictions of the cohesive energy of metallic manganese, but the theoretical predictions of the manganese cohesive energy differ substantially from the experimentally reported value. It is known that manganese has unusual properties, e.g., a low boiling point, as compared to other transition metals, and this can be attributed to the low cohesive energy of manganese. For purposes of validation, the experimental cohesive energy for manganese[46] was extrapolated from high temperature data, making it less reliable. However, it is nonetheless important to note that the theoretical models overestimate the metallic manganese cohesive energy.

The implications of this limitation can be recognized in the study of the anode-electrolyte interface. The ReaxFF model predicts the deposition of metallic manganese clusters on the surface of the anode which may result from the inability of the force field to accurately capture the energetics of metallic manganese. Hence, the current ReaxFF model does not provide conclusive evidence that deposition of metallic manganese will occur on the actual graphite anode surface. To resolve this uncertainty, future versions of the force field for manganese should be optimized to a more reliable experimental value for the manganese cohesive energy.

5.2.2 LITHIUM MANGANESE OXIDE SURFACES AND HEAT OF FORMATION

The ReaxFF model used in this dissertation is only able to reproduce the DFT derived energetics for the 100 surface of $LiMn_2O_4$ that is of principal interest in this study. A considerable amount of optimization is required to capture the energetics of other $LiMn_2O_4$ surfaces. This can be achieved by increasing the weightings associated with other surfaces during the optimization of the ReaxFF parameters.

The ReaxFF model was able to reproduce the heats of formation of spinel structures with high lithium loading but it was unable to capture the energetics of spinel structures at lower charge levels. The scope of this investigation was limited to lithium loadings of x=1, but the use of this force field to simulate $LiMn_2O_4$ cathode charge and discharge requires further improvement in the ReaxFF model.

5.2.3 PHOSPHORUS INTERACTIONS

The chemistry of the electrode-electrolyte interfaces in $LiMn_2O_4$ based batteries, as revealed via ReaxFF based MD in this study, did not include the potential effects of phosphorus reactivity. Decomposition of $LiPF_6$ electrolyte salt into highly reactive phosphorus compounds has been observed experimentally to play an important role in the composition of the electrode-electrolyte interface layers. However, the scope of this study was limited to non-reactive phosphorus, so as to focus the analysis on the electrode-electrolyte reaction chemistry that results from the dissolution and deposition of the cathode active material. Since the absence of $LiPF_6$ salt decomposition under the conditions in this study has not been proven or speculated, the results of this study do not paint a complete picture of the composition of the electrode-electrolyte interface layers,

or the entirety of the molecular phenomena occurring in the battery cells. In order to investigate the phosphorus-containing compounds formed in the batteries, the current ReaxFF model requires further optimization to include the interaction parameters of phosphorus with all of the other elements present in the system.

5.3 RECOMMENDATIONS FOR FUTURE WORK

The findings from this study provide a fundamental understanding of the molecular phenomena that occur at the electrode-electrolyte interfaces. Such an understanding is essential to inform research on strategies to develop stable electrode-electrolyte interface layers and prevent the loss of electrode active material. This work provides the preliminary results for the following future studies,

- Battery cycling effects: The Li-ion electrochemical cell simulations conducted in this study represent a battery storage scenario only. Li-ion intercalation and de-intercalation during battery cycling will affect the chemistry of the electrode-electrolyte interface layers. Further, the study of cycling effects will yield information about the transport dynamics of ions through the interfaces.

- Bridging scales in Li-ion battery research: This work provides information on the previously unknown chemical structure of the cathode-electrolyte interface layer. Larger scale models can now be developed to incorporate the molecular scale phenomena occurring at the cathode interface in order to represent a more realistic battery model.

Apart from laying the ground work for the afore mentioned follow-on studies, the results from this dissertation also suggest new research directions that can be pursued to

develop novel strategies for improving $LiMn_2O_4$ based battery performance. These include the following:

- <u>Effect of FEC on salt decomposition</u>: The results of this study suggest that in the absence of $LiPF_6$ salt decomposition, FEC does not yield LiF, implying that FEC is not a direct source of the increased concentrations of LiF observed experimentally[167]. While FEC is used as an additive primarily to form a stable SEI layer, studies have speculated on its role in enhancing $LiPF_6$ salt decomposition, a likely cause of undesirable LiF formation. Considering the results from this study, the effect of FEC on salt decomposition should be further investigated in order to gain insights into the overall effects of FEC in the battery system.

- <u>Manganese chelating electrolyte additives</u>: Dissolved manganese ions were found to be chelated by the carbonate oxygen atoms of the electrolyte solvent molecules. Further research on electrolyte additives that are strong chelating agents for dissolved Mn will help to prevent both manganese deposition on the anode and polymerization of electrolyte solvent molecules on the anode surface.

- <u>Hydroxyl ion scavengers</u>: A number of cathode coatings are already being used as HF scavengers to reduce the acidic species on the cathode surface. The results from this research suggest that surface hydroxyl molecules lead to further electrolyte decomposition, lattice oxygen removal and metal ion leaching. The ReaxFF model also suggests that HF molecules react with metal ions to form metal fluorides and more surface hydroxyl species. Hence, research into hydroxyl ion-scavenging cathode coatings and electrolyte additives will help to counteract the degradation reactions occurring at the cathode surface.

APPENDIX A: REAXFF MODEL PARAMETERS (FFIELD)

```
Reactive MD-force field: c/h/o/Mn/F/Li
 39        ! Number of general parameters
   50.0000 !Overcoordination parameter
    9.5469 !Overcoordination parameter
    1.6725 !Valency angle conjugation parameter
    1.7224 !Triple bond stabilisation parameter
    6.8702 !Triple bond stabilisation parameter
   60.4850 !C2-correction
    1.0588 !Undercoordination parameter
    4.6000 !Triple bond stabilisation parameter
   12.1176 !Undercoordination parameter
   13.3056 !Undercoordination parameter
  -55.1978 !Triple bond stabilization energy
    0.0000 !Lower Taper-radius
   10.0000 !Upper Taper-radius
    2.8793 !Not used
   33.8667 !Valency undercoordination
    6.0891 !Valency angle/lone pair parameter
    1.0563 !Valency angle
    2.0384 !Valency angle parameter
    6.1431 !Not used
    6.9290 !Double bond/angle parameter
    0.3989 !Double bond/angle parameter: overcoord
    3.9954 !Double bond/angle parameter: overcoord
   -2.4837 !Not used
    5.7796 !Torsion/BO parameter
   10.0000 !Torsion overcoordination
    1.9487 !Torsion overcoordination
   -1.2327 !Conjugation 0 (not used)
    2.1645 !Conjugation
    1.5591 !vdWaals shielding
    0.1000 !Cutoff for bond order (*100)
    1.7602 !Valency angle conjugation parameter
    0.6991 !Overcoordination parameter
   50.0000 !Overcoordination parameter
    1.8512 !Valency/lone pair parameter
    0.5000 !Not used
   20.0000 !Not used
    5.0000 !Molecular energy (not used)
    0.0000 !Molecular energy (not used)
    0.7903 !Valency angle conjugation parameter
  9    ! Nr of atoms; cov.r; valency;a.m;Rvdw;Evdw;gammaEEM;cov.r2;#
          alfa;gammavdW;valency;Eunder;Eover;chiEEM;etaEEM;n.u.
          cov r3;Elp;Heat inc.;n.u.;n.u.;n.u.;n.u.
          ov/un;val1;n.u.;val3,vval4
 C   1.3817   4.0000  12.0000   1.8903   0.1838   0.6387   1.1341   4.0000
     9.7559   2.1346   4.0000  34.9350  79.5548   4.9218   6.0000   0.0000
     1.2114   0.0000 202.2900  88.9539  34.9289  13.5366   0.8563   0.0000
    -2.8983   2.5000   1.0560  44.0000   2.9663   0.0000   0.0000   0.0000
```

```
H    0.8930    1.0000    1.0080    1.3550    0.0930    0.8203   -0.1000    1.0000
     8.2230   33.2894    1.0000    0.0000  121.1250    3.7248    9.6093    1.0000
    -0.1000    0.0000   55.1870   83.0408    2.4197    0.0003    1.0698    0.0000
   -19.4571    4.2733    1.0330   81.0000    2.8793    0.0000    0.0000    0.0000
O    1.2450    2.0000   15.9990    2.3890    0.1000    1.0898    1.0548    6.0000
     9.7300   13.8449    4.0000   37.5000  116.0768    8.5000    8.3122    2.0000
     0.9049    0.4056   68.0152    3.5027    0.7640    0.0021    0.9745    0.0000
    -3.5500    2.9000    1.0493    4.0000    2.9225    0.0000    0.0000    0.0000
Mn   2.2190    7.0000   54.9380    1.9685    0.3855    0.4633    0.1000    6.0000
    11.2058    4.1928    4.0000    0.0000    0.0000   -1.0000    6.1911    0.0000
     0.1000    0.0000  152.6300    3.4529    0.0722    3.1767    0.8563    0.0000
   -25.0000    3.1072    1.0338    8.0000    3.4590    0.0000    0.0000    0.0000
Li   1.9814    1.0000    6.9410    1.8000    0.2939    0.9387   -0.1000    1.0000
     9.0616    1.3258    1.0000    0.0000    0.0000   -3.0000   10.0241    0.0000
    -1.0000    0.0000   37.5000    5.4409    6.9107    0.1973    0.8563    0.0000
    -2.5068    2.2989    1.0338    1.0000    2.8103    1.3000    0.2000   13.0000
F    1.7938    1.0000   18.9984    1.4139    0.3134    0.7750   -0.1000    7.0000
    10.3051   15.1397    1.0000    9.2533    0.2000    9.8105    8.6941    0.0000
    -1.0000    3.5571   18.0000    6.9821    4.1799    1.0561    0.0000    0.0000
    -6.3417    2.6656    1.0493    4.0000    2.9225    0.0000    0.0000    0.0000
P    1.5994    3.0000   30.9738    1.7000    0.1743    1.0385    1.3000    5.0000
     9.1909   14.2932    5.0000    0.0000    0.0000    0.9528    7.9121    0.0000
    -1.0000   10.2596    1.5000    0.2205   16.7429   15.9629    0.0000    0.0000
    -2.5000    1.6114    1.0338    5.0000    2.8793    0.0000    0.0000    0.0000
Ni  -0.1000    2.0000    1.0080    2.0000    0.0000    1.0000   -0.1000    6.0000
    10.0000    2.5000    4.0000    0.0000    0.0000    8.5000    1.5000    0.0000
    -0.1000    0.0000   -2.3700    8.7410   13.3640    0.6690    0.9745    0.0000
   -11.0000    2.7466    1.0338    6.2998    2.8793    0.0000    0.0000    0.0000
Al  -0.1000    2.0000    1.0080    2.0000    0.0000    1.0000   -0.1000    6.0000
    10.0000    2.5000    4.0000    0.0000    0.0000    8.5000    1.5000    0.0000
    -0.1000    0.0000   -2.3700    8.7410   13.3640    0.6690    0.9745    0.0000
   -11.0000    2.7466    1.0338    6.2998    2.8793    0.0000    0.0000    0.0000
28       ! Nr of bonds; Edis1;LPpen;n.u.;pbe1;pbo5;13corr;pbo6
                      pbe2;pbo3;pbo4;Etrip;pbo1;pbo2;ovcorr
 1  1 158.2004   99.1897   78.0000   -0.7738   -0.4550    1.0000   37.6117    0.4147
        0.4590   -0.1000    9.1628    1.0000   -0.0777    6.7268    1.0000    0.0000
 1  2 169.4760    0.0000    0.0000   -0.6083    0.0000    1.0000    6.0000    0.7652
        5.2290    1.0000    0.0000    1.0000   -0.0553    6.9316    0.0000    0.0000
 2  2 153.3934    0.0000    0.0000   -0.4600    0.0000    1.0000    6.0000    0.7300
        6.2500    1.0000    0.0000    1.0000   -0.0790    6.0552    0.0000    0.0000
 1  3 115.3161  127.1562   61.7072    0.5141   -0.3474    1.0000   18.9948    0.9954
        1.5618   -0.3414    8.9489    1.0000   -0.1628    5.6821    0.0000    0.0000
 3  3 142.2858  145.0000   50.8293    0.2506   -0.1000    1.0000   29.7503    0.6051
        0.3451   -0.1055    9.0000    1.0000   -0.1225    5.5000    1.0000    0.0000
 2  3 160.0000    0.0000    0.0000   -0.5725    0.0000    1.0000    6.0000    0.5626
        1.1150    1.0000    0.0000    0.0000   -0.0920    4.2790    0.0000    0.0000
 1  4  49.3020   10.0000    0.0000   -1.0302   -0.3000    1.0000   36.0000   -0.0099
        1.8910   -0.4204    7.6871    1.0000   -0.0880    6.6676    1.0000    0.0000
 2  4 101.9444    0.0000    0.0000   -0.2285   -0.3000    0.0000   36.0000    1.0271
        7.0832   -0.1532   19.8594    1.0000   -0.0836    4.7210    0.0000    0.0000
 3  4  88.0134  107.3137    0.0000    0.4680   -0.5000    1.0000   50.0000    2.0000
        7.5815   -0.4509    7.6953    1.0000   -0.0952    5.1424    1.0000    0.0000
 4  4  75.6824    0.0000    0.0000   -0.9934   -0.3000    0.0000   16.0000    0.2050
        2.2857   -0.3000   16.0000    1.0000   -0.1230    8.7005    0.0000    0.0000
 1  5  54.6610   -0.0200    0.0000   -0.8605   -0.5000    0.0000   35.0000    0.3953
        0.6908   -0.2500   11.9965    1.0000   -0.0668    9.0596    0.0000    0.0000
 2  5  59.2034    0.0000    0.0000    0.1240    0.0000    0.0000    6.0000    0.4000
        1.0000    0.0000   12.0000    1.0000   -0.0565    4.9575    0.0000    0.0000
 3  5 223.9629   10.0000    0.0000   -0.8805    0.0000    1.0000    6.0000    0.2178
        4.2326   -0.1048    7.0167    1.0000   -0.0867    4.2825    0.0000    0.0000
 4  5 100.0000    0.0000    0.0000   -3.1025    0.3000    0.0000   26.0000    2.0000
        3.2823    0.0000   12.0000    1.0000   -0.0800    6.9752    0.0000    0.0000
 5  5  34.3154    0.0000    0.0000    0.5995    0.3000    0.0000   26.0000    0.5445
```

```
        0.5752    0.0000   12.0000    1.0000   -0.1382    4.5000    0.0000    0.0000
2  6 233.4343    0.0000    0.0000   -0.4237   -0.3500    1.0000   25.0000    1.9689
        4.7870   -0.2500   15.0000    1.0000   -0.1288    4.9159    1.0000    0.0000
3  6 197.9420    0.0000    0.0000   -0.7552   -0.3500    1.0000   25.0000    0.2137
        9.5888   -0.2500   15.0000    1.0000   -0.1477    7.8947    1.0000    0.0000
4  6 182.8718   14.3332    0.0000   -0.3452    0.3022    1.0000    6.0000    0.3585
        2.6684   -0.1484   11.8165    1.0000   -0.0940    5.8491    0.0000    0.0000
6  6 124.4206    0.0000    0.0000   -1.0188   -0.3500    1.0000   25.0000    0.0863
        8.4257   -0.2500   15.0000    1.0000   -0.2337    8.1452    1.0000    0.0000
1  6 230.5926    0.0000    0.0000   -0.9278    0.0000    1.0000    6.0000    1.0927
        7.1644    1.0000    0.0000    1.0000   -0.0732    5.9745    0.0000    0.0000
5  6  92.6032    0.0000    0.0000   -0.5454   -0.5582    0.0000   44.9378    0.3238
        1.0563   -0.2500   15.0000    1.0000   -0.1206    4.0000    0.0000    0.0000
1  7 110.0000   92.0000    0.0000    0.2171   -0.1418    1.0000   13.1260    0.6000
        0.3601   -0.1310   10.7257    1.0000   -0.0869    5.3302    1.0000    0.0000
2  7   0.1466    0.0000    0.0000    0.2250   -0.1418    1.0000   13.1260    0.6000
        0.3912   -0.1310    0.0000    1.0000   -0.1029    9.3302    0.0000    0.0000
3  7 202.5868  164.1808    0.0000    0.5506   -0.5000    1.0000   25.0000    0.4300
        0.0912   -0.1285   16.0342    1.0000   -0.2008    6.2678    1.0000    0.0000
7  7   0.0000    0.0000    0.0000    0.2171   -0.5000    1.0000   35.0000    0.6000
        0.5000   -0.5000   20.0000    1.0000   -0.2000   10.0000    1.0000    0.0000
6  7 191.3390   10.2597    0.0000    0.9085   -0.5000    1.0000    0.0000    0.1616
        0.0940   -0.1039   10.0002    1.0000   -0.1073    9.9960    1.0000    0.0000
5  7   0.0000    0.0000    0.0000    0.5000   -0.2000    0.0000   16.0000    0.5000
        1.0001   -0.2000   15.0000    1.0000   -0.1000   10.0000    0.0000    0.0000
4  7   0.0000    0.0000    0.0000    0.5000   -0.2000    0.0000   16.0000    0.5000
        1.0001   -0.2000   15.0000    1.0000   -0.1000   10.0000    0.0000    0.0000
16      ! Nr of off-diagonal terms;  Ediss;Ro;gamma;rsigma;rpi;rpi2
 1  2   0.1239    1.4004    9.8467    1.1210   -1.0000   -1.0000
 2  3   0.0283    1.2885   10.9190    0.9215   -1.0000   -1.0000
 1  3   0.0503    1.8006   10.2114    1.3492    1.1992    1.0506
 1  4   0.0475    1.6810    8.8902    1.5153    1.0000   -1.0000
 2  4   0.1017    1.3259   12.5406    1.4534   -1.0000   -1.0000
 3  4   0.1121    2.0879   11.2110    1.5063    1.4795   -1.0000
 1  5   0.0270    2.4124   11.4640    1.7840    1.0000    1.0000
 2  5   0.1149    1.4658   11.0886    1.3337   -1.0000   -1.0000
 3  5   0.0687    1.8765   12.0451    1.2928   -1.0000   -1.0000
 4  5   7.1011    0.9961   40.6852    1.7459   -1.0000   -1.0000
 2  6   0.1087    1.8734    9.1166    1.0000   -1.0000   -1.0000
 3  6   0.1714    1.6576   10.7298    1.5553   -1.0000   -1.0000
 4  6   0.0837    1.9512   12.2762    1.4795   -1.0000   -1.0000
 5  6   0.1092    1.7165   10.1139    1.5274   -1.0000   -1.0000
 1  6   0.1485    1.3609   11.8373    1.3335    1.4000   -1.0000
 6  7   0.1435    1.0021    9.7624    1.7440   -1.0000   -1.0000
48      ! Nr of angles;at1;at2;at3;Thetao,o;ka;kb;pv1;pv2
 1  1  1  59.0573   30.7029    0.7606    0.0000    0.7180    6.2933    1.1244
 1  1  2  65.7758   14.5234    6.2481    0.0000    0.5665    0.0000    1.6255
 2  1  2  70.2607   25.2202    3.7312    0.0000    0.0050    0.0000    2.7500
 1  2  2   0.0000    0.0000    6.0000    0.0000    0.0000    0.0000    1.0400
 1  2  1   0.0000    3.4110    7.7350    0.0000    0.0000    0.0000    1.0400
 2  2  2   0.0000   27.9213    5.8635    0.0000    0.0000    0.0000    1.0400
 1  1  3  54.7427   21.1992    1.0613    0.0000    2.9950   58.6562    1.1232
 3  1  3  78.6632   16.3065    6.3613  -19.9300    1.5183    0.0000    2.2234
 2  1  3  50.0000   12.9103    2.5311    0.0000    0.1000    0.0000    1.0000
 1  3  1  71.6401   45.0000    1.2667    0.0000    2.8294    0.0000    1.0000
 1  3  3  76.3686   44.8665    1.9461    0.0000    1.0572   68.1072    1.8676
 3  3  3  89.9293   15.8855    2.0229    0.0000    2.9881    0.0000    1.0237
 1  3  2  90.0000    6.6459    5.2255    0.0000    1.3111    0.0000    3.0000
 2  3  3  75.6935   50.0000    2.0000    0.0000    1.0000    0.0000    1.1680
 2  3  2  85.8000    9.8453    2.2720    0.0000    2.8635    0.0000    1.5800
 1  2  3   0.0000   16.7302    1.1143    0.0000    0.0000    0.0000    1.0000
 3  2  3   0.0000   15.0000    2.8900    0.0000    0.0000    0.0000    2.8774
 2  2  3   0.0000    8.5744    3.0000    0.0000    0.0000    0.0000    1.0421
```

```
3   4   3    29.9309     3.6478     2.2492     0.0000     1.1980     0.0000     2.3810
4   3   4     3.3622    10.1592     2.3865     0.0000     3.2489     0.0000     2.6812
3   3   4    11.7872    50.0000     5.8383     0.0000     4.6977     0.0000     1.0000
3   4   4    15.3871     4.8803     8.3929     0.0000     4.1095     0.0000     3.4321
1   3   4    90.0000    11.8185     3.0517     0.0000     2.1225     0.0000     1.0000
2   5   2    25.9881     0.0100     1.8827     0.0000     0.6581     0.0000     1.1500
5   2   5     0.0000     3.6249     1.0000     0.0000     1.0000     0.0000     1.2500
3   5   3    10.0000     0.1000     1.0302     0.0000     1.0000     0.0000     1.0000
3   3   5   106.0264     7.0152     0.2086     0.0000     0.0100     0.0000     2.5367
1   3   5    92.0242     0.1000    10.0000     0.0000     2.8844     0.0000     1.1706
3   1   5   100.2536     0.0100     4.2329     0.0000     1.7872     0.0000     2.3488
5   3   5    70.3878     3.0984     2.8121     0.0000     0.9139     0.0000     1.9378
3   2   6     0.0000     1.8088     0.0100     0.0000     0.0000     0.0000     1.2229
2   6   2     0.0000     5.6384     1.3636     0.0000     0.4652     0.0000     1.0400
6   4   6    19.0109    16.8964    13.2508     0.0000    -0.3146     0.0000     1.3785
6   6   4    35.8369    25.7536     3.2681     0.0000     3.0259     0.0000     1.0179
3   4   6    23.3113    15.3421     1.7515     0.0000     2.0263     0.0000     1.3581
5   4   3    59.8446    13.2857     0.3263     0.0000     4.0719     0.0000     1.1745
2   4   3   284.7908    48.6239     1.6168     0.0000     7.3083     0.0000    14.6937
4   3   2    48.8774    12.4454     1.0604     0.0000     4.1897     0.0000     1.0077
5   3   2    52.6599    13.3819     1.0695     0.0000     4.3732     0.0000     1.0078
6   2   6    10.0000     7.7335     1.0000     0.0000     1.2806     0.0000     1.0400
2   6   6    10.0000    10.0000     3.8265     0.0000     1.0000     0.0000     1.0400
6   6   6    59.0573    30.7029     0.7606     0.0000     0.7180     6.2933     1.1244
2   2   6    10.0000     7.2139     3.7598     0.0000     1.0000     0.0000     1.7496
6   1   6    66.7242    16.7256     8.4462     0.0000     1.0455     0.0000     3.9255
6   1   2    70.0840    25.3540     3.4508     0.0000     1.0000     0.0000     3.0000
1   1   6    65.7758    14.5234     6.2481     0.0000     1.0000     0.0000     1.6255
1   6   6    10.0000     2.3487     6.0000     0.0000     5.0000     0.0000     1.0000
1   6   1    10.0000     3.4110     7.7350     0.0000     1.0000     0.0000     1.0400
32       ! Nr of torsions;at1;at2;at3;at4;;V1;V2;V3;V2(BO);vconj;n.u;n
1  1  1  1   -0.2500    34.7453     0.0288    -6.3507    -1.6000     0.0000     0.0000
1  1  1  2   -0.2500    29.2131     0.2945    -4.9581    -2.1802     0.0000     0.0000
2  1  1  2   -0.2500    31.2081     0.4539    -4.8923    -2.2677     0.0000     0.0000
1  1  1  3   -2.5000    25.4016     1.0000    -4.4850    -1.1000     0.0000     0.0000
2  1  1  3   -0.9763    59.4161     1.0000    -7.7414    -1.0978     0.0000     0.0000
3  1  1  3   -2.5000    52.7614    -1.0000    -4.0134    -0.8614     0.0000     0.0000
1  1  3  1   -1.9125    80.0000    -1.0000    -4.5626    -0.9000     0.0000     0.0000
1  1  3  2    0.6154     8.3019    -0.4870    -2.9336    -0.9000     0.0000     0.0000
2  1  3  1   -2.5000    80.0000     0.9658    -4.4935    -0.9000     0.0000     0.0000
2  1  3  2   -1.0000    31.8695     1.0000    -2.6151    -1.1000     0.0000     0.0000
1  1  3  3    0.7514    34.1941     0.5669    -5.5360    -2.0544     0.0000     0.0000
2  1  3  3    2.5000    80.0000     1.0000    -2.6841    -2.8274     0.0000     0.0000
3  1  3  1    0.2515    79.1495    -0.6263    -4.3647    -3.0437     0.0000     0.0000
3  1  3  2    1.0000    37.1243     1.0000    -2.5000    -3.0476     0.0000     0.0000
3  1  3  3   -1.0092    41.0504     0.3915    -6.0913    -2.7174     0.0000     0.0000
1  3  3  1   -1.6378   -11.8357     0.3815    -3.2104    -2.7536     0.0000     0.0000
1  3  3  2   -2.5000    -9.2805     0.3063    -5.9187    -2.9498     0.0000     0.0000
2  3  3  2    0.2732   -21.6925    -1.0000    -2.5000    -0.9921     0.0000     0.0000
1  3  3  3    2.5000   -17.6041     1.0000    -2.5000    -0.9972     0.0000     0.0000
2  3  3  3   -2.5000    78.0855    -0.8750    -7.8902    -1.2407     0.0000     0.0000
3  3  3  3   -2.5000   -25.0000     1.0000    -2.5000    -0.9000     0.0000     0.0000
0  1  2  0    0.0000     0.0000     0.0000     0.0000     0.0000     0.0000     0.0000
0  2  2  0    0.0000     0.0000     0.0000     0.0000     0.0000     0.0000     0.0000
0  2  3  0    0.0000     0.1000     0.0200    -2.5415     0.0000     0.0000     0.0000
0  1  1  0    0.0000    50.0000     0.3000    -4.0000    -2.0000     0.0000     0.0000
0  3  3  0    0.5511    25.4150     1.1330    -5.1903    -1.0000     0.0000     0.0000
0  1  6  0    3.3423    30.3435     0.0365    -2.7171     0.0000     0.0000     0.0000
0  6  6  0   -0.0500    10.0000     0.1565    -2.2006     0.0000     0.0000     0.0000
0  2  6  0    0.0000     0.0000     0.0000     0.0000     0.0000     0.0000     0.0000
1  1  1  6   -0.2500    29.2131     0.2945    -4.9581    -2.1802     0.0000     0.0000
6  1  1  6   -0.2500    31.2081     0.4539    -4.8923    -2.2677     0.0000     0.0000
6  6  6  6   -0.2500    34.7453     0.0288    -6.3507    -1.6000     0.0000     0.0000
```

94

```
1    ! Nr of hydrogen bonds;at1;at2;at3;Rhb;Dehb;vhb1
3  2  3   2.1200  -3.5800   1.4500  19.5000
```

APPENDIX B: LAMMPS SAMPLE INPUT CODE

```
#initializing

log             log.LiSEI
units           real
boundary        p p p
atom_style      full
timestep        0.2

read_data       readdata
velocity         all create 10 12572

pair_style       reax
pair_coeff       * * ffield.reax 1 2 3 5 4 6 7 8 9

group           cath molecule 9
group           elect molecule 1 2 4
group           Li type 4
group           EC molecule 1
group           DMC molecule 2
group           salt molecule 3 4
group           Mn type 5

thermo           100
thermo_style     custom step temp pe ke etotal press vol

neighbor 2 bin
neigh_modify every 1 delay 0 check no one 10000

minimize        1.0e-8 1.0e-8 10000 10000
#-----------------------------------------------------------------------

#Heating

dump            1 all custom 10000 dump.nvt20ps id mol type q x y z
dump_modify     1 sort id

fix             1 all nvt temp 10 330 100

run              100000
```

```
write_restart     restart_LiSEI_20ps
#------------------------------------------------------------------------

#Equilibration

restart           50000  restart.LiSEI.mpiio
undump            1
unfix             1

fix               2 all nvt temp 330 330 100


dump              3 all custom 10000 dump.nvtequi.* id mol type q x y z
dump_modify       3 sort id
run               500000
write_restart     restart_LiSEI_nvt120ps
undump            3
#------------------------------------------------------------------------

#Production

#Compute MSD

compute           saltmsd salt msd com yes
fix               saltmsd salt ave/time 5000 100 500000 c_saltmsd file
salt.msd mode vector

compute           ECmsd EC msd com yes
fix               ECmsd EC ave/time 5000 100 500000 c_ECmsd file EC.msd
mode vector

compute           DMCmsd DMC msd com yes
fix               DMCmsd DMC ave/time 5000 100 500000 c_DMCmsd file
DMC.msd mode vector

compute           Mnmsd Mn msd com yes
fix               Mnmsd Mn ave/time 5000 100 500000 c_Mnmsd file Mn.msd
mode vector

compute           Limsd Li msd com yes
fix               Limsd Li ave/time 5000 100 500000 c_Limsd file Li.msd
mode vector

#Compute RDF

#RDF between Li and all O

compute           LiOrdf all rdf 200 4 3
```

```
fix             LiOrdf all ave/time 5000 100 500000 c_LiOrdf file
LiO.rdf mode vector

#RDF between Mn and all O

compute         MnOrdf all rdf 200 4 3
fix             MnOrdf all ave/time 5000 100 500000 c_MnOrdf file
MnO.rdf mode vector

dump            4 all custom 10000 dump.nvtprod.* id mol type q x y z
dump_modify     4 sort id
run              5000000 upto
write_restart    restart_LiSEI_nvt1ns
```

APPENDIX C: PACKMOL INPUT CODE

```
# A mixture of EC/DMC (3:7), FEC 5%, LiPF₆ 1M

# All the atoms from different molecules will be separated at least 2.5
# Angstroms at the solution.

tolerance 2.5
seed 235

# The file type of input and output files is xyz

filetype xyz

# The name of the output file

output electout.xyz

structure DMC.xyz
  number 240
  inside box 0. 0. 0. 33. 33. 33.
end structure

structure EC.xyz
  number 104
  inside box 0. 0. 0. 33. 33. 33.
end structure

#structure FEC.xyz
#  number 18
#  inside box 0. 0. 0. 33. 33. 33.
#end structure

structure LiPF6.xyz
  number 26
  inside box 0. 0. 0. 33. 33. 33.
end structure
```

BIBLIOGRAPHY

1.   Vetter, J. *et al.* Ageing mechanisms in lithium-ion batteries. *J. Power Sources* **147,** 269–281 (2005).

2.   Gaines, L. & Cuenca, R. *Costs of Lithium-Ion Batteries for Vehicles*. (2000).

3.   Stephenson, D. E. Microstructure and Transport Propertues of Porous Li-ion electrodes. (Brigham Young University, 2011).

4.   Fergus, J. W. Recent developments in cathode materials for lithium ion batteries. *J. Power Sources* **195,** 939–954 (2010).

5.   Daniel, C. Materials and Processing for Lithium ion Batteries. *J. Met.* **60,** (2008).

6.   Sahan, H., Goktepe, H. & Patat, S. A Novel Method to Improve the Electrochemical Performance of LiMn2O4 Cathode Active Material by CaCO3 Surface Coating. *J. Mater. Sci. Technol.* **27,** 415–420 (2011).

7.   Rodriguez-Carvajal, J., Rousse, G., Masquelier, C. & Hervieu, M. Electronic Crystallization in a Lithium Battery Material: Columnar Ordering of Electrons and Holes in the Spinel LiMn2O4. *Phys. Rev. Lett.* **81,** 21–24 (1998).

8.   Chen, C. ., Liu, J. & Amine, K. Symmetric cell approach and impedance spectroscopy of high power lithium-ion batteries. *J. Power Sources* **96,** 321–328 (2001).

9.   Balbuena, P. B. *Lithium-Ion Batteries: Solid-Electrolyte Interphase*. (Imperial College Press, 2004).

10.   Doh, C., Lee, J., Lee, D., Jin, B. & Moon, S. The Quantitative Analyses of the Dissolved Manganese in the Electrolyte of Li/LiMn2O4 Cell Using by Ion Chromatography. *Bull. Korean Chem. Soc.* **30,** 4–7 (2009).

11.   Edstrom, K., Herstedt, M. & Abraham, D. P. A new look at the SEI at the graphite electrolyte interphase in Li ion batteries.pdf. *J. Power Sources* **153,** 380–384 (2006).

12.   Friesner, R. a. Ab initio quantum chemistry: methodology and applications. *Proc. Natl. Acad. Sci. U. S. A.* **102,** 6648–53 (2005).

13.   Cramer, C. J. & Truhlar, D. G. Density functional theory for transition metals and transition metal chemistry. *Phys. Chem. Chem. Phys.* **11,** 10757–816 (2009).

14.   Cuevas, J. C. & Scheer, E. *Molecular electronics: An introduction to theory and experiment*. (World Scientific Publication Company, 2010).

15.   Sholl, D. S. & Steckel, J. A. *Density Functional Theory: A Practical Introduction*.

(Wiley, 2009).

16. Allen, M. P. Introduction to Molecular Dynamics Simulation. **23,** (2004).

17. Aktulga, H. M., Pandit, S. A., Duin, A. C. T. V. A. N. & Grama, A. Y. Reactive molecular dynamics: numerical methods and algorithmic techniques. **33620,** 1–29

18. Mayo, S. L., Olafson, B. D. & Goddard III, W. A. DREIDING: A Generic Force Field for Molecular Simulations. *J. Phys. Chem.* **94,** 8897–8909 (1990).

19. Rappe, A. K., Casewit, C. ., Colwell, K. ., Goddard, W. A. & Skiff, W. . UFF, a full periodic table force field for Molecular Mechanics and Molecular dynamic simulations. *J. Am. Chem. Soc.* **114,** 10024–10035 (1992).

20. Cornell, W. D. *et al.* A Second Generation Force Field for the Simulation of Proteins, Nucleic Acids, and Organic Molecules. *J. Am. Chem. Soc.* **117,** 5179–5197 (1995).

21. Brooks, B. R. *et al.* CHARMM: A program for macromolecular energy, minimization, and dynamics calculations. *J. Comput. Chem.* **4,** 187–217 (1983).

22. Melker, A. I. Potentials of interatomis interaction in molecular dynamics. *Rev. Adv. Mater. Sci.* **20,** 1–13 (2009).

23. González, M. A. Force fields and molecular dynamics simulations. *Collect. SFN* **12,** 169–200 (2011).

24. Halgren, T. A. & Damm, W. Polarizable force fields. *Curr. Opin. Struct. Biol.* **11,** 236–42 (2001).

25. Halgren, T. A. & Damm, W. Polarizable Force Fields. *Curr. Opin. Struct. Biol.* **11,** 236–242 (2001).

26. Tersoff, J. New empirical approach for the structure and energy of covalent systems. *Phys. Rev. B* **37,** (1988).

27. Brenner, D. W. *et al.* A second-generation reactive empirical bond order (REBO) potential energy expression for hydrocarbons. *J. Phys. Condens. Matter* **14,** 783–802 (2002).

28. Stuart, S. J., Tutein, A. B. & Harrison, J. a. A reactive potential for hydrocarbons with intermolecular interactions. *J. Chem. Phys.* **112,** 6472 (2000).

29. van Duin, A. C. T., Dasgupta, S., Lorant, F. & Goddard, W. a. ReaxFF: A Reactive Force Field for Hydrocarbons. *J. Phys. Chem. A* **105,** 9396–9409 (2001).

30. van Duin, A. *ReaxFF User Manual*. (2002).

31. Nielson, K. D., van Duin, A. C. T., Oxgaard, J., Deng, W.-Q. & Goddard, W. a. Development of the ReaxFF reactive force field for describing transition metal catalyzed reactions, with application to the initial stages of the catalytic formation of carbon nanotubes. *J. Phys. Chem. A* **109,** 493–9 (2005).

32. Rom, N. *et al.* Density dependent liquid Nitromethane decomposition: MD simulations based on ReaxFF. *J. Phys. Chem. A* 10181–10202 (2011). doi:10.1021/jp202059v

33. Raju, M., Kim, S., Duin, A. C. T. Van & Fichthorn, K. A. ReaxFF Reactive Force Field Study of the Dissociation of Water on Titania Surfaces. *J. Phys. Chem. C*

(2013).

34.   Schönfelder, T. Reactive Force Fields in Particular ReaxFF and Application Possibilities. (2010).

35.   van Duin, A. C. T., Dasgupta, S., Lorant, F. & Goddard, W. a. ReaxFF: A Reactive Force Field for Hydrocarbons. *J. Phys. Chem. A* **105,** 9396–9409 (2001).

36.   Chenoweth, K. *et al.* Development and Application of a ReaxFF Reactive Force Field for Oxidative Dehydrogenation on Vanadium Oxide Catalysts. *J. Phys. Chem. C* **112,** 14645–14654 (2008).

37.   Chenoweth, K., van Duin, A. C. T. & Goddard, W. a. ReaxFF reactive force field for molecular dynamics simulations of hydrocarbon oxidation. *J. Phys. Chem. A* **112,** 1040–53 (2008).

38.   Järvi, T. T. *et al.* Development of a ReaxFF description for gold. *Eur. Phys. J. B* **66,** 75–79 (2008).

39.   Bedrov, D., Smith, G. D. & van Duin, A. C. T. Reactions of singly-reduced ethylene carbonate in lithium battery electrolytes: A molecular dynamics simulation study using the ReaxFF. *J. Phys. Chem. A* **116,** 2978–85 (2012).

40.   Han, S. S., van Duin, A. C. T., Goddard, W. a & Lee, H. M. Optimization and application of lithium parameters for the reactive force field, ReaxFF. *J. Phys. Chem. A* **109,** 4575–82 (2005).

41.   Aravindan, V., Gnanaraj, J., Madhavi, S. & Liu, H. K. Lithium-ion conducting electrolyte salts for lithium batteries. *Chem. - A Eur. J.* **17,** 14326–14346 (2011).

42.   Segall, M. D. *et al.* First-principles simulation : ideas , illustrations and the CASTEP code. *J. Phys. Condens. Matter* **14,** 2717–2744 (2002).

43.   Delley, B. From molecules to solids with the DMol3 approach. *J. Chem. Phys.* **113,** 7756 (2000).

44.   Inada, Y. & Orita, H. Efficiency of numerical basis sets for predicting the binding energies of hydrogen bonded complexes: evidence of small basis set superposition error compared to Gaussian basis sets. *J. Comput. Chem.* **29,** 225–232 (2008).

45.   van Duin, A. C. T., Baas, J. M. A. & van de Graaf, B. Delft Molecular Mechanics : A New Approach to Hydrocarbon Force. *J. Chem. Soc. Faraday Transform.* **90,** 2881–2895 (1994).

46.   Desai, P. . D. Thermodynamic Properties of Manganese and Molybdenum. *J. Phys. Chem. Ref. Data* **16,** 91–108 (1987).

47.   Oberteuffer, J. a. & Ibers, J. a. A refinement of the atomic and thermal parameters of α-manganese from a single crystal. *Acta Crystallogr. Sect. B Struct. Crystallogr. Cryst. Chem.* **26,** 1499–1504 (1970).

48.   Hobbs, D. & Hafner, J. Ab initio density functional study of phase stability and noncollinear magnetism in Mn. *J. Phys. Condens. Matter* **13,** L681–L688 (2001).

49.   Hortamani, M., Kratzer, P. & Scheffler, M. Density-functional study of Mn monosilicide on the Si(111) surface: Film formation versus island nucleation. *Phys. Rev. B* **76,** 235426 (2007).

50.   Jacob, K. T., A.Kumar, G.Rajitha & Waseda, Y. Thermodynamic Data for Mn3O4

, Mn2O3 and MnO2. *High Temp. Mater. Proc.* **30,** 459–472 (2011).

51. Julien, C. M. & Massot, M. Lattice vibrations of materials for lithium rechargeable batteries I. Lithium manganese oxide spinel. *Mater. Sci. Eng. B* **97,** 217–230 (2003).

52. Darwent, B. *Bond dissociation energies in simple molecules*. (1986).

53. Zhou, M. *et al.* Reactions of Mn with H2O and MnO with H2 . Matrix-Isolation FTIR and Quantum Chemical Studies. *J. Phys. Chem. A* **105,** 5801–5807 (2001).

54. Kalemos, A. & Dunning, T. H. Ab initio study of the electronic structure of manganese carbide. **154308,** 1–6 (2006).

55. Stout, J. . & Reed, S. . in *Crystal Structure of Anhydrous Fluorides* (1954).

56. Chase, M. *NIST-JANAF Thermochemical Tables*. *Journal of Physical and Chemical Reference Data, Monograph 9* (1998). doi:citeulike-article-id:12140840

57. Ehlert, T. C. & Hsia, M. Mass spectrometric and thermochemical studies of the manganese fluorides. *J. Fluor. Chem.* **2,** 33–51 (1972).

58. Brandes, E. A. & Brook, G. B. *Smithells Metals reference book*. (1992).

59. Chandra, A. K. & Uchimaru, T. A DFT Study on the C-H Bond Dissociation Enthalpies of Haloalkanes : Correlation between the Bond Dissociation Enthalpies and Activation Energies for Hydrogen Abstraction. *J. Phys. Chem. A* **104,** 9244–9249 (2000).

60. Zunger, A. Band structure, crystal conformation, and hydrogen bond potentials for solid HF. *J. Chem. Phys.* **63,** 1713 (1975).

61. Barrett, C. . & Meyer, L. Molecular Packing defects and transformations in Solid Oxygen. *Phys. Rev.* **160,** 694–697 (1967).

62. Post, J. E. Manganese oxide minerals: Crystal structures and economic and environmental significance. *Proc. Natl. Acad. Sci.* **96,** 3447 (1999).

63. Sidheswaran, M. a., Destaillats, H., Sullivan, D. P., Larsen, J. & Fisk, W. J. Quantitative room-temperature mineralization of airborne formaldehyde using manganese oxide catalysts. *Appl. Catal. B Environ.* **107,** 34–41 (2011).

64. Álvarez-Galván, M. C., Pawelec, B., de la Peña O'Shea, V. a., Fierro, J. L. G. & Arias, P. L. Formaldehyde/methanol combustion on alumina-supported manganese-palladium oxide catalyst. *Appl. Catal. B Environ.* **51,** 83–91 (2004).

65. Luo, Y. *et al.* Probing the Surface Structure of αMn2O3 Nanocrystals during CO Oxidation by Operando Raman Spectroscopy. *J. Phys. Chem. C* (2012).

66. Hu, J., Chu, W. & Shi, L. Effects of carrier and Mn loading on supported manganese oxide catalysts for catalytic combustion of methane. *J. Nat. Gas Chem.* **17,** 159–164 (2008).

67. Brooks, C. S. The Kinetics of Hydrogen and Carbon Monoxide Oxidation over a Manganese Oxide. *J. Catal.* **8,** 272–282 (1967).

68. Najafpour, M. M. *et al.* Manganese Compounds as Water-Oxidizing Catalysts: From the Natural Water-Oxidizing Complex to Nanosized Manganese Oxide Structures. *Chem. Rev.* (2016). doi:10.1021/acs.chemrev.5b00340

69. Chang, Y. & McCarty, J. G. Novel oxygen storage components for advanced catalysts for emission control in natural gas fueled vehicles. *Catal. Today* **30,** 163–170 (1996).

70. Ottone, C. *et al.* Effect of surface area on the rate of photocatalytic water oxidation as promoted by different manganese oxides. *Chem. Eng. J.* **278,** 36–45 (2015).

71. Xu, J. *et al.* Operando Raman spectroscopy and kinetic study of low-temperature CO oxidation on an α-Mn2O3 nanocatalyst. *J. Catal.* **300,** 225–234 (2013).

72. Zou, Z., Meng, M. & Zha, Y. Surfactant-Assisted Synthesis , Characterizations , and Catalytic Oxidation Mechanisms of the Mesoporous MnOx-CeO2 and Pd/MnOx-CeO2 Catalysts Used for CO and C3H8 Oxidation. *J. Phys. Chem. C* **114,** 468–477 (2010).

73. Kapteijn, F., Singoredjo, L., Andreini, A. & Moulijn, J. A. Activity and selectivity of pure manganese oxides in the selective catalytic reduction of nitric oxide with ammonia. *Appl. Catal. B Environ.* **3,** 173–189 (1994).

74. Grisel, R. J. H. & Nieuwenhuys, B. E. A comparative study of the oxidation of CO and CH4 over Au/MOx/Al2O3 catalysts. *Catal. Today* **64,** 69–81 (2001).

75. Bjo, E. & Ja, S. Total oxidation catalysts based on manganese or copper oxides and platinum or palladium II : Activity , hydrothermal stability and sulphur resistance. *Appl. Catal. A Gen.* **180,** 153–161 (1999).

76. Adanez, J., Abad, A., Garcia-Labiano, F., Gayan, P. & De Diego, L. F. Progress in chemical-looping combustion and reforming technologies. *Prog. Energy Combust. Sci.* **38,** 215–282 (2012).

77. Boreskov, G. K. The Catalysis of Isotopic Exchange in Molecular Oxygen. *Adv. Catal.* **15,** 285–339 (1965).

78. Roux, S., Bensakhria, A. & Antonini, G. Study and improvement of the regeneration of metallic oxides used as oxygen carriers for a new combustion process. *Int. J. Chem. React. Eng.* **4,** 1–14 (2006).

79. Cho, P., Mattisson, T. & Lyngfelt, A. Comparison of iron-, nickel-, copper- and manganese-based oxygen carriers for chemical-looping combustion. *Fuel* **83,** 1215–1225 (2004).

80. Lin, L. & Bai, H. Promotional effects of manganese on the structure and activity of Ce – Al – Si based catalysts for low-temperature oxidation of acetone. *Chem. Eng. J.* **291,** 94–105 (2016).

81. Royer, S., Alamdari, H., Duprez, D. & Kaliaguine, S. Oxygen storage capacity of La(1-x)A ' xBO3 perovskites (with A ' = Sr, Ce; B=Co, Mn)-relation with catalytic activity in the CH4 oxidation reaction. *Appl. Catal. B-Environmental* **58,** 273–288 (2005).

82. Jia, L., Shen, M., Hao, J., Rao, T. & Wang, J. Dynamic oxygen storage and release over Mn0.1Ce0.9Ox and Mn0.1Ce0.6Zr0.3Ox complex compounds and structural characterization. *J. Alloys Compd.* **454,** 321–326 (2008).

83. Adanez, J. *et al.* Selection of Oxygen Carriers for Chemical-Looping Combustion S. *Energy & Fuels* **18,** 371–377 (2004).

84. Mattisson, T., Jardans, A., Lyngfelt, A. & Ja, A. Reactivity of Some Metal Oxides Supported on Alumina with Alternating Methane and OxygenApplication for Chemical-Looping Combustion Reactivity of Some Metal Oxides Supported on Alumina with Alternating Methane and OxygensApplication for Chemical-Looping C. *Energy & Fuels* 643–651 (2003). doi:10.1021/ef020151i

85. Zhang, L. *et al.* Manganese dioxide as an alternative cathodic catalyst to platinum in microbial fuel cells. *Biosens. Bioelectron.* **24,** 2825–9 (2009).

86. Density, H., Theory, F. & Methods, C. C. C. EHF Theory of Chemical Reactions V . Nature of Manganese – Oxygen Bonds by. **85,** 34–43 (2001).

87. Fang, D., He, F., Li, D. & Xie, J. First principles and experimental study of NH3 adsorptions on MnOx surface. *Appl. Surf. Sci.* **285,** 215–219 (2013).

88. Li, W., Gibbs, G. V & Oyama, S. T. Mechanism of Ozone Decomposition on a Manganese Oxide Catalyst. 1. In Situ Raman Spectroscopy and Ab Initio Molecular Orbital Calculations. *J. Am. Chem. Soc.* **120,** 9041–9046 (1998).

89. Plimpton, S. Fast Parallel Algorithms for Short – Range Molecular Dynamics. *J. Comput. Phys.* **117,** 1–42 (1995).

90. Zafar, Q., Abad, A., Mattisson, T., Gevert, B. & Strand, M. Reduction and oxidation kinetics of Mn3O4/Mg–ZrO2 oxygen carrier particles for chemical-looping combustion. *Chem. Eng. Sci.* **62,** 6556–6567 (2007).

91. Abad, a, Mattisson, T., Lyngfelt, a & Ryden, M. Chemical-looping combustion in a 300W continuously operating reactor system using a manganese-based oxygen carrier. *Fuel* **85,** 1174–1185 (2006).

92. Pour, N. M., Azimi, G., Leion, H., Ryden, M. & Lyngfelt, A. Production and Examination of Oxygen-Carrier Materials Based on Manganese Ores and Ca (OH)2 in Chemical Looping with Oxygen Uncoupling. *Sep. Mater. Devices Process* **60,** 645–656 (2014).

93. Arjmand, M., Leion, H., Mattisson, T. & Lyngfelt, A. Investigation of different manganese ores as oxygen carriers in chemical-looping combustion (CLC) for solid fuels. *Appl. Energy* **113,** 1883–1894 (2014).

94. Johansson, M., Mattisson, T. & Lyngfelt, a. Investigation of Mn3O4 With Stabilized ZrO2 for Chemical-Looping Combustion. *Chem. Eng. Res. Des.* **84,** 807–818 (2006).

95. Mattisson, T. Materials for Chemical-Looping with Oxygen Uncoupling. *ISRN Chem. Eng.* **2013,** 1–19 (2013).

96. Sekine, Y. Oxidative decomposition of formaldehyde by metal oxides at room temperature. *Atmos. Environ.* **36,** 5543–5547 (2002).

97. Lee, J. H. & Trimm, D. L. Catalytic combustion of methane. *Fuel Process. Technol.* **42,** 339–359 (1995).

98. Craciun, R., Nentwick, B., Hadjiivanov, K. & Knözinger, H. Structure and redox properties of MnOx/Yttrium-stabilized zirconia (YSZ) catalyst and its used in CO and CH4 oxidation. *Appl. Catal. A Gen.* **243,** 67–79 (2003).

99. Mishra, S. & Ceder, G. Structural stability of lithium manganese oxides. *Phys.*

Rev. B **59,** 6120–6130 (1999).

100. Patoux, S. *et al.* High voltage nickel manganese spinel oxides for Li-ion batteries. *Electrochim. Acta* **53,** 4137–4145 (2008).

101. Verma, P., Maire, P. & Novák, P. A review of the features and analyses of the solid electrolyte interphase in Li-ion batteries. *Electrochim. Acta* **55,** 6332–6341 (2010).

102. *Lithium-Ion Batteries: Solid-Electrolyte Interphase*. (2004).

103. Xu, C. *et al.* Improved performance of the silicon anode for li-ion batteries: Understanding the surface modification mechanism of fluoroethylene carbonate as an effective electrolyte additive. *Chem. Mater.* **27,** 2591–2599 (2015).

104. Etacheri, V. *et al.* Effect of fluoroethylene carbonate (FEC) on the performance and surface chemistry of Si-nanowire li-ion battery anodes. *Langmuir* **28,** 965–976 (2012).

105. Bordes, A., Eom, K. & Fuller, T. F. The effect of fluoroethylene carbonate additive content on the formation of the solid-electrolyte interphase and capacity fade of Li-ion full-cell employing nano Si-graphene composite anodes. *J. Power Sources* **257,** 163–169 (2014).

106. Profatilova, I. A., Kim, S. S. & Choi, N. S. Enhanced thermal properties of the solid electrolyte interphase formed on graphite in an electrolyte with fluoroethylene carbonate. *Electrochim. Acta* **54,** 4445–4450 (2009).

107. Leung, K. *et al.* Modeling Electrochemical Decomposition of Fluoroethylene Carbonate on Silicon Anode Surfaces in Lithium Ion Batteries. *J. Electrochem. Soc.* **161,** A213–A221 (2014).

108. Mogi, R., Inaba, M., Iriyama, Y., Abe, T. & Ogumi, Z. Study of the decomposition of propylene carbonate on lithium metal surface by pyrolysis-gas chromatography-mass spectroscopy. *Langmuir* **19,** 814–821 (2003).

109. Nguyen, C. C. & Lucht, B. L. Comparative Study of Fluoroethylene Carbonate and Vinylene Carbonate for Silicon Anodes in Lithium Ion Batteries. *J. Electrochem. Soc.* **161,** 1933–1938 (2014).

110. Aoshima, T., Okahara, K., Kiyohara, C. & Shizuka, K. Mechanisms of manganese spinels dissolution and capacity fade at high temperature. *J. Power Sources* **97-98,** 377–380 (2001).

111. Komaba, S., Kumagai, N. & Kataoka, Y. Influence of manganese(II), cobalt(II), and nickel(II) additives in electrolyte on performance of graphite anode for lithium-ion batteries. *Electrochim. Acta* **47,** 1229–1239 (2002).

112. Amine, K. *et al.* Improved lithium manganese oxide spinel/graphite Li-ion cells for high-power applications. *J. Power Sources* **129,** 14–19 (2004).

113. Gowda, S. R. *et al.* Oxidation state of cross-over manganese species on the graphite electrode of lithium-ion cells. *Phys. Chem. Chem. Phys.* **16,** 6898–902 (2014).

114. Zhan, C. *et al.* Mn(II) deposition on anodes and its effects on capacity fade in spinel lithium manganate-carbon systems. *Nat. Commun.* **4,** 2437 (2013).

106

115. Delacourt, C. *et al.* Effect of Manganese Contamination on the Solid-Electrolyte-Interphase Properties in Li-Ion Batteries. *J. Electrochem. Soc.* **160,** A1099–A1107 (2013).

116. Xiao, X., Ahn, D., Liu, Z., Kim, J. H. & Lu, P. Atomic layer coating to mitigate capacity fading associated with manganese dissolution in lithium ion batteries. *Electrochem. commun.* **32,** 31–34 (2013).

117. Borodin, O. & Smith, G. D. Quantum chemistry and molecular dynamics simulation study of dimethyl carbonate: ethylene carbonate electrolytes doped with LiPF6. *J. Phys. Chem. B* **113,** 1763–76 (2009).

118. L. Martinez, Andrade, R., Birgin, E. G. & Martinez, J. M. PACKMOL: A package for building initial configurations for molecular dynamics simulations. *J. Comput. Chem.* **30,** 2157–2164 (2009).

119. Kim, S.-P., Duin, A. C. T. Van & Shenoy, V. B. Effect of electrolytes on the structure and evolution of the solid electrolyte interphase (SEI) in Li-ion batteries: A molecular dynamics study. *J. Power Sources* **196,** 8590–8597 (2011).

120. An, S. J. *et al.* The State of Understanding of the Lithium-Ion-Battery Graphite Solid Electrolyte Interphase (SEI) and Its Relationship to Formation Cycling. *Carbon N. Y.* **105,** 52–76 (2016).

121. Wang, Y., Nakamura, S., Ue, M. & Balbuena, P. B. Theoretical studies to understand surface chemistry on carbon anodes for lithium-ion batteries: reduction mechanisms of ethylene carbonate. *J. Am. Chem. Soc.* **123,** 11708–18 (2001).

122. Leung, K. & Budzien, J. L. Ab initio molecular dynamics simulations of the initial stages of solid – electrolyte interphase formation on lithium ion battery graphitic anodesw. *Phys. Chem. Chem. Phys.* **12,** 6583–6586 (2010).

123. Schroder, K. *et al.* The Effect of Fluoroethylene Carbonate as an Additive on the Solid Electrolyte Interphase on Silicon Lithium-Ion Electrodes. *Chem. Mater.* **27,** 5531–5542 (2015).

124. Nie, M., Abraham, D. P., Chen, Y., Bose, A. & Lucht, B. L. Silicon Solid Electrolyte Interphase (SEI) of Lithium Ion Battery Characterized by Microscopy and Spectroscopy Silicon solid electrolyte interphase (SEI) of lithium ion battery characterized by microscopy and spectroscopy. *J. Phys. Chem. C* **117,** 13403–13412 (2013).

125. Ma, Y. & Balbuena, P. B. DFT Study of Reduction Mechanisms of Ethylene Carbonate and Fluoroethylene Carbonate on Li+-Adsorbed Si Clusters. *J. Electrochem. Soc.* **161,** E3097–E3109 (2014).

126. Nakai, H., Kubota, T., Kita, A. & Kawashima, A. Investigation of the Solid Electrolyte Interphase Formed by Fluoroethylene Carbonate on Si Electrodes. *J. Electrochem. Soc.* **158,** A798 (2011).

127. Lemordant, D. *et al.* in *Advanced Fluoride-Based Materials for Energy Conversion* 173–202 (Elsevier, 2015). doi:10.1016/B978-0-12-800679-5.00008-7

128. Ochida, M. *et al.* Effects of Electrolyte Additives on the Suppression of Mn Deposition on the Edge Plane of HOPG for Lithium-ion Battery. in *Honolulu Prime The electrochemical Society* 759 (2012).

129. Shkrob, I. a. *et al.* Manganese in Graphite Anode and Capacity Fade in Li Ion Batteries. *J. Phys. Chem. C* **118,** 24335–24348 (2014).

130. Shin, H., Park, J., Sastry, A. M. & Lu, W. Degradation of the solid electrolyte interphase induced by the deposition of manganese ions. *J. Power Sources* **284,** 416–427 (2015).

131. Xiao, X. *et al.* Unraveling manganese dissolution/deposition mechanisms on the negative electrode in lithium ion batteries. *Phys. Chem. Chem. Phys.* **16,** 10398–402 (2014).

132. Scrosati, B. & Garche, J. Lithium batteries: Status, prospects and future. *J. Power Sources* **195,** 2419–2430 (2010).

133. Dunn, B., Kamath, H. & Tarascon, J.-M. Electrical Energy Storage for the Grid: A Battery of Choices. *Science (80-.).* **334,** 928–935 (2011).

134. Desilvestro, J. & Haas, O. Metal Oxide Cathode Materials for Electrochemical Energy Storage: A Review. *J. Electrochem. Soc.* **137,** (1976).

135. Amine, K. *et al.* Factors responsible for impedance rise in high power lithium ion batteries. *J. Power Sources* **97-98,** 684–687 (2001).

136. Xu, B., Fell, C. R., Chi, M. & Meng, Y. S. Identifying surface structural changes in layered Li-excess nickel manganese oxides in high voltage lithium ion batteries: A joint experimental and theoretical study. *Energy Environ. Sci.* **4,** 2223 (2011).

137. Edström, K., Gustafsson, T. & Thomas, J. O. The cathode–electrolyte interface in the Li-ion battery. *Electrochim. Acta* **50,** 397–403 (2004).

138. Yang, L., Ravdel, B. & Lucht, B. L. Electrolyte Reactions with the Surface of High Voltage LiNi0.5Mn1.5O4 Cathodes for Lithium-Ion Batteries. *Electrochem. Solid-State Lett.* **13,** A95 (2010).

139. Edstrom, K. *et al.* The cathode–electrolyte interface in the Li-ion battery. *Electrochim. Acta* **50,** 397–403 (2004).

140. Demeaux, J., Caillon-Caravanier, M., Galiano, H., Lemordant, D. & Claude-Montigny, B. LiNi0.4Mn1.6O4/Electrolyte and Carbon Black/Electrolyte High Voltage Interfaces: To evidence the chemical and ELectronic Contributions of the Solvent on the Cathode-Electrolyte Interface Formation. *Electrochem. Soc. Soc. Trans.* **41,** 65–78 (2012).

141. Gulbinska, M. K. *Catalytic Materials and Processes in Secondary Lithium-ion Batteries. New and Future Developments in Catalysis* (Elsevier B.V., 2013). doi:10.1016/B978-0-444-53880-2.00022-3

142. Jow, R. T., Xu, K., Borodin, O. & Ue, M. *Electrolytes for Lithium and Lithium-Ion Batteries.* (2014). doi:10.1039/c3ta14290f

143. Amine, K., Tukamoto, H., Yasuda, H. & Fujita, Y. Preparation and electrochemical investigation of LiMn2−xMexO4 (Me: Ni, Fe, and x = 0.5, 1) cathode materials for secondary lithium batteries. *J. Power Sources* **68,** 604–608 (1997).

144. Banov, B., Todorov, Y., Trifonova, A., Momchilov, A. & Manev, V. LiMnCoO4 Cathode With Enhanced Cycleability. *J. Power Sources* **68,** 578–581 (1997).

145. Gummow, R. J., de Kock, A. & Thackeray, M. M. Improved capacity retention in rechargeable 4 V lithium/lithium-manganese oxide (spinel) cells. *Solid State Ionics* **69,** 59–67 (1994).

146. Myung, S. T., Komaba, S. & Kumagai, N. Enhanced Structural Stability and Cyclability of Al-Doped LiMn2O4 Spinel Synthesized by the Emulsion Drying Method. *J. Electrochem. Soc.* **148,** 482–489 (2001).

147. Bhaskar, A. *et al.* 3d-Transition metal doped spinels as high-voltage cathode materials for rechargeable lithium-ion batteries. *Prog. Solid State Chem.* **42,** 128–148 (2014).

148. Chen, Z., Qin, Y. & Amine, K. Role of surface coating on cathode materials for lithium-ion batteries. *J. Mater. Chem.* **20,** 7606–7612 (2010).

149. Li, C. *et al.* Cathode materials modified by surface coating for lithium ion batteries. *Electrochim. Acta* **51,** 3872–3883 (2006).

150. Wu, H.-C., Su, C.-Y., Shieh, D.-T., Yang, M.-H. & Wu, N.-L. Enhanced High-Temperature Cycle Life of LiFePO4 Based Li-Ion Batteries by Vinylene Carbonate as Electrolyte Additive. *Electrochem. Solid-State Lett.* **9,** A537 (2006).

151. Eom, J. Y., Jung, I. H. & Lee, J. H. Effects of vinylene carbonate on high temperature storage of high voltage Li-ion batteries. *J. Power Sources* **196,** 9810–9814 (2011).

152. Ogawa, T. *et al.* A Theoretical Study on Initial Processes of Li-Ion Transport at the Electrolyte/Cathode Interface: A Quantum Chemical Molecular Dynamics Approach. *Jpn. J. Appl. Phys.* **49,** 04DP11 (2010).

153. Tasaki, K. Solvent decompositions and physical properties of decomposition compounds in Li-ion battery electrolytes studied by DFT calculations and molecular dynamics simulations. *J. Phys. Chem. B* **109,** 2920–33 (2005).

154. Xing, L. *et al.* Theoretical investigations on oxidative stability of solvents and oxidative decomposition mechanism of ethylene carbonate for lithium ion battery use. *J. Phys. Chem. B* **113,** 16596–602 (2009).

155. Leung, K. First-Principles Modeling of the Initial Stages of Organic Solvent Decomposition on LixMn2O4 (100) Surfaces. *J. Phys. Chem. C* **116,** 9852–9861 (2012).

156. Eriksson, T. *et al.* Surface Analysis of LiMn2O4 Electrodes in Carbonate-Based Electrolytes. *J. Electrochem. Soc.* **149,** A69 (2002).

157. Aurbach, D. *et al.* Review on electrode-electrolyte solution interactions, related to cathode materials for Li-ion batteries. *J. Power Sources* **165,** 491–499 (2007).

158. Matsui, M., Dokko, K. & Kanamura, K. Dynamic behavior of surface film on LiCoO2 thin film electrode. *J. Power Sources* **177,** 184–193 (2008).

159. Aurbach, D., Ein-Ely, Y. & Zaban, A. The Surface Chemistry of Lithium Electrodes in Alkyl Carbonate Solutions. *J. Electrochem. Soc.* **141,** L1 (1994).

160. Carroll, K. J. *et al.* Probing the electrode/electrolyte interface in the lithium excess layered oxide Li1.2Ni0.2Mn0.6O2. *Phys. Chem. Chem. Phys.* **15,** 11128–38 (2013).

161. Aurbach, D. *et al.* Recent studies of the lithium-liquid electrolyte interface Electrochemical, morphological and spectral studies of a few important systems. *J. Power Sources* **54,** 76–84 (1995).

162. Lux, S. F. *et al.* The mechanism of HF formation in LiPF6 based organic carbonate electrolytes. *Electrochem. commun.* **14,** 47–50 (2012).

163. Simmen, F. *et al.* Aspects of the Surface Layer Formation on Li1+xMn2O4−δ during Electrochemical Cycling. *J. Electrochem. Soc.* **157,** A1026 (2010).

164. Edstrom, K., Gustafsson, T. & Thomas, J. The cathode–electrolyte interface in the Li-ion battery. *Electrochim. Acta* **50,** 397–403 (2004).

165. Wang, E. *et al.* Stability of Lithium Ion Spinel Cells. III. Improved Life of Charged Cells. *J. Electrochem. Soc.* **147,** 4023 (2000).

166. Wang, R., Li, X., Wang, Z. & Guo, H. Manganese dissolution from LiMn2O4 cathodes at elevated temperature: methylene methanedisulfonate as electrolyte additive. *J. Solid State Electrochem.* (2015). doi:10.1007/s10008-015-2998-1

167. Nie, M., Abraham, D. P., Chen, Y., Bose, A. & Lucht, B. L. Lithium Ion Battery Graphite solid Electrolyte interphase (SEI characterized by microscopy and spectroscopy. (2013). doi:10.1021/jp404155y